Handling of 3D Clouds in Trace Gas Retrievals (3DCTRL)

ESA Contract No. AO/1-10877/21/I-AG

3DCTRL Validation Report v2.0

Evaluation of the improved handling of clouds in satellite NO_2 observations

MariLiza Koukouli[1], Dimitris Karagkiozidis[1], Arve Kylling[2], Huan Yu[3], Ronny Lutz[4], Víctor Molina García[4], Alkis Bais[1], and Michel Van Roozendael[3]

[1]Laboratory of Atmospheric Physics, Aristotle University of Thessaloniki (AUTH), Thessaloniki, Greece
[2]The Climate and Environmental Research Institute (NILU), Kjeller, Norway
[3]Royal Belgian Institute for Space Aeronomy (BIRA-IASB), Brussels, Belgium
[4]German Aerospace Center (DLR), Remote Sensing Technology Institute (IMF), Oberpfaffenhofen, Münchener Str. 20, 82234 Weßling, Germany

June 12, 2024

Document Approval Record

	Digital Signature
Prepared by MariLiza Koukouli	
Checked by Arve Kylling	

Document Change Record

Issue	**Date**	**Change**
0.9	May 19, 2023	First initial version
1.0	June 1, 2023	Final version
1.9	June 12, 2024	First initial version
2.0		Final version

Contents

List of Figures

List of Tables

Acronyms and abbreviations

ALB	Surface Albedo
AMF	Airmass factor
BRDF	Bidirectional reflectance distribution function
CAL	Clouds-As-Layers model
CBH	Cloud Bottom Height
CGT	Cloud Geometrical Thickness
CLASS	Comprehensive Large Array-Data Stewardship System
CTM	Chemistry Transport Model
COT	Cloud Optical Thickness
CRB	Clouds-as-Reflecting-Boundaries model
DOAS	Differential Optical Absorption Spectroscopy
dSCD	Differential Slant Column Density
EVDC	ESA Atmospheric Validation Data Centre
FRESCO	Fast Retrieval Scheme for Clouds from the Oxygen A band
FRM_4DOAS	Fiducial Reference Measurements for Ground-Based DOAS Air-Quality Observations
MAX-DOAS	Multi-Axis Differential Optical Absorption Spectroscopy
NDACC	Network for Detection of Atmospheric Composition Change
OCRA	Optical Cloud Recognition Algorithm
RAA	Relative Azimuth Angle
ROCINN	Retrieval of Cloud Information using Neural Networks
RTM	Radiative Transfer Model
SDR	Sensor Data Record
S-NPP	Suomi National Polar-orbiting Partnership
SZA	Solar Zenith Angle
TM5	Tracer Model 5
TROPOMI	TROPOspheric Monitoring Instrument
TVCD	Tropospheric vertical column density
VIIRS	Visible Infrared Imaging Radiometer Suite
VZA	Viewing Zenith Angle

1 Introduction

The European Space Agency, ESA, "Atmosphere Science Cluster – Research Opportunities 2" is established under the Scientific Exploitation component of the Future Earth Observation Programme. It is intended to support innovative scientific developments, which responds to Research and networking opportunities, but also targeted Research in the Atmospheric sciences. Under the Targeted Research Activities scope, ESA identified the need for Research on Handling of Clouds in Trace Gas Retrievals. The following scientific objectives for this Research opportunity were defined as follows:

- Evaluation of cloud products used for cloud correction in Copernicus Sentinel-4, Sentinel-5 and Sentinel-5P trace gas retrieval schemes by using reference datasets in which true cloud properties including their 3D structure and vertical distribution are known;
- Exploration of ways to improve the handling of realistic clouds in trace gas retrievals, using one short lived air pollutant as an example;
- Generation and evaluation of synthetic data of cloud properties where applicable;
- Testing and evaluation of the improved approach by handling of clouds in real observations.

The Handling of 3D Clouds in Trace Gas Retrievals, 3DCTRL, project[1] was defined to investigate the aforementioned scientific objectives.

In the following Validation Report version 2.0, VR v2.0, the effects of cloud properties and algorithm schemes on tropospheric nitrogen dioxide, NO_2, levels - chosen as a short lived air pollutant to be used as example- will be presented. A two-fold analysis has been performed within WP4; first, based on the synthetic spectra generated within this project and delivered to ESA as D4.1, and secondly, based on real Sentinel-5P TROPOspheric Monitoring Instrument, S5P/TROPOMI, real-life observations generated within this project and delivered to ESA as D4.3.

1.1 Approach and purpose of the document

Trace gas retrievals from nadir-sounding instruments are compromised by the presence of clouds ([Yu et al., 2022]). There are three different cloud effects that affect trace gas retrievals:

1. The albedo effect, related to the enhancement of reflectivity compared to clear scenes;
2. The cloud shadow effect when a part of the trace gas column is not exposed to direct sunlight due to clouds, causing a decrease in reflectivity compared to clear scenes;
3. The increase in absorption due to multiple scattering inside clouds and scattering of cloud sides.

With the 3DCTRL project Algorithm Theoretical Basis Document v2.0, delivered to ESA as project deliverable D2, possible retrieval algorithms improvements set to tackle the cloud issues were identified and extensively discussed. In the 3DCTRL ATBD v2.0, both theoretical as well as the actual suggested improvements are described, briefly discussed also in the beginning of this VR v2.0. The investigation here follows the four major tasks identified by the consortium as pertinent to WP4: Evaluation of the improved handling of clouds in satellite NO_2 observations.

- Task 4.1. Identify test cases for development and validation
  The main aim of this task is to define and identify interesting cases. This specifically means cases where high polluted NO_2 levels are observed simultaneously with clearly distinguishable cloud/clear boundaries. The behaviour of the approaches proposed by 3DCTRL at locations with more pristine, cloud-wise, conditions are also discussed. The ESA Atmospheric Validation Data Centre (EVDC)

[1] https://websites.auth.gr/3dctrl/

repository is utilized for identification of MAX-DOAS observational systems which provide a long enough timeseries of tropospheric NO_2 columns under various cloud conditions. The Visible Infrared Imaging Radiometer Suite (VIIRS) cloud coverage product is used to properly identify the location of the clouds with respect to both the ground and the space-borne observations. Sky camera images, that can provide a hemispherical view of the cloud structure locations, will also be employed, such as the one hosted by the Laboratory of Atmospheric Physics, Aristotle University of Thessaloniki, LAP/Auth, observing site.

- Task 4.2. Evaluate operational cloud products and cloud correction approaches
  In this VR v2.0, we compare operational cloud products and NO_2 retrievals with the new approaches provided by WP2 and WP3. 1D, 2D as well as full 3D cloud fields, available as part of the synthetic dataset provided by WP1, are employed in this investigation. The synthetic spectra were used to produce FRESCO, O_2-O_2 and OCRA/ROCINN cloud products. These are compared with/evaluated against the synthetic 3D cloud fields.

- Task 4.3. Assess the operational and optimized tropospheric NO_2 S5P/TROPOMI product
  Using the MAX-DOAS locations identified in task 4.1, where the ground-truth of the scattered cloud field is known, the operational and the optimized S5P/TROPOMI tropospheric NO_2 product provided by DLR as D4.2: Optimized S5P/TROPOMI NO2 output dataset, v2.0 and v3.0, respectively, are being assessed.

- Task 4.4. Identify further scientific and technical priority areas in this research area
  Based on lessons learned from the proposed project, further scientific and technical priority areas in this research area will be identified and quantified. This work will feed into Task 5.4, i.e. Scientific Roadmap document. This document shall describe all the experimental work carried out as well as the scientific results and findings of this project and shall further identify scientific and technical priority areas and provide guidance for future projects in the research activity.

1.2 Content of the document

The structure of the document is as follows: in section 2, two separate subsections describe the data pertaining to the synthetic spectrum investigations and the data pertaining to the S5P/TROPOMI observations investigations. In section 3 the two different validation methodologies that apply to the synthetic spectra and the real-time observations are briefly explained. In section 4, the same structure is followed, i.e. first a sub-section on the synthetic spectra covering both the cloud parameters investigations and the Air Mass Factor, AMF, and NO_2 investigations is provided following by the validation of the S5P/TROPOMI tropospheric NO_2 columns. VR v2.0 concludes with a discussion and summary section 5 as well as a short note on possible future research avenues in section 6.

2 Datasets used in this validation report

2.1 Data pertaining to the synthetic spectra investigation

2.1.1 Synthetic spectra

In order to investigate the effect of 3D cloud features on the NO_2 retrieval from space sensors, the 3D Monte Carlo model MYSTIC [Mayer, 2009, Emde et al., 2011], which is operated as one of several radiative transfer solvers in the libRadtran package [Mayer and Kylling, 2005, Emde et al., 2016], is used to generate synthetic observations. Three-dimensional means that it considers horizontal photon transport between adjacent grid cells. Scattering is calculated without approximations, i.e. multi-scattering is fully considered, also the realistic cloud optical properties including the scattering phase functions (Mie scattering for liquid clouds and aerosols and optical properties for the realistic ice crystal shapes for ice clouds). MYSTIC can be operated in plane-parallel/cartesian or is spherical geometry. For absorption, the REPTRAN parametrization is available. For high spectral resolution (line-by-line) it includes the very efficient ALIS method, this is essential to compute e.g. the O2A band with the Monte Carlo method. MYSTIC can also calculate 3D box-airmass factors. MYSTIC can also include a heterogeneous surface albedo and topography. The MYSTIC model allows the inclusion of 3D distributions of liquid clouds and ice clouds, mixed-phase clouds, multi-layer clouds and also inhomogeneous cloud voxels. Aerosols may also be added. The major difference to most other RT solvers is that MYSTIC is a 3D solver, which allows to study the impact of cloud shadows and in-scattering on trace-gas retrievals. RT solvers applied for trace gas remote sensing are mostly for 1D plane-parallel atmospheres, thus they can not be used to calculate the impact of clouds situated in neighbouring columns.

So far, MYSTIC does not include Raman scattering. It could be implemented in the future, indeed the Monte Carlo method in combination with ALIS should be well suited to efficiently calculate Raman scattering. Observed spectra are always impacted by Raman scattering. For this study, this is not relevant because we investigate the effect of cloud scattering and Raman scattering can be disabled in the retrieval algorithms when applied to synthetic spectra which do not include Raman scattering.

Another missing feature in MYSTIC is refraction which becomes important for large solar zenith angles or shallow viewing zenith angles, which are not typical for Sentinel-4, Sentinel-5, and Sentinel-5P observations. The dataset includes simulated spectra in two spectral ranges: the UV-visible band ranges 310-500 nm and the O_2-A band from 755-775 nm (see D4.1). In addition, it includes layer-AMFs calculated at 460 nm [Emde et al., 2022].

Two cloud setups are considered in this study. The first simulation involves a simple box cloud with varying geometrical and optical thickness, and radiance spectra are also simulated for a corresponding 1D cloud layer setup. The second simulation employs realistic 3D clouds from a large eddy simulation (LES) over Europe for various representative sun positions, satellite viewing angles, and surface albedos [for further details, see Emde et al., 2022].

2.1.2 Cloud products used in the synthetic satellite spectra trace gas retrievals

In order to correct the cloud effects on the gas retrievals, several cloud products have been developed that use different physical processes as approaches to retrieve cloud parameters such as cloud fraction, cloud height, and cloud optical thickness.

Aerosols are not included in this study. Nevertheless, their presence can have varying effects on trace gas retrievals. These effects depend on aerosol properties such as single scattering albedo, optical thickness, and vertical distribution. In practical terms, aerosols are implicitly treated as clouds in actual retrievals, as their effects are expected to be similar to those of clouds [Boersma et al., 2004, 2011]. However, relying on a cloud model to account for aerosols can introduce significant biases in trace gas retrievals. These biases could be mitigated by employing a more physically accurate aerosol model instead of a simple cloud model [Chimot et al., 2016, 2019]. It is worth emphasizing that aerosol correction has not been implemented in any operational trace gas products at present. Furthermore, developing a retrieval

algorithm using an advanced aerosol model is beyond the scope of this study.

2.1.2.1 OCRA/ROCINN

The Optical Cloud Recognition Algorithm (OCRA) and the Retrieval Of Cloud Information using Neural Networks (ROCINN) constitute the cloud retrieval algorithm tandem developed by the German Aerospace Center (DLR). OCRA employs a color-space approach to translate UV-Vis reflectances into colors from which the radiometric cloud fraction is computed [Lutz et al., 2016]. ROCINN is an optimal estimation algorithm in which NIR radiances in and around the O_2 A-band (between 758 and 771 nm), together with the OCRA radiometric cloud fraction as *a priori* information, are used to retrieve cloud-top height, cloud optical thickness and cloud albedo [Loyola et al., 2018].

The forward model used by ROCINN is an atmospheric radiative transfer model (e.g. LIDORT), which is generally replaced by a combination of two neural networks that emulate it (for both the clear-sky and cloudy contributions), reducing the computation time of the forward model calls several orders of magnitude. When ROCINN makes use of neural networks as emulators of the radiative transfer model, the neural network training is performed with a pseudo-random sample (consisting of more than 100 000 synthetic scenarios) that covers the space of input parameters appropriately (surface properties, geometric configuration, cloud properties), and for which the top-of-atmosphere radiances are computed by means of LIDORT (assuming a 1D atmosphere with pseudospherical correction). For the scope of this study, ROCINN is used with direct calls to LIDORT, so that the uncertainties due to the neural network training do not need to be considered in the subsequent analyses.

Two cloud models are implemented in ROCINN: the Cloud-As-Layer (CAL) model and the Cloud-as-Reflecting-Boundaries (CRB) model. CAL treats the clouds as a homogeneous layer of scattering liquid water particles to retrieve their cloud-top height and cloud optical thickness. The cloud-base height is not a retrieved quantity; instead, the cloud is assumed to have a constant geometrical thickness of 1 km. In the CRB model, clouds are considered as Lambertian equivalent reflectors, and the cloud height and cloud albedo are obtained as retrieved parameters. The ROCINN retrieval is not triggered if the cloud fraction does not reach a threshold of 0.05; under this situation, the cloud fraction is reset to 0 and the scene is considered as "clear-sky".

For this study, two cloud fraction models were initially employed in the ROCINN retrieval. The first uses either 0 or 1 as *a priori* cloud fraction (*cfmask*), while the second uses the cloud fraction obtained from OCRA (*cfocra*). The retrieval that uses the CRB cloud model with the "*cfmask*" cloud fraction is not utilised in this study due to its inadequacy in correcting retrievals of a tropospheric trace gas.

2.1.2.2 FRESCO

The FRESCO (the Fast Retrieval Scheme for Clouds from the Oxygen A-band) algorithm, developed by the Royal Netherlands Meteorological Institute (KNMI), models the effective cloud fraction and cloud height/pressure using the O_2-A band around 760 nm [Koelemeijer et al., 2001, Wang et al., 2008]. The cloud parameters are retrieved from top-of-atmosphere reflectances in three 1-nm wide wavelength windows at 758-759 nm, 760-761 nm, and 765-766 nm. FRESCO uses a Lambertian cloud model to describe the cloud reflection and transmission properties in a simplified manner. This model assumes that the cloud surfaces reflect light uniformly in all directions, resulting in the same intensity of reflected light regardless of the viewing angle. Additionally, the model assumes that no light is transmitted through the clouds. Cloud albedo is assumed to be a fixed value of 0.8. It is important to note that not all sensors are capable of detecting the O_2-A band, such as OMI and GEMS.

2.1.2.3 O_2-O_2

The O_2-O_2 algorithm has been developed by KNMI and was initially developed for OMI because this instrument does not cover the spectral range of the O_2-A band in the NIR [Acarreta et al., 2004, Pepijn

Veefkind et al., 2016]. The O_2-O_2 algorithm is based on the O_2-O_2 collision-induced absorption, which is a process where two oxygen molecules (O_2) collide and temporarily form a complex that can absorb light. This absorption occurs in specific spectral regions and is different from the absorption by individual oxygen molecules. The algorithm uses the satellite measurements from the O_2-O_2 absorption window at 477 nm, which is the strongest absorption band in the spectral range of OMI, to retrieve the effective cloud fraction and the cloud height/pressure using a similar cloud model to the one used in FRESCO. FRESCO algorithm originates from the use of absorption by a single molecule, scaled with oxygen number density (O_2), versus the use of absorption by a collision complex (O_2-O_2), scaled with oxygen number density squared. Therefore, the O_2-O_2 retrieval is more sensitive to clouds at lower altitudes and to aerosol. As in FRESCO, a fixed cloud albedo of 0.8 is assumed. Furthermore, the measured TOA reflectance can be smaller than the corresponding clear-sky reflectance due to factors such as cloud shadowing. To compensate for this negative bias, FRESCO and O_2-O_2 retrievals allow for negative cloud fractions. O_2-O_2 is a relatively weak absorber, which can limit the sensitivity and accuracy of cloud retrievals. Moreover, the accuracy of O_2-O_2 retrieval may be more susceptible to atmospheric conditions, such as aerosols, compared to O_2-A clouds.

Concluding, we should note that a limitation of the FRESCO, O_2-O_2 and ROCINN CRB algorithms is their assumption of a Lambertian cloud, i.e. an idealized reflecting boundary that does not account for vertical extend and in-cloud multiple scattering. As a step towards a physically more realistic description of a cloud, the ROCINN CAL algorithm, in contrast to the three algorithms mentioned before, assumes a vertically extended cloud model consisting of a single layer of liquid water droplets that allows for multiple scattering within the cloud.

2.1.3 NO_2 retrievals based on the synthetic spectra

The classic NO_2 retrieval algorithm is based on the DOAS technique, which consists of two steps [Boersma et al., 2004]: first, the slant column density (SCD) is obtained by using spectral fitting methods within a predefined window of a set of relevant reference spectra to a satellite-measured reflectance spectrum. Second, the AMF is applied to convert the SCD into a vertical column density (VCD).

For the optically thin absorber (such as NO_2, HCHO), the AMF (M) can be written as a linear sum of the altitude-dependent AMF of each layer, weighted by the NO_2 partial vertical column [Palmer et al., 2001]:

$$M = \frac{\sum_i m_i \cdot x_i}{\sum_i x_i} \tag{1}$$

Where m_i is the box-AMF and x_i is the NO_2 partial column density of layer i.

For partly cloudy scenes, the independent pixel approximation (IPA) approach is used. This method assumes that the AMF can be expressed as a linear combination of a clear AMF (M_{clr}) and a cloudy AMF (M_{cld}):

$$M = (1 - CF_w) \cdot M_{clr} + CF_w \cdot M_{cld} \tag{2}$$

The term CF_w, see equation 6, refers to the fraction of radiance that originates from the cloudy part of a pixel, commonly known as the cloud radiance fraction or intensity-weighted cloud fraction. When assuming a Lambertian cloud, the AMFs for cloudy scenes are calculated using Eq. 1, with a specific cloud albedo and cloud pressure, and setting $m_i = 0$ below the cloud. On the other hand, if the CAL cloud model is used in the AMF calculation, the clouds are treated as optically uniform layers of light-scattering particles (water droplets), and their optical properties are consistent with those used in cloud retrieval.

The analysis from previous 3DCATS study indicates that the cloud effect on AMF is less significant in remote regions compared to polluted areas, and cloud-corrected AMF exhibits better agreement with the truth values for less polluted regions. Furthermore, in polluted regions, the uncertainty in tropospheric NO_2 retrieval is primarily dominated by uncertainties in AMF calculations. Conversely, in less polluted

regions, the uncertainty in slant column retrieval become more prominent. Thus, our study concentrates specifically on highly polluted NO_2 cases..

Furthermore, several NO_2 profiles (Fig. 1) from the TM5 CTM are included to investigate the impact of profile shape on the calculation of the NO_2 AMF. The previous study [Yu et al., 2022] has shown that the impact of clouds on NO_2 retrieval is more sensitive in polluted cases than in clean air cases. Therefore, we use the NO_2 profile from Northern China region as the baseline, as it is one of the most polluted regions in the world. In addition, the tropopause height is set to a fixed value of 15 km in this study.

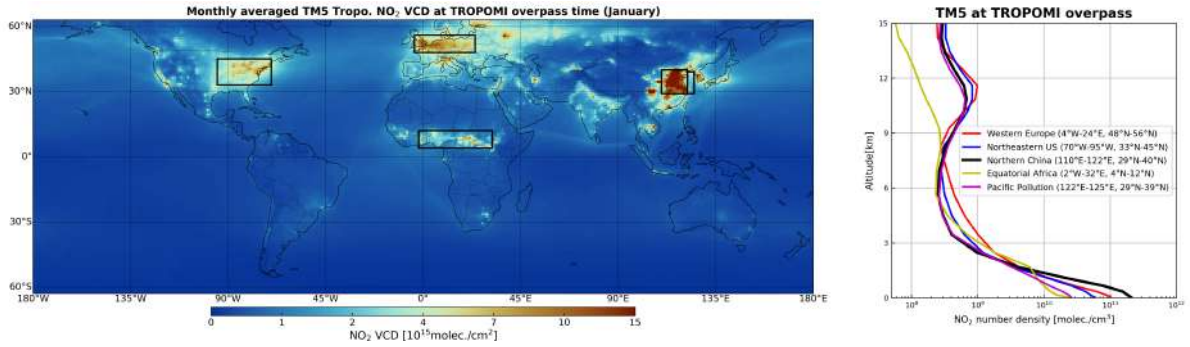

Figure 1: Tropospheric NO_2 derived from the TM5-MP daily analysis, with a spatial resolution of $1° \times 1°$ and a temporal resolution of 1 hour. This dataset serves as the auxiliary support product used for the operational S5P/TROPOMI NO_2, SO_2, and HCHO retrievals. Left panel: map of tropospheric NO_2 content for January (2018-2022) simulated by TM5 CTM at TROPOMI overpass time; right panel: averaged tropospheric NO_2 profiles over five selected regions. The black line represents the baseline, which is the average NO_2 profile over the Northern China region, known as one of the most polluted regions in the world.

2.2 Data pertaining to the S5P/TROPOMI retrievals investigation

2.2.1 S5P/TROPOMI tropospheric NO_2 columns

TROPOMI is the satellite instrument on board the Copernicus Sentinel-5 Precursor (S5P) satellite Veefkind et al. [2012]. Several trace gases are derived from TROPOMI measurements, such as total ozone, sulphur dioxide, formaldehyde, carbon monoxide, methane, etc. In this work we focus on NO_2 as it is an important measure of air quality and a key tropospheric trace gas measured by the Atmospheric Sentinels[2].

As part of the 3DCTRL project, DLR has provided the validation teams D4.2: Optimized S5P/TROPOMI NO_2 output datasets, v2.0 and v3.0.

The original DLR algorithm and its improvements have been extensively described in [Liu et al., 2021]. In the validation exercise included in this paper performed against ground-based MAX-DOAS measurements, the DLR tropospheric NO_2 data showed good correlations for nine European urban/suburban stations, with an average correlation coefficient of 0.78. They further report that implementation of the algorithm improvements lead to a decrease of the relative difference from -55.3% to -34.7% on average in comparison with the DLR reference retrieval. For D4.2 v2.0, the algorithm settings are provided in the v2.0 dataset ReadMe file, which in cases are different from the settings used in [Liu et al., 2021]. Similarly, for D4.2 v3.0, an updated dataset ReadMe file enumerates further improvements. Here, we briefly mention the algorithm steps relating to the cloud treatments which give rise to three tropospheric NO_2 columns; the first is based on the ROCINN/CRB cloud treatment, the second is based on the ROCINN/CAL cloud treatment and the third is based on the ROCINN/CAL cloud treatment with a surrogate cloud model,

[2] https://sentinel.esa.int

discussed further below. Details on the first two cloud treatments can be found in e.g. Loyola et al. [2018, 2021] while for the ROCINN/CAL cloud treatment with a surrogate cloud model in the ATBD v2.0.

The general approach is that an apriori radiometric cloud fraction is determined by the OCRA algorithm as a first step. This is then an input to the second step, the ROCINN algorithm, which comes in the two flavors, namely CAL and CRB. ROCINN/CAL retrieves cloud fraction, cloud top height and cloud optical thickness, while ROCINN/CRB retrieves cloud fraction, effective cloud height and effective cloud albedo.

In general, CAL and CRB are based on two conceptually different cloud models: In CAL, a cloud consists of a scattering layer of liquid water droplets, following the Mie theory, while in CRB a cloud is considered as a Lambertian surface. When comparing the CAL and CRB cloud parameters on a global scale, the following general issues should be kept in mind:

- The cloud fractions from ROCINN CAL and CRB are very similar, because their retrieval is strongly regularized towards their apriori input value from OCRA. The ROCINN/CAL cloud top heights are (on a global average) roughly 800m above the ROCINN/CRB effective cloud heights which are more representative of the "middle" of the cloud
- ROCINN/CAL only retrieves the cloud top height. The cloud base height is assumed with a fix offset of -1000m in the retrieval, i.e. the assumed cloud geometric thickness in CAL is 1km. The top and base pressures are then only a converted quantity from the retrieved top height and offset base height. The largest differences seem to appear for large pressures, i.e. close to the surface. Cloud retrievals very close to the surface are challenging and differences between CAL and CRB become more obvious here when keeping in mind that the global average offset is about 800m between the cloud top and cloud "middle". The assumption that a Lambertian cloud (CRB) has no vertical extent while a CAL cloud has a vertical extent of 1km then also impacts the comparisons between CAL and CRB when the top height is less than 1km above the surface.
  This issue is discussed in section 4.2.
- The cloud albedo is provided by the CRB model which is representative of "effective" or "mid-height" parameters. In the cloud albedo product, over-estimations have been observed over sunglint areas, which should not really affect the comparisons shown later on, apart from the coastal sites. We should note here that the surface treatment is similar in CAL and CRB (both use the GE–LER database).
- The ROCINN/CAL cloud optical thickness/depth, COD, retrieval works best for optically thick clouds. Very optically thin clouds, with COD between 0 and 5, are challenging to retrieve from the spectral range where ROCINN is operating (O_2-A band in the NIR). The cloud parameter retrieval in that very low COD regime is therefore quite error prone. COD is also linked closely to the cloud fraction and the ROCINN retrieval tends to compensate underestimated cloud fractions with enhanced COD and vice versa.

Finally, we should mention at this stage that from the theoretical assessments performed within the ATBD (D2 of this project) the way that OCRA works leads us inherently to the *surrogate cloud model* because it utilizes measured radiances, which are 3D quantities. This effect is even stronger if applied in tandem with ROCINN/CAL, while ROCINN/CRB is a very rough approximation from the physical point of view and the theoretical interpretation is not as straighforward. In the ROCINN/CAL provided tropospheric NO_2 with the current OCRA version the surrogate cloud model has hence been applied and forms the third tropospheric NO_2 column examined.

2.2.2 Visible Infrared Imaging Radiometer Suite (VIIRS)

S5P flies in tandem with the Suomi National Polar-orbiting Partnership (S-NPP) satellite. The S-NPP payload includes the Visible Infrared Imaging Radiometer Suite (VIIRS) instrument, which may be used as an imager for TROPOMI.

We used both VIIRS L1b and L2 data. The L1b reflectances were used for RGB plots and to produce various metrics, see section 2.2.3. The L2 data include various cloud products of which we used the cloud mask, cloud shadow, cloud optical thickness and cloud top height products. The TROPOMI data includes the latitude and longitude of the corners of each TROPOMI pixel. This information was used to identify VIIRS pixels within each TROPOMI pixel. Examples of various VIIRS data products are shown in Fig. 38. It is noted that the difference in overpass time for S5P and S-NPP is slightly more than four minutes and care must be taken to for example movement of clouds when combining data from the two platforms [e.g. Trees et al., 2022].

VIIRS data were accessed through the NOAA Comprehensive Large Array-Data Stewardship System (CLASS, `https://www.class.noaa.gov`). L2 data were obtained from the JPSS VIIRS Products (Granule) (JPSS_GRAN) while L1 data were taken from JPSS VIIRS Sensor Data Record (VIRRS_SDR).

2.2.3 Cloud metrics from VIIRS and S5P/TROPOMI

In addition to the data products from VIIRS and TROPOMI various metrics were calculated from the VIIRS and TROPOMI data. They are described by Kylling et al. [2022] and repeated below for completeness.

2.2.3.1 Cloud geometric and radiance fractions Cloud fractions may be defined in several ways. We calculate the geometric cloud fraction, CF_g, the radiometric cloud fraction, CF_r, and the weighted radiometric cloud fraction, CF_w.

The geometric cloud fraction for a TROPOMI pixel is defined as

$$CF_g = \sum CM_i/N, \tag{3}$$

where the sum is over all N VIIRS pixels within the TROPOMI pixel and CM_i is the VIIRS cloud mask where $CM_i = 1$ for pixels identified as cloudy and $CM_i = 0$ otherwise.

The radiometric cloud fraction is the fraction of measured radiance reflected from clouds in a pixel [see also Grzegorski et al., 2006]

$$CF_r = \begin{cases} 0 & R \le R_s \\ \frac{R-R_s}{R_c-R_s} & R_s < R < R_c \\ 1 & R \ge R_c \end{cases} \tag{4}$$

Here R is the observed reflectance, R_s is the reflectance for a cloudless sky and R_c the reflectance for an opaque cloud. For the O_2-O_2 cloud correction, CF_r is calculated based on the reflectance at 460nm which is in the middle of the DOAS fitting window for NO_2. For the FRESCO algorithm, CF_r is determined by the reflectance in the 758-759nm window band. Further details are described by Yu et al. [2022]. We also define an average radiometric cloud fraction CF_r^{VIIRS} using the average of CF_r calculated for each VIIRS M3 band pixel, centred at 0.488 μm, within a TROPOMI pixel:

$$CF_r^{VIIRS} = \sum CF_{r,i}/N, \tag{5}$$

where the sum is over all N VIIRS pixels within the TROPOMI pixel.

Finally, the weighted radiometric cloud fraction is defined as [Yu et al., 2022]

$$CF_w = \frac{CF_r R_c}{CF_r R_c + (1 - CF_r) R_s} \tag{6}$$

2.2.3.2 Cloud shadow fraction The VIIRS cloud shadow mask algorithm is geometry-based and described by Hutchison et al. [2009]. They compared the MODIS MOD35 product which uses spectral signatures to identify cloud shadows with geometry-based approaches and states that the latter "are far

superior to those predicted with the spectral procedures". A cloud shadow detection algorithm using TROPOMI data only have been described by Trees et al. [2022]. It was, however, not available for this study.

The cloud shadow fraction, CSF, for a TROPOMI pixel is defined as

$$CSF = \sum CSM_i/N, \tag{7}$$

where the sum is over all N VIIRS pixels within the TROPOMI pixel and CSM_i is the VIIRS cloud shadow mask where $CSM_i = 1$ for pixels identified as cloud shadow and $CSM_i = 0$ otherwise.

2.2.4 MAX-DOAS ground-based instruments

Multi-Axis Differential Optical Absorption Spectroscopy (MAX-DOAS) is a well-established and commonly used remote sensing technique for the detection of trace gases and aerosols in the troposphere. MAX-DOAS utilizes scattered sunlight in the ultraviolet (UV) and visible (VIS) parts of the electromagnetic spectrum received from different elevation angles, usually from the horizon up to the zenith [Hönninger et al., 2004], and the recorded solar spectra are analyzed by differential optical absorption spectroscopy (DOAS) [Platt and Stutz, 2008] for the determination of trace gas differential slant column densities (dSCDs). MAX-DOAS measurements are highly sensitive to various absorbers that exhibit distinct absorption features (such as NO_2, HCHO, SO_2, H_2O, O_3, BrO and CHOCHO) in the lowest few kilometers of the atmosphere. While 1D MAX-DOAS instruments can measure trace gas concentrations at a fixed azimuth, which may usually not be representative for the NO_2 load in the surrounding areas, 2D systems perform elevation scans at multiple azimuth viewing directions, providing an improved spatial coverage (potentially of 360° assuming clear line of sight), allowing for the investigation of possible horizontal inhomogeneities and for a better characterization of the field around the measurement site [e.g. Chan et al., 2020, Schreier et al., 2020, Karagkiozidis et al., 2023].

Information about the vertical distribution of a trace gas can be obtained from a single elevation scan by applying proper inverse modelling approaches that combine the measurements with Radiative Transfer Model (RTM) simulations [e.g. Clémer et al., 2010, Irie et al., 2011, Bösch et al., 2018, Friedrich et al., 2019]. The capability of retrieving trace gas vertical profiles, vertical column densities and surface concentrations with a generally good accuracy and temporal resolution makes MAX-DOAS systems essential for air quality monitoring, providing also reference ground-based data for the validation of satellite trace gas measurements [e.g. Dimitropoulou et al., 2020, Pinardi et al., 2020, Verhoelst et al., 2021].

2.2.5 Thessaloniki All Sky camera

LAP/Auth is a multi-instrument atmospheric composition observational site, established in 1982, hosting a large variety of ground-based instrumentation with multi-decadal timeseries[3]. With respect to the needs of this project, we mention the commercial visible all-sky-imaging system (MOBOTIX Q24), operating on the rooftop of the Laboratory of Atmospheric Physics (40.634° N, 22.956° E), about 60 m above sea level. The camera points to the zenith and a fish-eye lens is mounted in front of the entrance optics of the camera, allowing for a field of view of 180°, hence providing a hemispherical view of the sky. The camera is configured to capture images of the sky every 1 min, which are stored in JPEG format with a resolution of 1280×960 pixels. The camera operates routinely under all weather conditions and the captured images can be used as a visual tool for the detection of cloud patterns and the horizontal distribution of clouds around the measurement site. No automated algorithm has, as of yet, been developed for the automatic calculation of the cloud fraction. Thus, differentiating the cloud coverage conditions is not based on well-defined thresholds of the cloud fraction, rather than on empirical observation of the images. Figure 2 shows three sample images captured by the sky-camera in Thessaloniki under different weather and cloud conditions.

[3] https://lapweb.physics.auth.gr/en/infrastructure/

Figure 2: Sample images captured by the sky-camera in Thessaloniki under clear (left), broken clouds (middle) and overcast (right) conditions.

3 Validation Methodology

A brief summary of the two validation approaches used in Section 4 is provided in the following two subsection. The first applies to the validation of the synthetic low Earth orbit spectra while the second to the validation of the S5P/TROPOMI Observations.

3.1 Validation of the synthetic data

In order to investigate the errors in trace gas retrievals using the synthetic data, MYSTIC includes the option to simulate 1D layer-AMFs or 3D box-AMFs [Schwaerzel et al., 2020]. Layer-AMFs, which are often called "box-AMFs" although they refer to atmospheric layers, are commonly obtained as an intermediate result in DOAS-type retrievals. They are derived from the distribution of photon path lengths within the individual layers of the model atmosphere. When considering the horizontal variability of trace gas concentrations, the conversion from SCD to VCD should be performed using 3D box-AMFs instead of 1D layer-AMFs. However, in this study, the focus is on examining the influence of 3D cloud structures on trace gas retrievals, and thus the trace gas concentration is assumed to be horizontally homogeneous. The error of the NO_2 retrieval is assessed by comparing the calculated AMF, as described in Section 2.1.3, with the true AMF. The true AMF is computed using 1D layer-AMFs from MYSTIC combined with the NO_2 profile.

3.2 Validation of the S5P/TROPOMI NO_2 observations

3.2.1 EVDC MAX-DOAS observations

The MAX-DOAS data that are used for validating the TROPOMI tropospheric NO_2 products are collected through the ESA Atmospheric Validation Data Centre [4], EVDC. The analysis is focused on selected days in 2021 and 2022 based on observations from eight European measurement sites, two of which are located in Greece (Thessaloniki and Athens), while the rest of them are distributed in northern Europe, see Table 1. The MAX-DOAS data sets for the selected sites that are included in EVDC are either generated individually by the instruments' principal investigators or they are commonly processed by the Fiducial Reference Measurements for Ground-Based DOAS Air-Quality Observations[5], FRM_4DOAS, based on harmonized tropospheric NO_2 retrieval settings. In order to avoid uncertainties caused by different NO_2 data processing settings, only the MAX-DOAS data that are produced by FRM_4DOAS are used for the validation.

For some of the selected stations, the MAX-DOAS instruments are fixed at a single azimuth viewing

[4] https://evdc.esa.int/
[5] https://frm4doas.aeronomie.be/

direction, while few instruments measure solar scattered spectra at multiple azimuths, providing data that are usually more representative for the surrounding area, allowing for a better characterization of the NO_2 horizontal distribution. The locations of the selected MAX-DOAS systems that are used for the validation are summarized in Table 1. Figure 3 shows a visualization of the instruments' geographical distribution along with the azimuth viewing directions being scanned for all measurements sites. Specifically for Mainz, four instruments operate simultaneously at different azimuths for the selected time period and their viewing directions are combined in the corresponding sub-panel.

Table 1: Location and azimuth viewing directions of the selected MAX-DOAS instruments.

Location name	Longitude	Latitude	Instrument name	# of viewing azimuth angles	Azimuth viewing angles
Athens	23.86000	38.05000	iup008	7	120.0 150.0 220.0 232.5 245.0 257.5 275.0
Bremen	8.84941	53.10366	iup002	3	180.0 270.0 295.0
Cabauw	4.92700	51.96800	knmi006	1	287.0
De Bilt	5.17800	52.10100	knmi004	1	80.0
Heidelberg	8.67460	49.41730	uheidelberg001	1	324.0
Mainz	8.23000	49.99000	mpic001	1	321.0
Mainz	8.23000	49.99000	mpic002	1	51.0
Mainz	8.23000	49.99000	mpic003	1	141.0
Mainz	8.23000	49.99000	mpic004	1	231.0
Thessaloniki	22.95600	40.63400	lap008	4	142.0 185.0 220.0 255.0
Uccle	4.36000	50.80000	iasb011	4	11.0 35.5 105.0 262.5

3.2.2 Selection of collocated observations

Producing TROPOMI NO_2 overpass data for all sites since the beginning of the S5P mission would require a large computational effort. Furthermore, the MAX-DOAS tropospheric NO_2 data sets for the selected stations of EVDC cover different time periods with some of them having gaps in their time series. Thus, the analysis and the validation in this VR v2.0are focused on selected days in 2021 and 2022, which are characterized by different NO_2 levels and cloud conditions. The DLR algorithm team prodived these S5P/TROPOMI tropospheric NO_2 observations, forming part of D4.2 v1.0.

In order to identify and further investigate interesting cases for the validation of TROPOMI tropospheric NO_2 columns, two report files have been generated (one for 2021 and one for 2022, respectively), containing visualisations and statistics from the MAX-DOAS instruments, images from VIIRS and cloud fraction data from the operational S5P/TROPOMI NO_2 product, for all stations and for all days. In Sect. 3.2.3 and 3.2.4, the results from two example study cases in summer and winter (on 13.08.2021and 12.02.2021, respectively) are presented, which are summarized in Table 2 and Figures 4-8 for the summer case and in Table 3 and Figures 9-12 for the winter case. Equivalent tables and figures are produced for all days of 2021 and 2022, which have been uploaded as two pdf documents to the project Internal Document pages, as part of deliverable D3 VR v2.0.

Each day is investigated separately and it is automatically flagged as potentially interesting based on the following criteria:

1. Tropospheric NO_2 column data from at least 4 ground-based MAX-DOAS instruments must be reported. Furthermore, it is required that each operating instrument reports a minimum of 4 measurements between 10:00 and 14:00 UTC. This corresponds to roughly 1 measurement per hour so that a collocation with TROPOMI can eventually be achieved.

2. Images from VIIRS, showing the cloudiness situation, must be available for all operating sites.

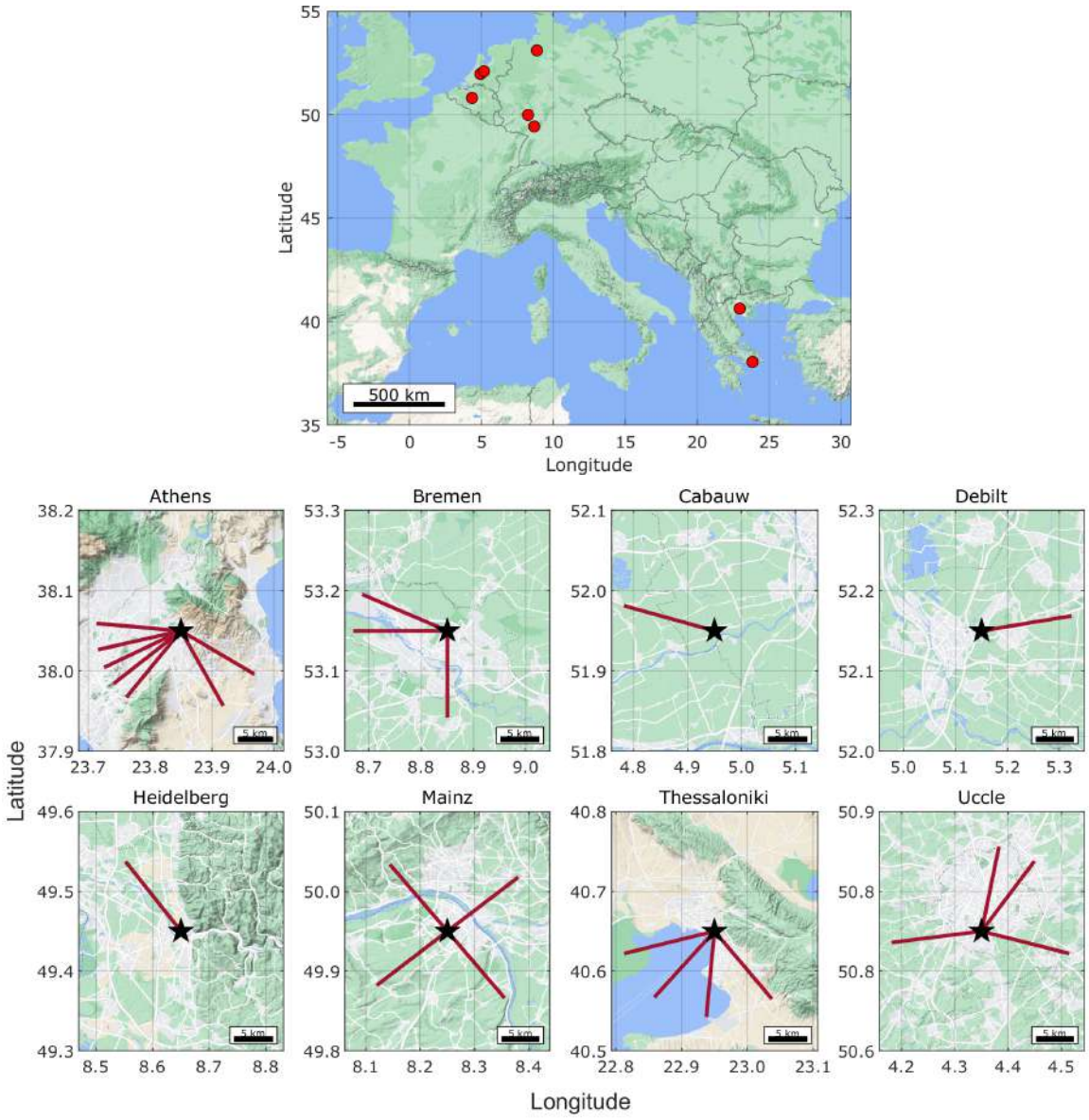

Figure 3: The geographical distribution of the selected European measurement sites (top figure) and the azimuth viewing directions for the respective MAX-DOAS instruments (bottom panels).

3. The mean cloud fraction (from all pixels within 20 km radius) reported by the operational S5P/TROPOMI NO_2 product must be ≤ 0.5 for all operating sites.

For Mainz, where several instruments operate simultaneously, data from one system only have been used, since otherwise, the flagging algorithm could potentially lead to misleading results. The aim here is to identify cases where NO_2 data are available from as many as possible different locations around Europe.

3.2.3 Case study in summer (13.08.2021)

The number of available ground-based MAX-DOAS observations along with the mean cloud fraction that is reported by the operational S5P/TROPOMI NO_2 per station on this example day in summer are summarized in Table 2.

Table 2: Number of MAX-DOAS measurements and the average TROPOMI cloud fraction per station on 13.08.2021.

Station	Number of observations	Oper. TROPOMI cloud fraction
Athens	27	0.01
Bremen	4	0.37
Cabauw	12	0.40
De Bilt	13	0.37
Heidelberg	11	0.09
Mainz	0	0.37
Thessaloniki	7	0.07
Uccle	0	0.26
Sum	**74**	**N/A**

Figure. 4 shows the images from VIIRS for all stations ($\pm 1^\circ$ in latitude and longitude) on 13.08.2021, where different cloud coverage conditions and cloud structures can be visually identified. The images have been automatically downloaded using the NASA Worldview interface[6]. In some cases, usually due to instrument malfunction, VIIRS data are not available and hence the reported images are either partly or totally black. In order to automatically extract valid images, an RGB-based image processing technique is implemented, i.e., the RGB composition of each pixel is identified and the number of totally black pixels (R=0, G=0, B=0) is calculated, normalized by division with the total number of pixels. If the fraction of black pixels is $> 50\%$, then the image is considered invalid. In this example (Figure. 4), VIIRS images are available for all stations.

An image captured on 13.08.2021 by the sky camera in Thessaloniki is presented in Figure. 5. The images from the sky camera are downloaded from a dedicated LAP/Auth server, and only the image that is captured closer to VIIRS overpass time is selected (only if images within ± 15 minutes exist). Such images can be used for a more detailed visual investigation of the cloud conditions in Thessaloniki and thus for a better assessment of the TROPOMI tropospheric NO_2 product.

Figure. 6 shows the tropospheric NO_2 VCDs for all ground-based instruments. The NO_2 columns are shown as polar plots, where the azimuth angle is the azimuth viewing direction of the instruments and the radius represents the measurement time in UTC. The red lines approximately indicate the temporal window of TROPOMI overpass and the green lines represent the time range in which at least 4 measurements are required for each MAX-DOAS instrument. In this case, 6 ground-based instruments meet the requirement.

Histograms of the tropospheric NO_2 columns for all instruments are presented in Figure. 7. Such results are produced for all days, in order to identify cases of various concentrations and to validate the TROPOMI NO_2 TVCDs under different NO_2 levels.

[6] `https://worldview.earthdata.nasa.gov/`

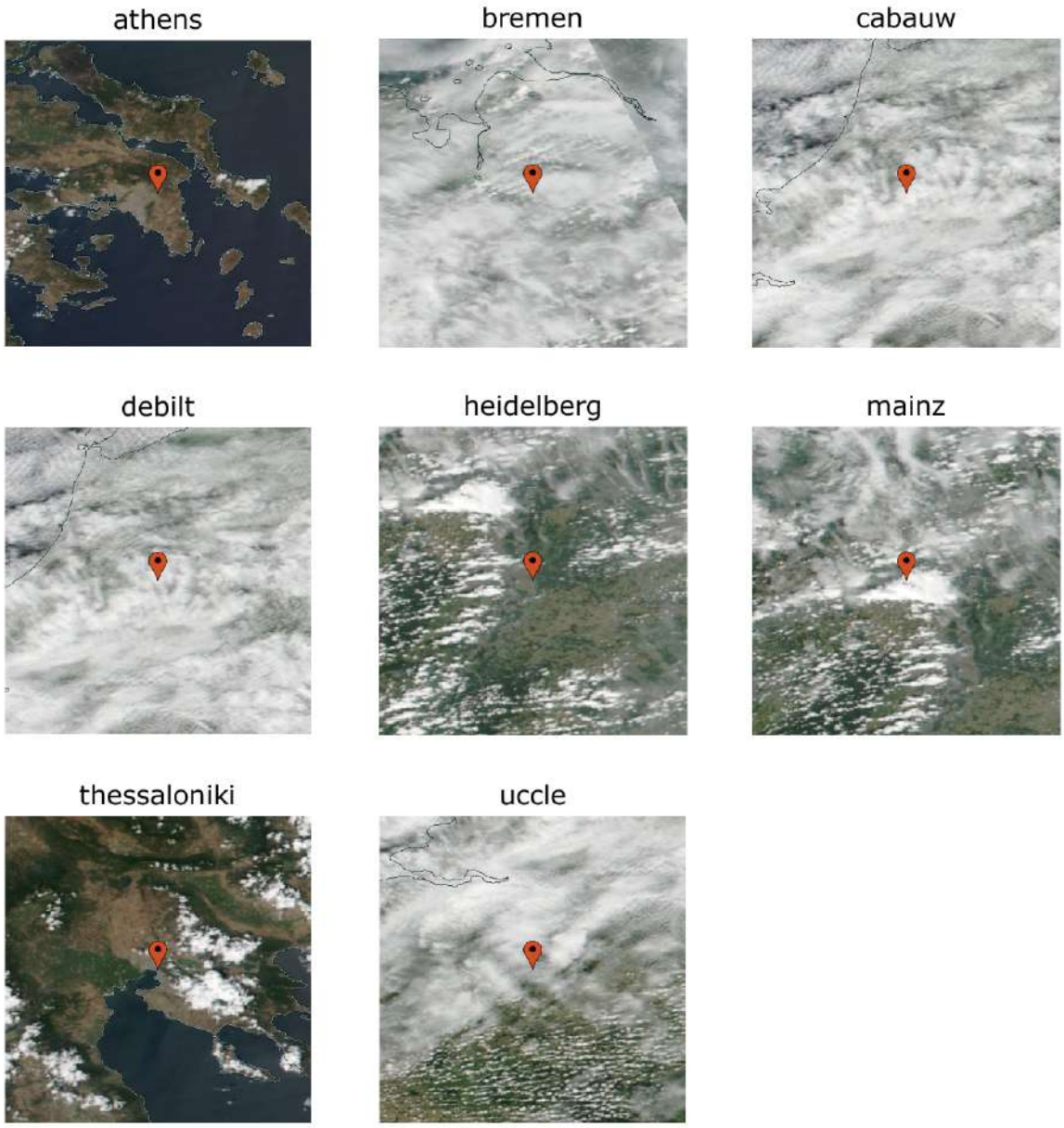

Figure 4: Images from VIIRS per station on 13.08.2021.

Figure 5: Image from the sky camera in Thessaloniki captured close to VIIRS overpass time on 13.08.2021.

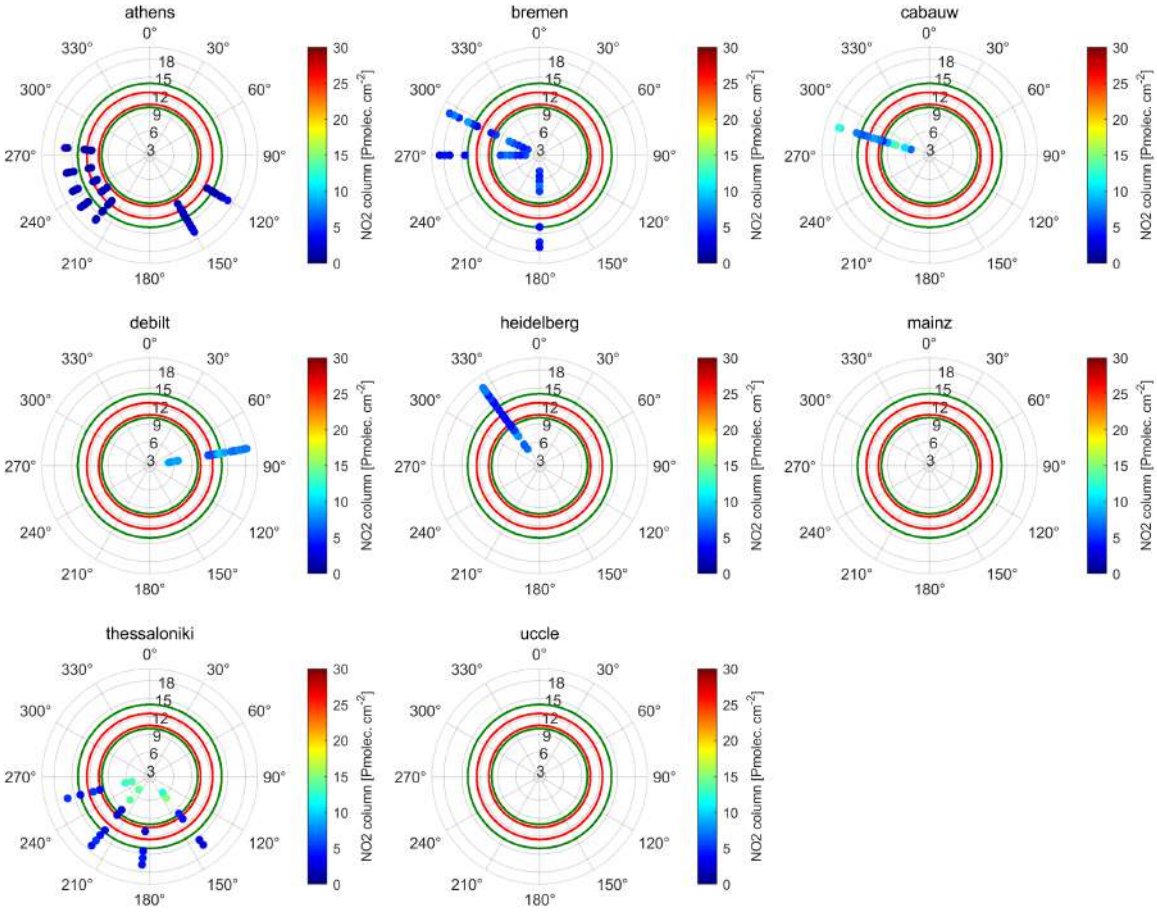

Figure 6: Polar plots of tropospheric NO_2 columns from all MAX-DOAS instruments on 13.08.2021. The azimuth angle is the azimuth viewing direction and the radius represents the measurement time in UTC.

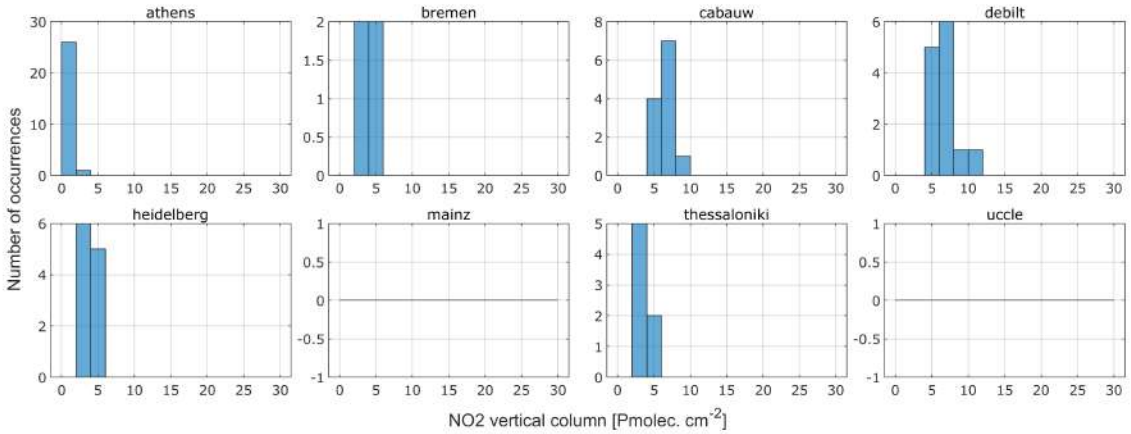

Figure 7: Frequency distribution of the MAX-DOAS tropospheric NO_2 VCDs per station (between 10:00 and 14:00 UTC) on 13.08.2021.

Figure. 8 shows the MAX-DOAS NO_2 vertical profiles (colored by the solar zenith angle) that are reported from all stations. The number in the upper right corner of each sub-panel indicates the number of available measurements. The aim here is to identify cases that are characterized by various NO_2 vertical distributions, e.g., investigate highly polluted conditions, where a substantial part of the NO_2 load lies at low altitudes, below the cloud. Also, the effect of known geophysical parameters, such as the SZA, on the NO_2 product and on the 3D cloud treatment is to be further investigated.

3.2.4 Case study in winter (12.02.2021)

The results presented for this case study are equivalent to those in Sect. 3.2.3. On this day, 5 ground-based MAX-DOAS systems were operational, images from VIIRS are available for all stations, but no image from the sky camera in Thessaloniki was captured, due to instrument malfunction.

Table 3: Same as Table 2, but on 12.02.2021.

Station	Number of observations	Oper. TROPOMI cloud fraction
Athens	15	0.02
Bremen	2	0.28
Cabauw	0	0.60
De Bilt	8	0.50
Heidelberg	15	0.27
Mainz	14	0.22
Thessaloniki	9	0.00
Uccle	0	0.36
Sum	**63**	**N/A**

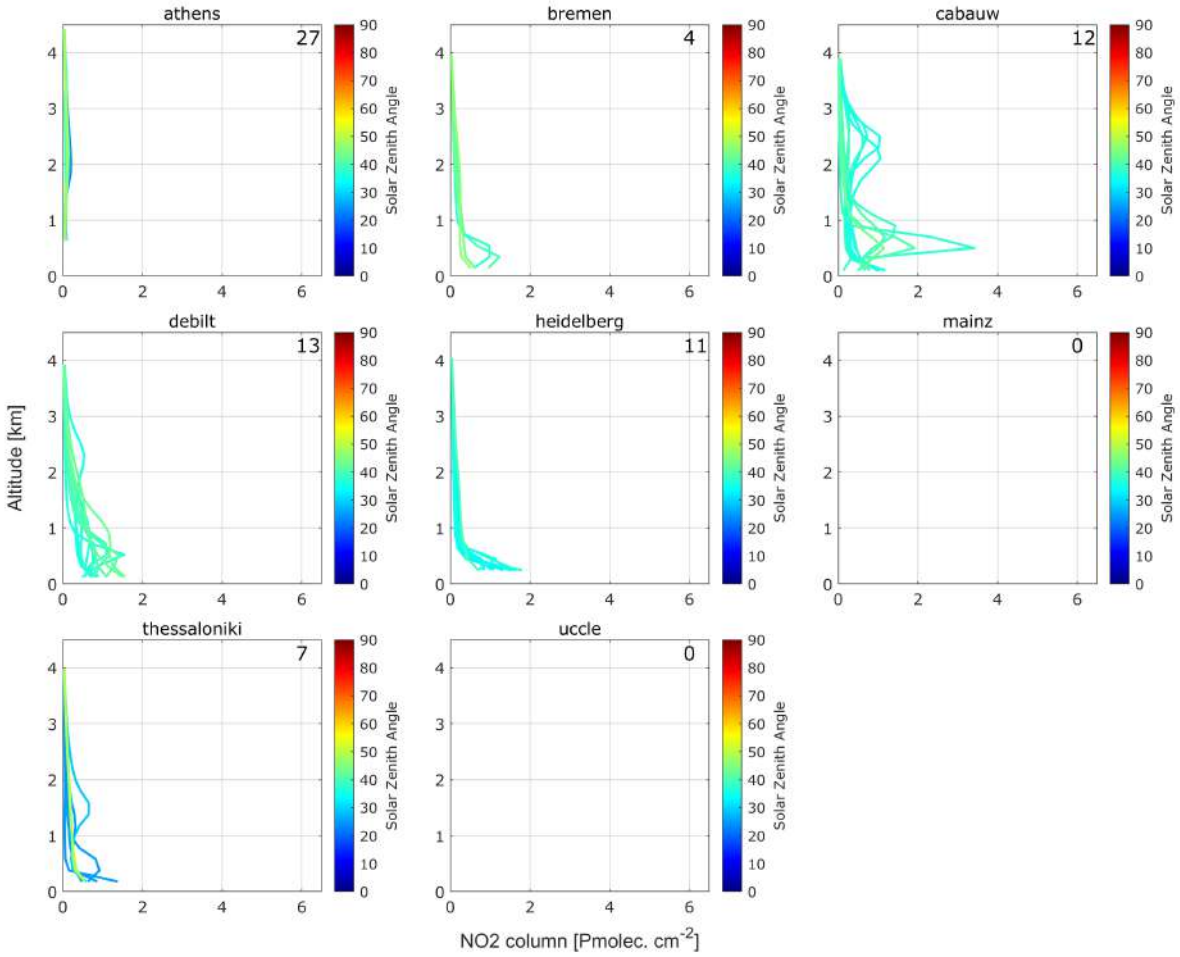

Figure 8: NO_2 vertical profiles for all MAX-DOAS instruments (between 10:00 and 14:00 UTC) on 13.08.2021.

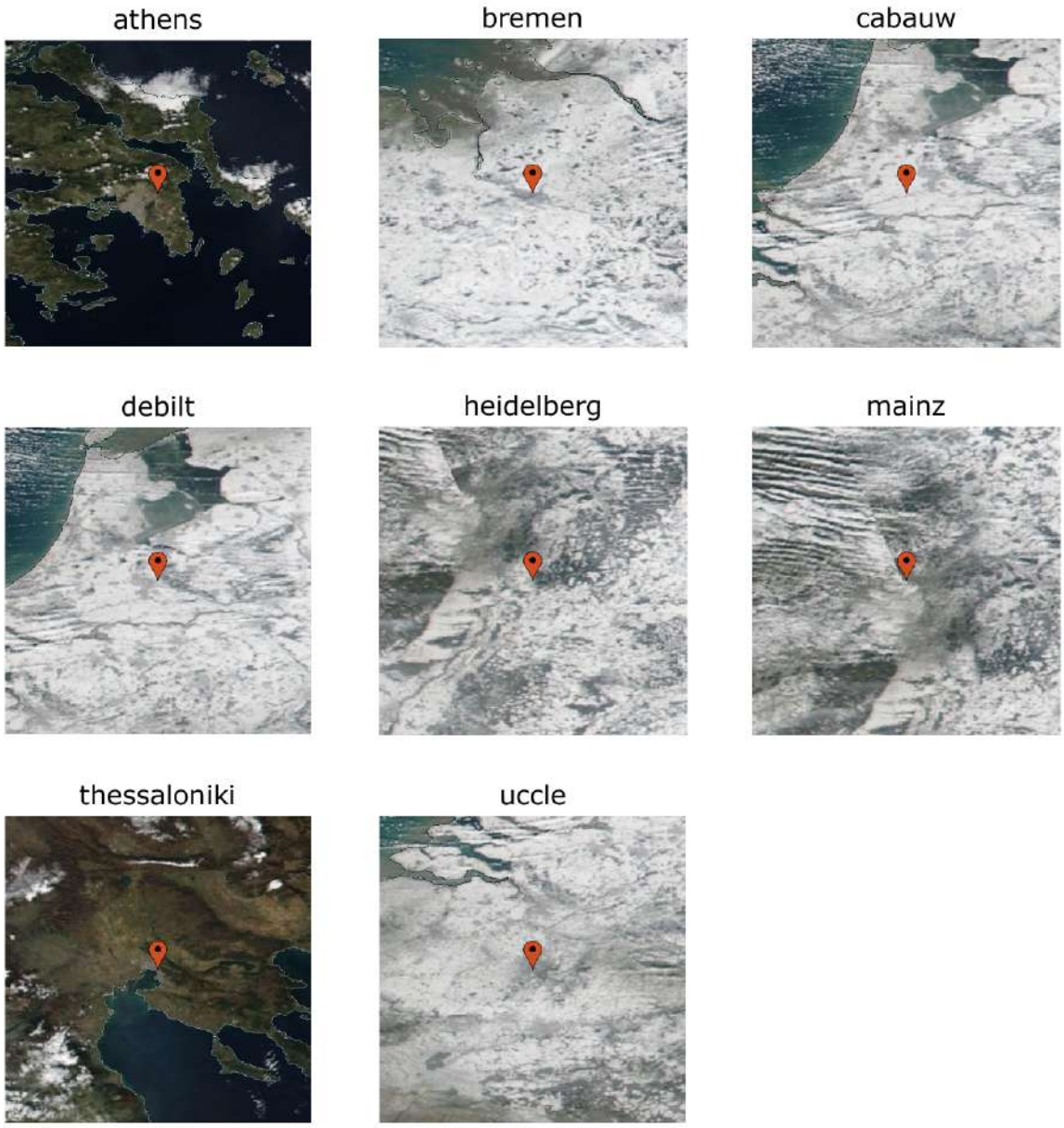

Figure 9: Same as Figure. 4, but for 12.02.2021.

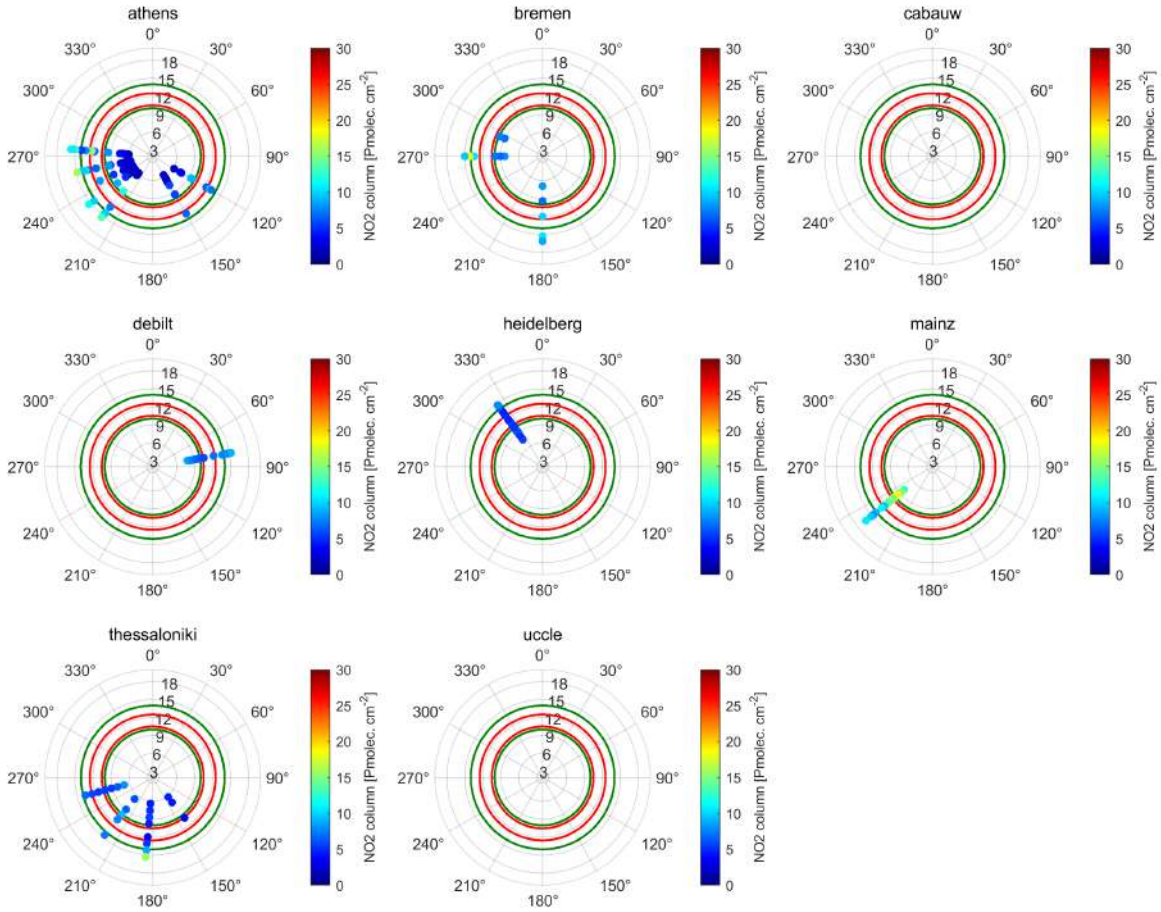

Figure 10: Same as Figure. 6, but on 12.02.2021.

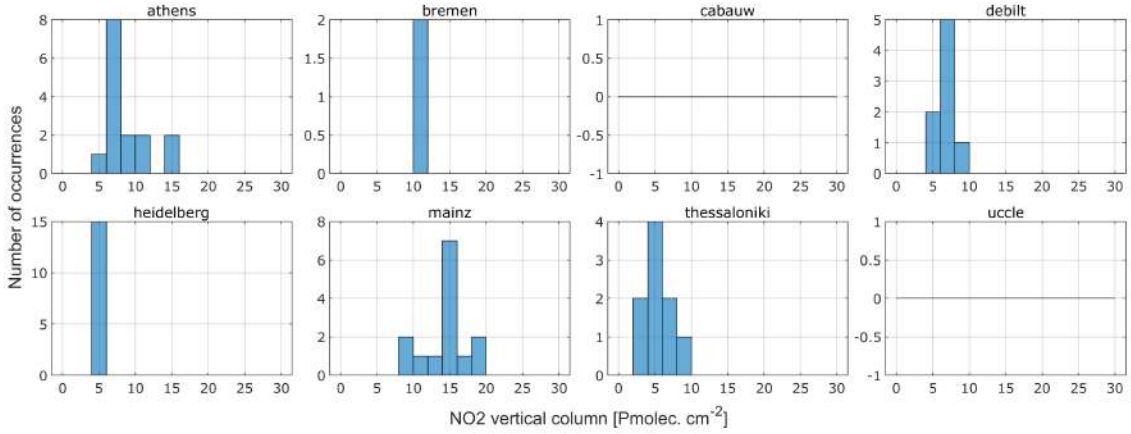

Figure 11: Same as Figure. 7, but on 12.02.2021.

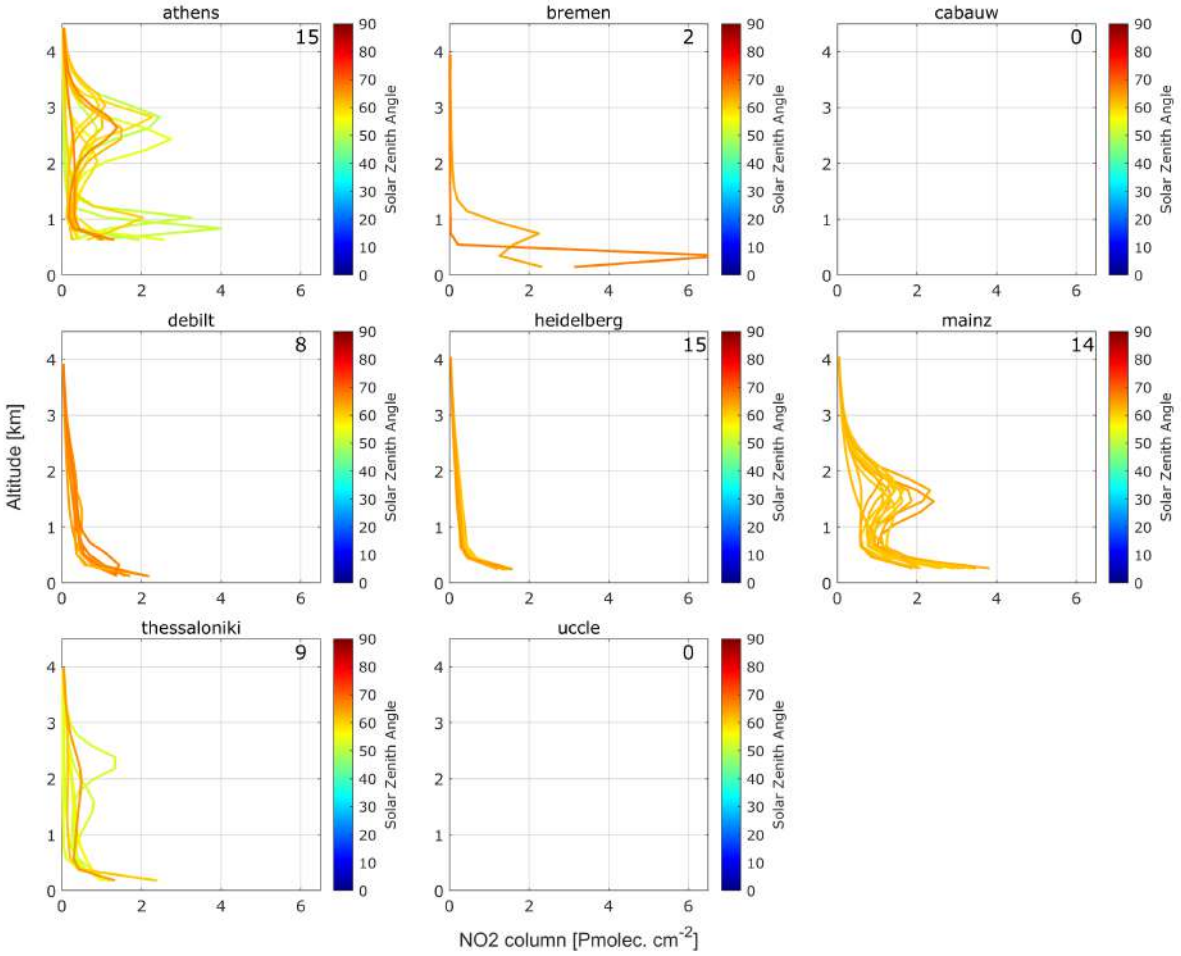

Figure 12: Same as Figure. 8, but on 12.02.2021.

4 Results

This section is divided into three main sub-sections: section 4.1 describes the effect of the different cloud treatments on the synthetic spectra, section 4.2 describes the comparisons between the different DLR S5P/TROPOMI retrievals over all selected MAX-DOAS observations while section 4.3 reports on selected specific cases of cloud shadows affecting the satellite observations.

4.1 Validation based on the synthetic spectra

4.1.1 1D Cloud

First, we evaluate the magnitude of uncertainty associated with traditional cloud correction schemes. By considering this inherent uncertainty, we can better contextualize the errors resulting from the simplified treatment of clouds in scenes with complex 3D cloud structures. Six cloud correction schemes are considered in this study, including FRESCO, O_2-O_2, OCRA/ROCINN CRB, OCRA/ROCINN CRB with adapted scaling for cloud fraction and cloud albedo(=0.8), OCRA/ROCINN CAL and ROCINN CAL with a fixed cloud fraction of 1.

4.1.1.1 Cloud Retrievals

Fig. 13 displays cloud retrievals for 1D liquid cloud cases with different values of surface albedo (ALB), solar zenith angle (SZA), cloud bottom height (CBH), cloud geometrical thickness (CGT) and cloud optical thickness (COT).

In most cases, the cloud fractions obtained from the FRESCO and O_2-O_2 retrievals are very similar; whereas those from the OCRA are consistently higher, except for scenarios with low COT (COT$\leq$2). This discrepancy can be attributed to the different definitions of cloud fraction used in the FRESCO/O_2-O_2 and OCRA retrievals. The FRESCO and the O_2-O_2 effective cloud fractions (FRESCO_*e*CF) are similar because both retrievals assume a fixed cloud albedo (CA) of 0.8. The OCRA radiometric cloud fraction (OCRA_*r*CF) retrieval does not make such assumptions and the cloud albedo is retrieved with the ROCINN algorithm. These quantities are related by FRESCO_eCF * CA $\simeq$ OCRA_rCF * CA. On global average the CA is around 0.2-0.3, therefore the FRESCO and the effective cloud fractions are lower to compensate the O_2-O_2 assumed CA of 0.8. As a result, the cloud optical thickness obtained from the ROCINN CRB retrieval is systematically lower. It should be noted that the OCRA cloud fraction plays a crucial role in the retrieval of cloud albedo and cloud optical thickness in ROCINN. The ROCINN CAL cloud heights are generally higher than those obtained from the other cloud retrievals. The retrieved CAL cloud height is close to the cloud top height, while the Lambertian cloud retrieval provides cloud height estimates corresponding to the middle of the clouds. The ROCINN CAL retrievals using "*cfmask*" and "*cfocra*" cloud fractions are very close. There is an outlier (SZA=80°) for ROCINN CAL retrieval using "*cfocra*" cloud fraction. This is probably because the current retrieval algorithm does not account for such a large range of solar zenith angles.

For the "*cfmask*" cloud fraction model, the retrieved COT is very close to the synthetic truth, while the COT retrieval using "*cfocra*" cloud fraction is relatively higher.

Furthermore, the presence of outliers in ROCINN retrievals for low COT cases (COT$\leq$2) may be attributed to the insensitivity of the OCRA cloud fraction retrieval towards situations with low COT. It should be noted that OCRA determines the cloud fraction based on how much the TOA reflectances differ from the expected TOA reflectances under clear-sky conditions. With this definition, it is not easy to discriminate if the TOA reflectance discrepancy is caused by a fully-cloudy scene with small COT or a partially-cloudy scene with high COT. For limit cases with low COT, it can be observed that the OCRA radiometric cloud fraction tends to be much lower than the geometric cloud fraction, and this discrepancy needs to be compensated later in ROCINN by retrieving a higher COT than the value in reality. Future research paths could include updates or improvements in the OCRA cloud fraction retrieval so that it resembles the geometric cloud fraction better for the majority of standard remote sensing scenes.

Fig. 14 shows cloud retrievals for 1D ice cloud cases, and the results are very similar to the liquid cloud cases. It is worth noting that the ROCINN cloud retrieval is solely based on liquid cloud assumption, which may introduce uncertainties for ice cloud scenarios due to an incorrect forward model selection. Nevertheless, the most important thing is that the NO_2 AMF calculation is based on the same assumption as the cloud retrievals.

Strictly speaking, when using a Lambertian cloud model approach, only thick clouds can be accurately represented. However, in order to improve the calculation of the NO_2 AMF using OCRA/ROCINN CRB cloud correction, an effective cloud fraction can be defined by calculating an effective cloud albedo of 0.8 (CF=CF·CA/0.8, and CA=0.8). This approach helps to transform optically thin clouds into equivalent optically thick clouds of reduced extent, thus improving the accuracy of cloud representation in the CRB model.

4.1.1.2 Box-AMF

In this study, the main focus is on the effect of 3D clouds. Therefore, radiative transfer model settings in the NO_2 and cloud retrievals are made as consistent as possible with those used to generate the synthetic datasets. In the 1D cloud scene, the differences between the NO_2 retrieval and truth (as imposed in the synthetic data) mainly come from the simplified cloud correction approach used in the calculation of the AMF. In order to assess the uncertainty of cloud correction schemes, we apply the NO_2 retrievals with various cloud correction approaches to 1D cloud cases.

Fig. 15 shows the results of the box-AMFs using various cloud corrections for liquid and ice cloud base cases, as well as the true AMF calculated by MYSTIC. The retrieved cloud heights are inside the cloud for all cloud retrievals. The box-AMFs are very similar above and below the cloud layer, with slightly large differences in the box-AMFs calculated using the OCRA/ROCINN CRB cloud correction.

Fig. 16 and Fig. 17 display the box-AMFs using different cloud corrections depending on the parameters discussed in Sect. 4.1.1.1, for liquid cloud and ice cloud, respectively. The box-AMFs demonstrate a high degree of similarity across all cloud correction approaches for liquid cloud cases, whereas the differences are relatively larger for ice cloud cases. This is mainly due to the large difference in cloud height retrievals.

4.1.1.3 NO_2 AMF

The standard NO_2 retrievals, employing various cloud correction approaches, have been applied to the synthetic spectra using a polluted NO_2 profile from the Northern China region. In order to examine the impact of cloud correction, the AMF values from the retrieval are compared with their corresponding true values.

Fig. 18 shows the biases of the NO_2 AMF for various ALB, SZA, CBH, CGT, and COT. The biases are typically below 20%, except for cases with high SZA (¿60°) and for retrievals using OCRA/ROCINN CRB cloud correction. Furthermore, the biases for the retrievals using cloud correction based on ROCINN CAL and "*cfmask*" cloud fraction mode are consistently close to 0 in most cases, as the cloud retrieval mode closely resembles the synthetic settings. For larger solar zenith angles, the treatment of cloud can be improved by modifying the assumption of Lambertian albedo values, though this approach requires further investigation. Additionally, incorporating a scattering cloud model could enhance cloud correction, which necessitates accurate cloud properties information.

Fig. 19 shows the results using a profile from the region with relatively low pollution, where the NO_2 biases are generally lower compared to those using Northern China NO_2 profile.

4.1.2 2D Box-cloud

In reality, the cloud-affected scenes are usually complex, many cloud effects come together that are difficult to distinguish. In order to investigate the influence of the different 3D cloud effects on NO_2 retrievals, we start with simple box cloud cases and investigate the NO_2 retrievals around the cloud edge.

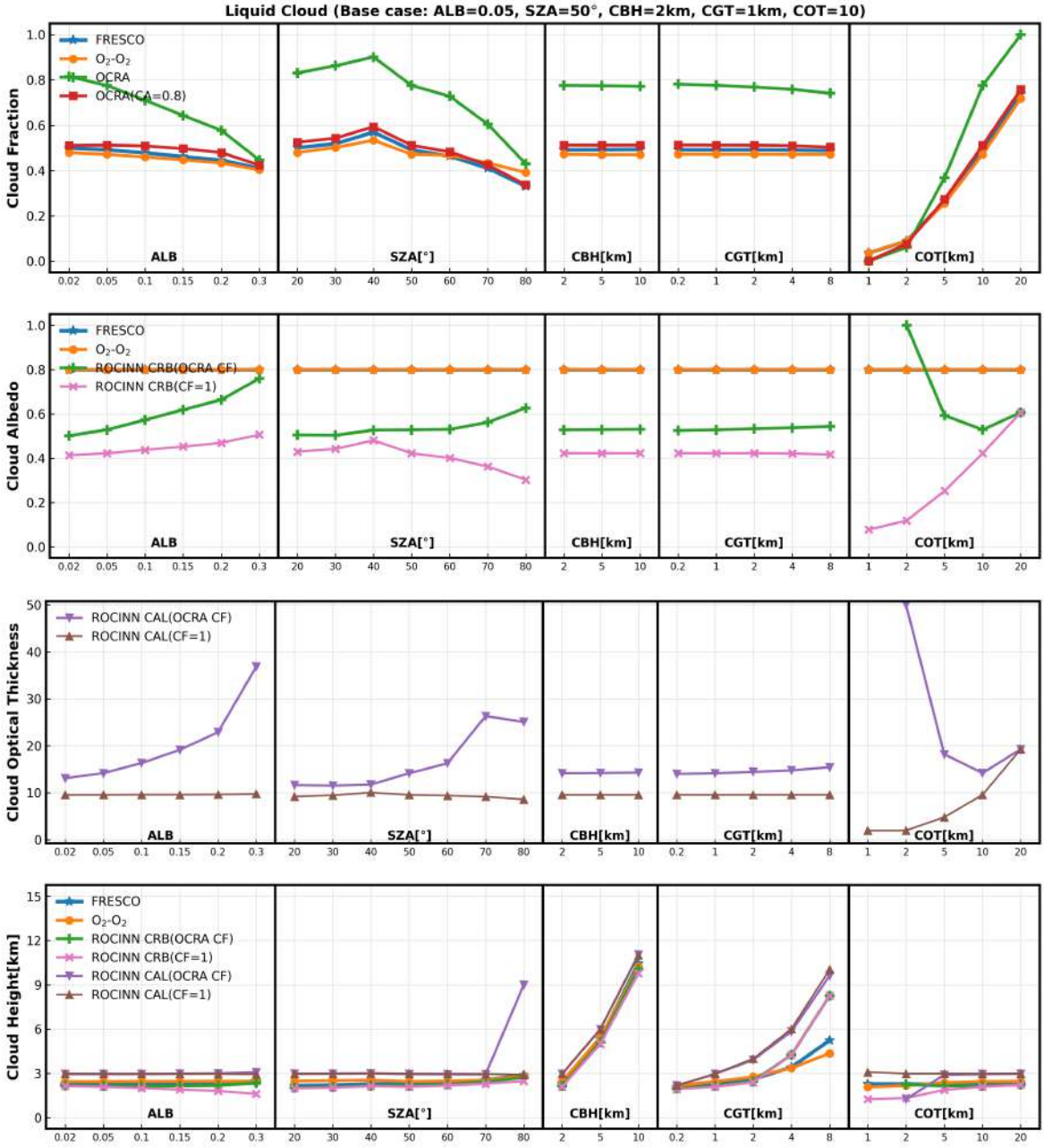

Figure 13: Cloud retrievals for a series of 1D liquid cloud cases

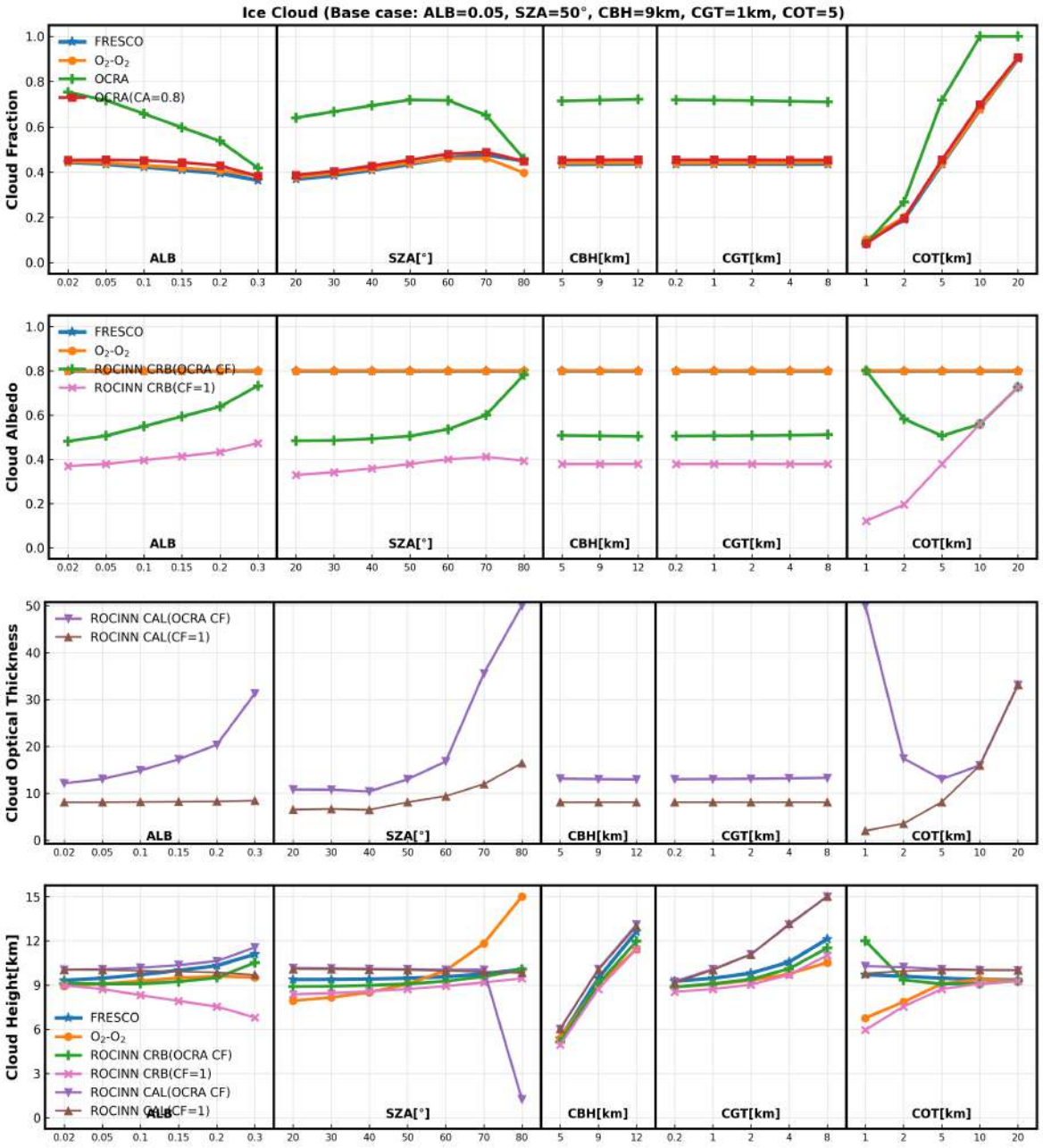

Figure 14: Similar as Fig. 13, but for 1D ice cloud cases

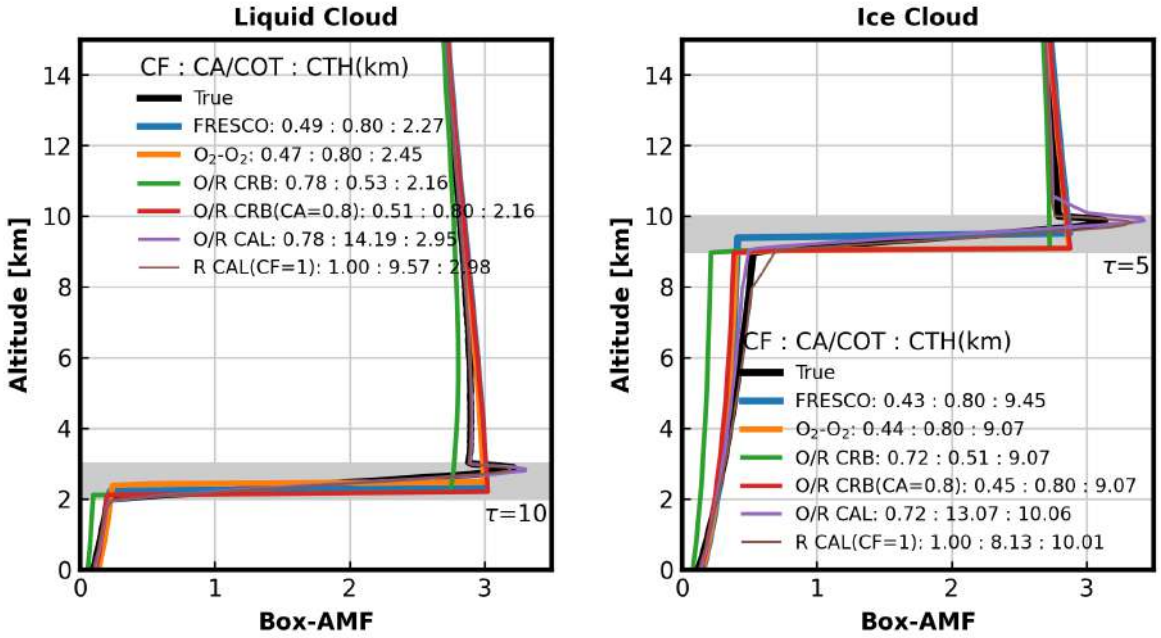

Figure 15: Box-AMFs using different cloud correction methods for liquid (optical thickness τ=10, cloud height at 2-3km, left) and ice (optical thickness τ=5, cloud height at 9-10km, right) cloud base cases. The gray area represents the true cloud layer. The black line represents the true box-AMFs simulated by MYSTIC, while the other colors correspond to the box-AMFs calculated using various cloud corrections. The legends indicate the cloud retrieval results, including cloud fraction, cloud top albedo/optical thickness, and cloud top height.

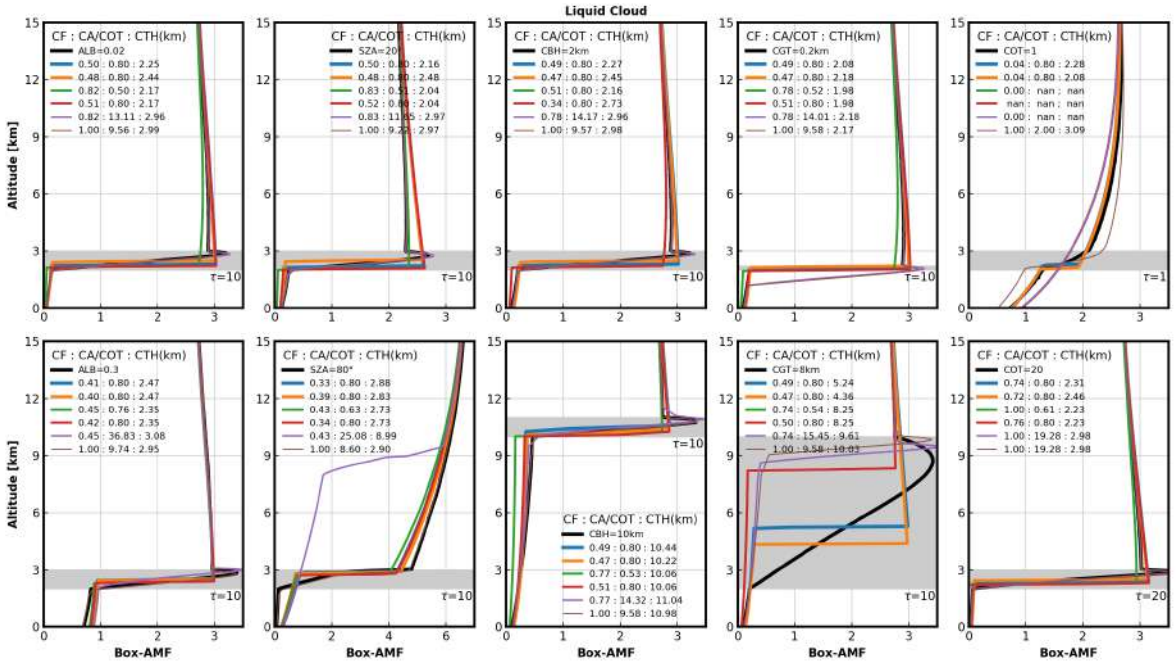

Figure 16: Similar to Fig. 15, but for liquid cloud cases with different ALB (0.02 and 0.3, 1st column), SZA (20° and 80°, 2nd column), CBH (2 and 10 km, 3rd column), CGT (0.2 and 8 km, 4th column) and COT (1 and 20, 5th column). The gray area represents the true cloud layer. The black line represents the true box-AMFs simulated by MYSTIC, while the other colors correspond to the box-AMFs calculated using various cloud corrections. The legends indicate the cloud retrieval results, including cloud fraction, cloud top albedo/optical thickness, and cloud top height. The results show that most of the retrieved cloud heights are close to the midlevel of the clouds.

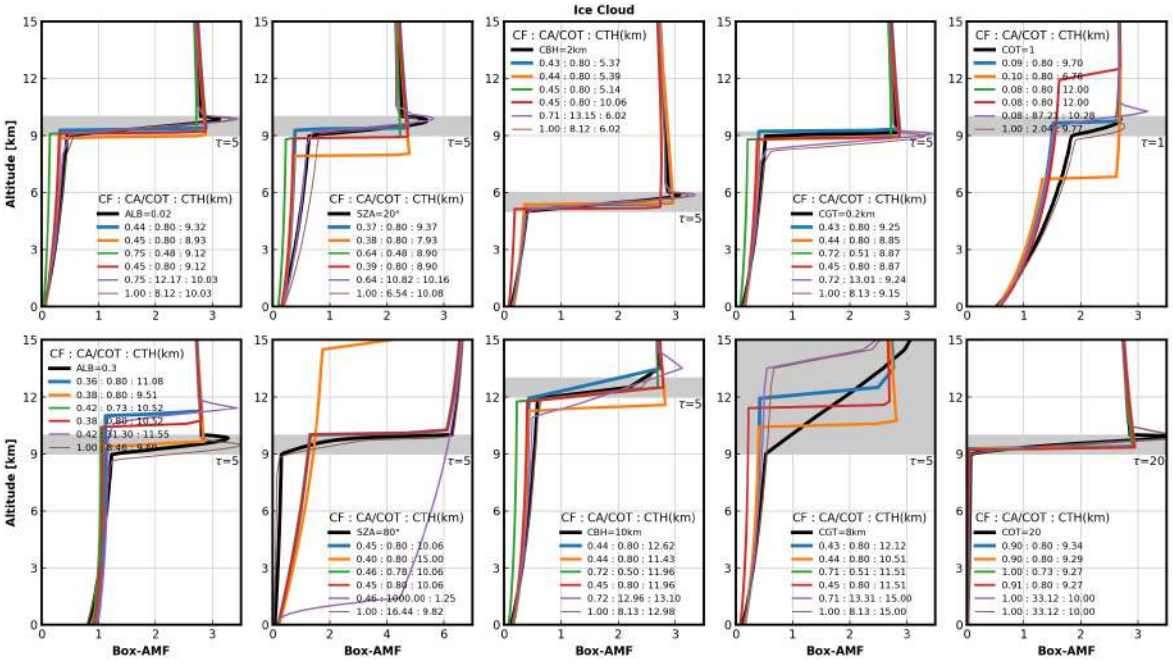

Figure 17: Similar to Fig. 16, but for ice cloud cases.

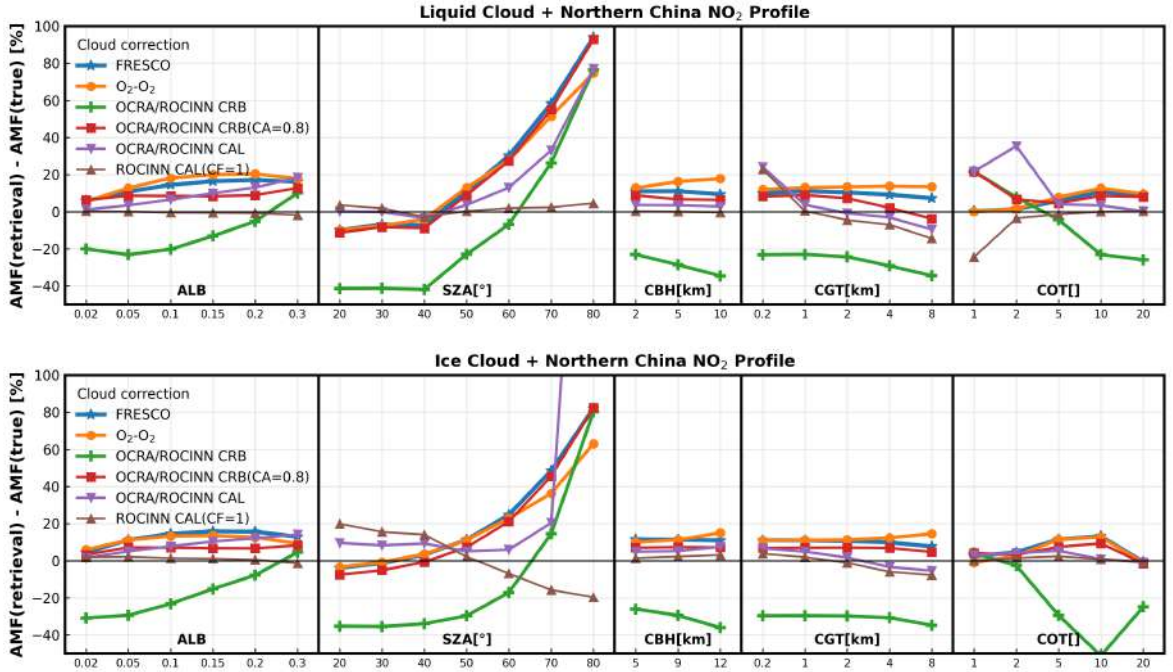

Figure 18: NO_2 AMF bias for all 1D cloud cases (top panel: liquid cloud; bottom panel: ice cloud). The AMF bias is defined as (AMF(retrieval)–AMF(true))/AMF(true)·100%. A NO_2 profile from the polluted Northern China region is used, the different colors correspond to the box-AMFs calculated using various cloud corrections.

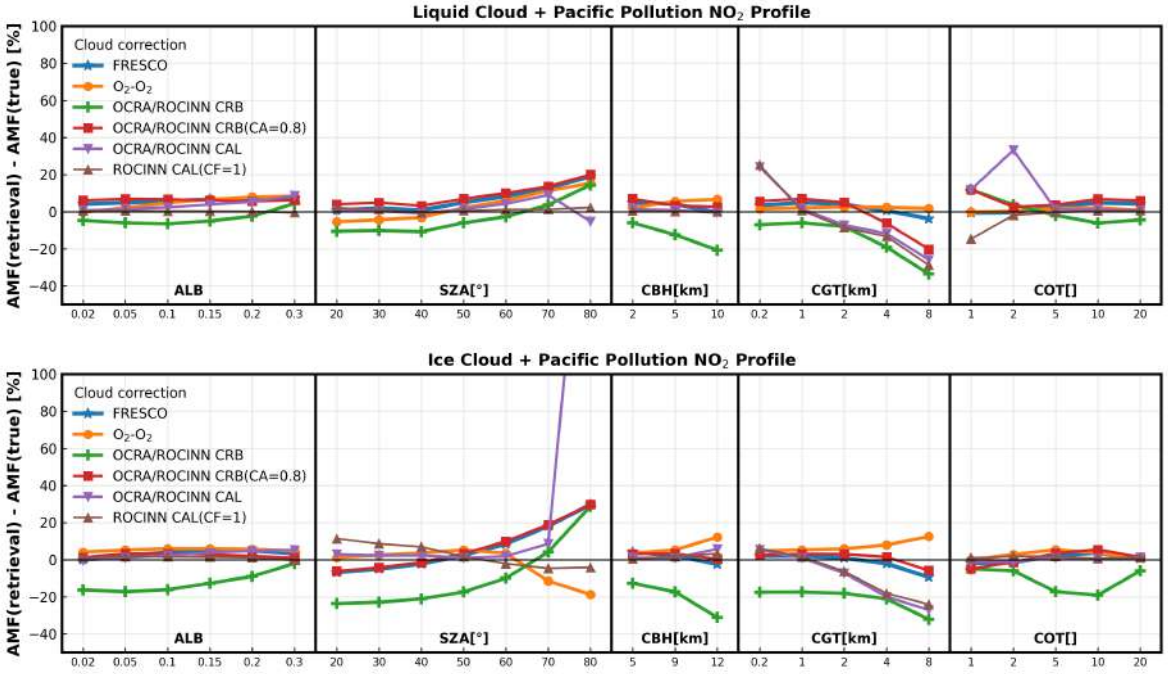

Figure 19: Similar to Fig.18, but a NO_2 profile from the polluted Pacific region is used.

4.1.2.1 Cloud Retrievals

All cloud retrievals have been applied to the synthetic spectra with a box-cloud. Fig. 20 illustrates the results for the liquid cloud base case, while Fig. 21 presents the results for the ice cloud base case.

The left plot displays the retrievals in the in-scattering region. For the cloudy pixels (positive distance values on the x-axis), the cloud retrievals closely resemble those for the corresponding 1D cloudy scene, with a slight dependency on the distance from the cloud edge. For the clear pixels (negative distance values), the retrieved cloud fraction is zero, except for FRESCO and O_2-O_2 retrievals near the cloud edge, which is due to the enhanced reflectance resulting from scattering into the clear region. In such cases, the retrieved cloud heights are lower than those of the neighboring cloudy pixels.

The right panel shows the results in the cloud shadow region. The cloud retrievals are usually very similar to those for the corresponding 1D scene, except for the pixels around the cloud edge. In the cloud shadow region, the cloud fractions from FRESCO and O_2-O_2 retrievals are negative due to the decreased reflectance, while the OCRA/ROCINN retrieval consistently classifies clear pixels as cloud-free (i.e. cloud fraction = 0).

4.1.2.2 NO_2 Retrieval

Fig. 22 shows the bias of the NO_2 AMF due to cloud in-scattering and shadowing. In the in-scattering region (left panel of Fig. 22), a negative or positive bias is observed for a few pixels next to the cloud edge, and these biases typically fall within the range of ±20%. The bias of NO_2 retrievals shows a strong dependency on the distance from the cloud edge for the cloudy pixels.

The reflectance in the cloud shadow region is lower than that of clear sky conditions. As a result, the retrieved cloud fraction is 0 for all cloud products, and the calculated AMF corresponds to the AMF for a clear sky. This leads to a significant bias (up to 100%) in the NO_2 retrieval within the cloud shadow area. The NO_2 bias over the cloudy pixels shows a slight dependence on the distance from the cloud edge, and the values are very close to those obtained from the corresponding 1D cloud scene.

In order to study the dependence of the NO_2 AMF bias due to the cloud shadowing/in-scattering for the

parameters defined in the synthetic data. The NO_2 retrieval bias at the selected positions (distance = -0.5, 0.5, and 10.5 km) is plotted as a function of various parameters. The results are shown in Fig. 23 for the in-scattering cases and Fig. 24 for the shadowing cases, respectively.

The largest biases are typically observed in the cloudy pixels located at the edge of the cloud in the in-scattering cases. On the other hand, in the cloud shadowing cases, the largest biases are found in the clear pixels at the edge of the cloud. For the remaining positions, the biases are generally small and mostly within a range of 20%.

4.1.3 3D LES cloud

To delve into how 3D cloud scattering affects NO_2 retrievals across real-world data, we applied the cloud retrievals and NO_2 AMF based on these cloud corrections to the simulations with LES data.

Fig. 25 shows retrievals for a LEO case (ALB=0.05, SZA=40°, SAA=13°, VZA=0°, VAA=109.5°). It's worth noting that the complete cloudy pixels are excluded from the analysis, since satellite NO_2 retrieval mainly focuses on the nearly cloud-free scenes. In OCRA/ROCINN, the CRB retrieval reveals the effective cloud fraction (which equals CF·CA/0.8), while the CAL retrieval shows cloud optical thickness scaling by cloud fraction. When it comes to cloud height retrievals, we are only showing pixels with the cloud fraction retrieval larger than 0.01. In OCRA/ROCINN CAL retrieval, cloud height is provided as the top of the cloud. The NO_2 AMF calculation is applied to all pixels with valid cloud retrievals. Fig. 27 shows pixel-by-pixel difference of cloud retrievals and bias of NO_2 AMF based on various cloud corrections.

The cloud fraction/cloud optical thickness retrievals demonstrate good agreement (first column in Fig. 25), despite the OCRA/ROCINN CAL retrieval providing a different parameter. In the cloud height retrievals, the O_2-O_2 cloud height appears higher than FRESCO and OCRA/ROCINN CRB in scenarios with low clouds (cloud height $<$ 3km) and lower in situations with high clouds (cloud height $>$ 6km). The OCRA/ROCINN CAL cloud height typically appears higher than the other three products. It is important to note that there are differences in the definition of cloud height between OCRA/ROCINN CAL and the other retrievals. In the OCRA/ROCINN cloud height retrievals, both CRB and CAL models exhibit outliers (Fig. 27) where the retrieved cloud heights approximate 9 km, closely resembling the initial cloud height values used in fitting. This anomaly likely stems from convergence issues in nearly cloud-free scenes. However, this impact on the AMF calculation is minimal.

The bias of NO_2 AMF based on various cloud corrections, as illustrated in the third column of Fig. 25, remains generally minimal, with only a few pixels exhibiting significant differences, particularly those near the cloud edge. The mean AMF bias for all LEO scenarios (Fig. 26) shows similar result, with most of values being positive. It implies that the 3D cloud effects are primarily influenced by cloud shadowing effects.

4.1.4 Treatment of 3D cloud effects

The surrogate cloud method is introduced by smoothing the cloud fraction field to account for the 3D cloud effects. In the trace gas retrieval algorithm, all steps remain consistent with the standard approach, except for the alteration of the cloud fraction by the smoothed value.

In order to assess the surrogate cloud method in correcting for 3D cloud effects, The liquid cloud base case from the 2D-box cloud scenario is used. The NO_2 retrieval based on various cloud correction approaches is tested, and the width of the smoothed kernel is 3 and 5km. Fig. 28 shows the results based on the NO_2 retrieval using scaled OCRA/ROCINN CRB cloud correction. Noticed that in this case, the cloud pressure values in the clear regions are obtained from the neighboring cloudy pixels, as there is no cloud pressure retrieval when the cloud fraction is 0. After smoothing, the cloud fraction is reduced in the cloudy regions and increased in the clear regions compared to the original values. While AMF biases are diminished for some pixels near the cloud edge, some biases persist, particularly over the clear region. The results for the NO_2 retrieval based on the other cloud corrections yield very similar outcomes (not shown).

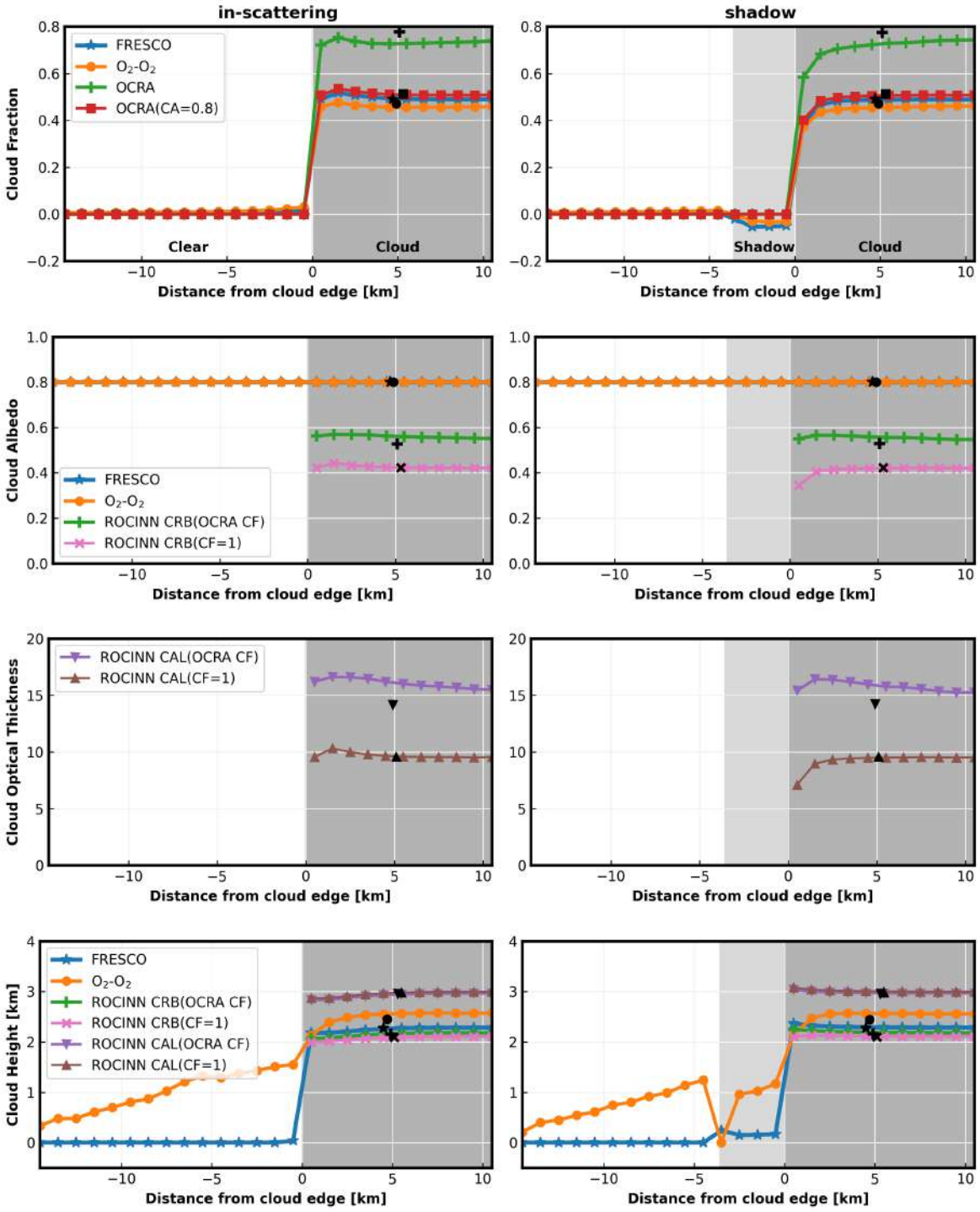

Figure 20: Cloud retrievals (1st row: cloud fraction; 2nd row: cloud albedo; 3rd row: cloud optical thickness; 4th row: cloud height) for liquid box-cloud base case as a function of the distance from the cloud edge. Negative values refer to clear pixels, positive values correspond to cloudy pixels (shown as dark grey regions), and the light grey area within the clear region denotes the cloud shadow region. The left panel shows the in-scattering region while the right panel displays the cloud shadow. Different cloud retrievals are denoted by various colors while the black symbols represent the retrievals for corresponding 1D cloud scenes. The FRESCO and O_2-O_2 cloud albedo values are not obtained through the retrieval process; instead, they are assumed to have a fixed value of 0.8. Negative cloud fractions are allowed in the FRESCO and O_2-O_2 retrievals. The ROCINN retrievals are not activated if the OCRA cloud fraction is less than 0.05.

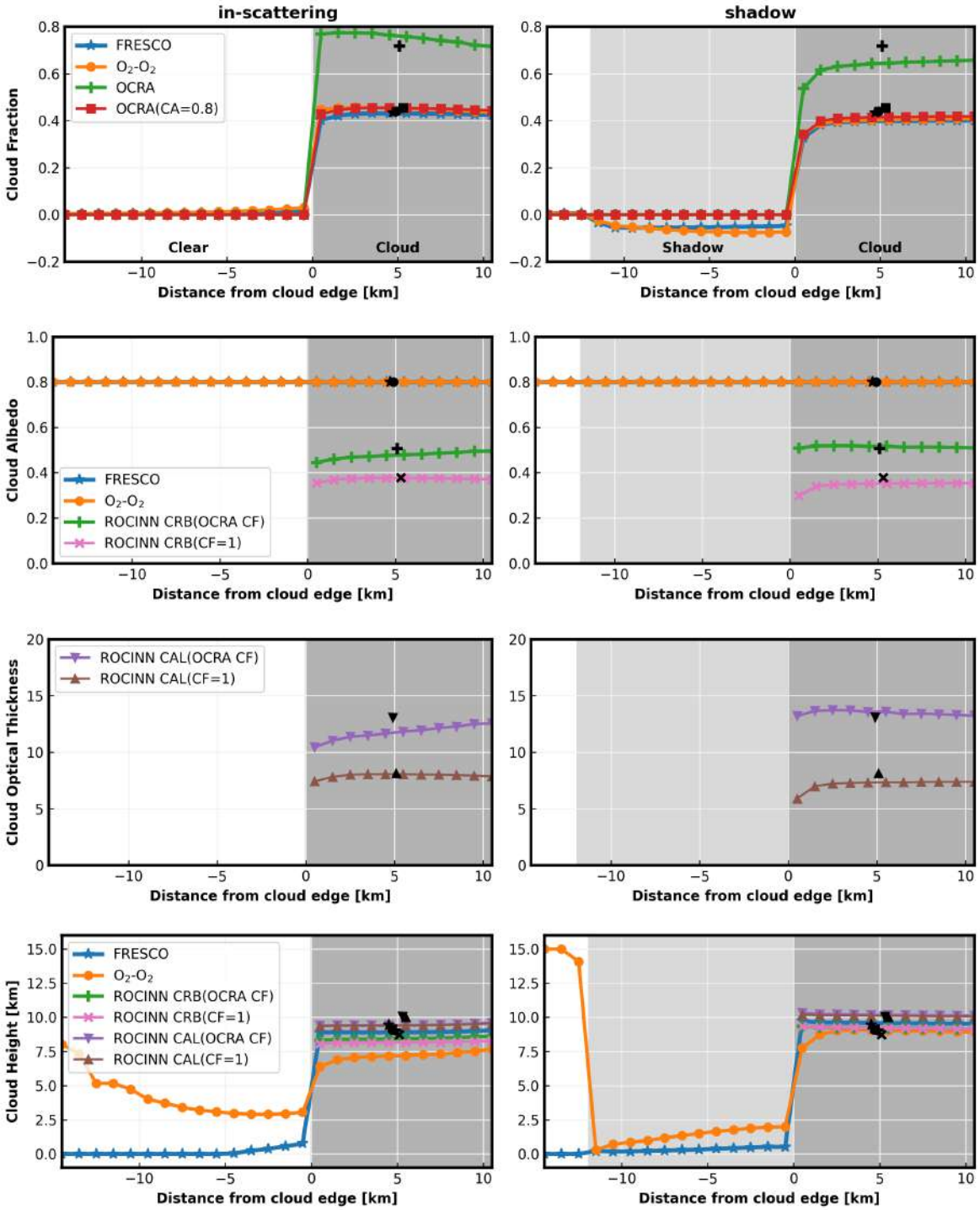

Figure 21: Similar to Fig. 20, but for the ice cloud base case.

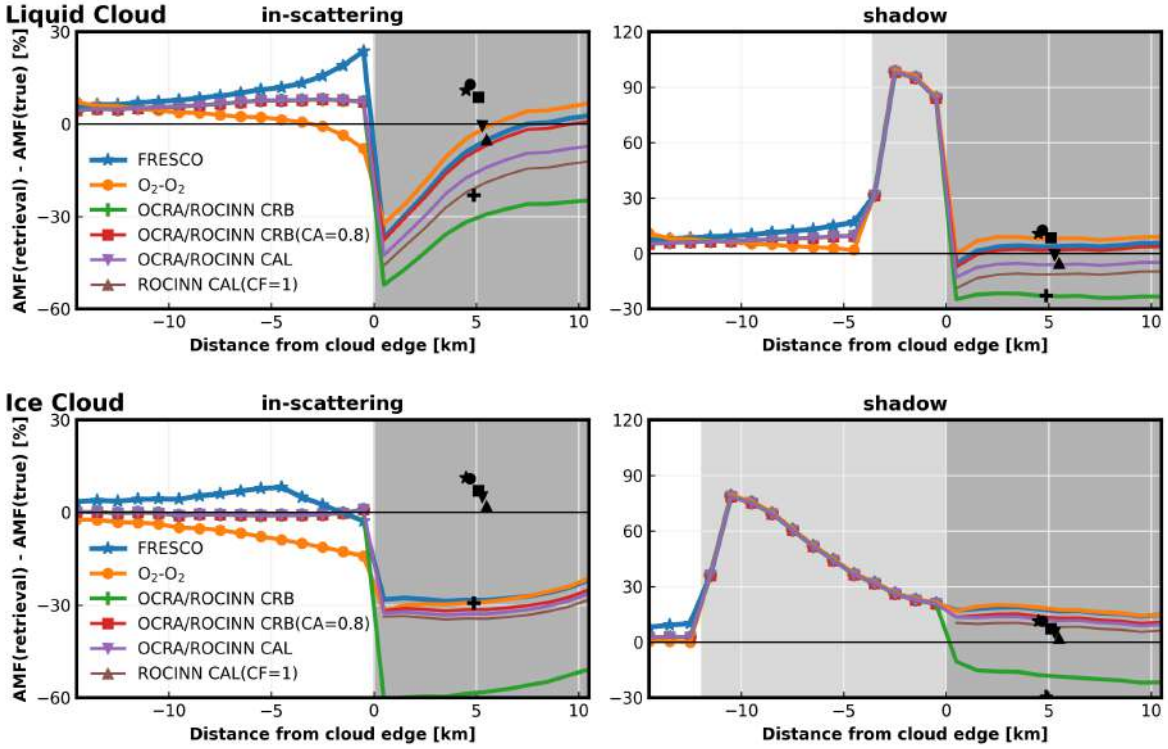

Figure 22: NO_2 AMF bias as a function of distance from the cloud edge, with negative distances indicating clear pixels (white regions), positive distances indicating cloudy pixels (dark grey regions), and the light grey regions corresponding to the cloud shadow region. The left and right panels depict in-scattering and shadow cases, respectively. The various colors represent the bias of the NO_2 AMF obtained using different cloud corrections, while the colored symbols indicate pixels with a cloud radiance fraction less than 50%. The black symbols correspond to the retrievals for a corresponding 1D cloud scene.

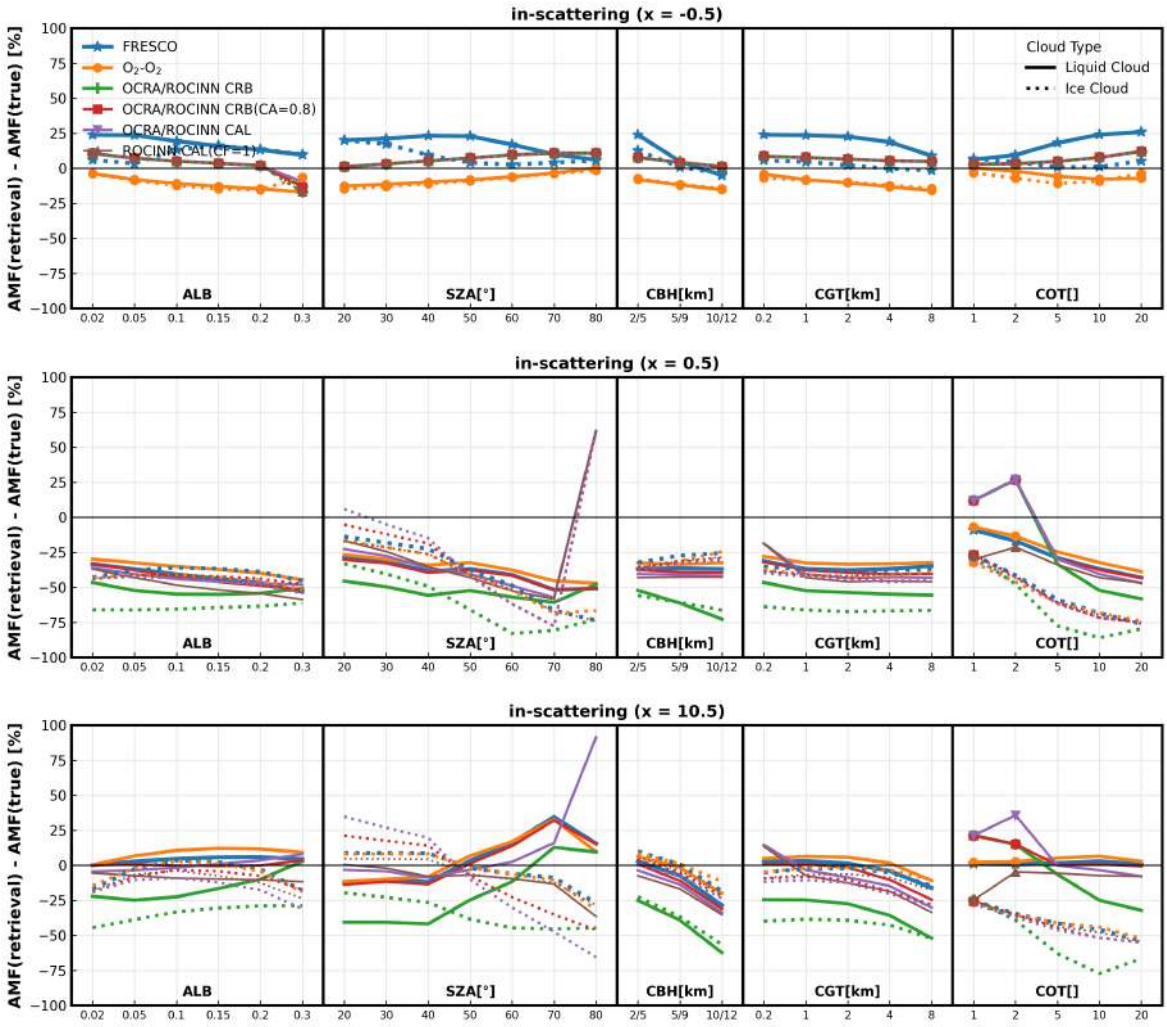

Figure 23: NO_2 AMF bias at different locations of the in-scattering region, for different surface albedos, solar zenith angles, cloud bot-tom heights, cloud geometrical thicknesses, and cloud optical thicknesses.

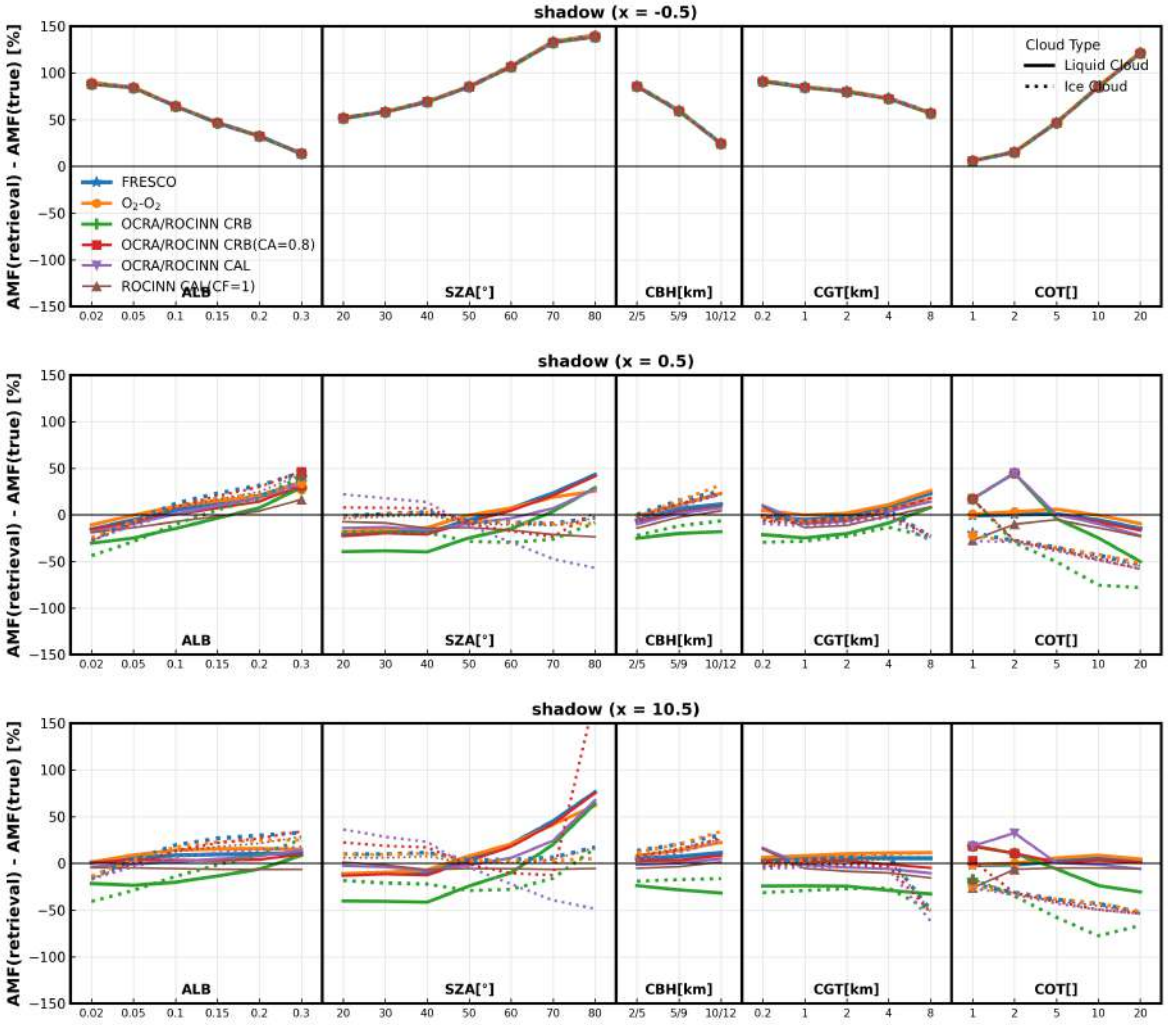

Figure 24: Similar to Fig. 23, but for the cloud shadow region.

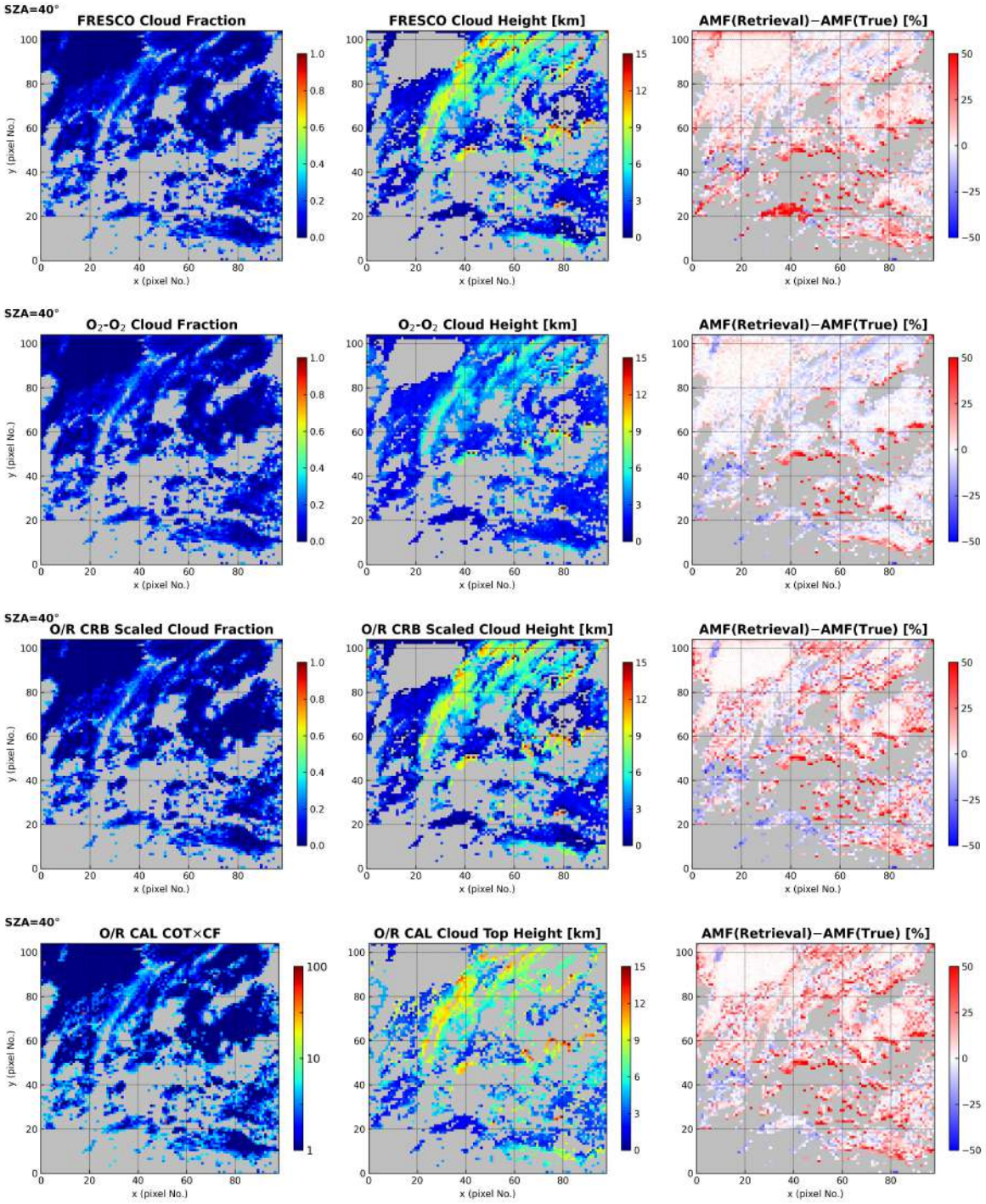

Figure 25: Examples of cloud retrievals and the errors of NO_2 AMF based on different cloud corrections (for a LEO geometry case with ALB=0.05, SZA=40°, VZA=0°). 1st row: FRESCO cloud retrieval; 2nd row: O_2-O_2 cloud retrieval; 3rd row: OCRA/ROCINN CRB cloud retrieval with scaled cloud fraction; 4th row: OCRA/ROCINN CAL cloud retrieval. 1st column: effective cloud fraction or cloud optical thickness; 2nd column: cloud height (in OCRA/ROCINN CAL retrieval denote cloud top height); 3rd column: difference between the calculated AMF and actual value.

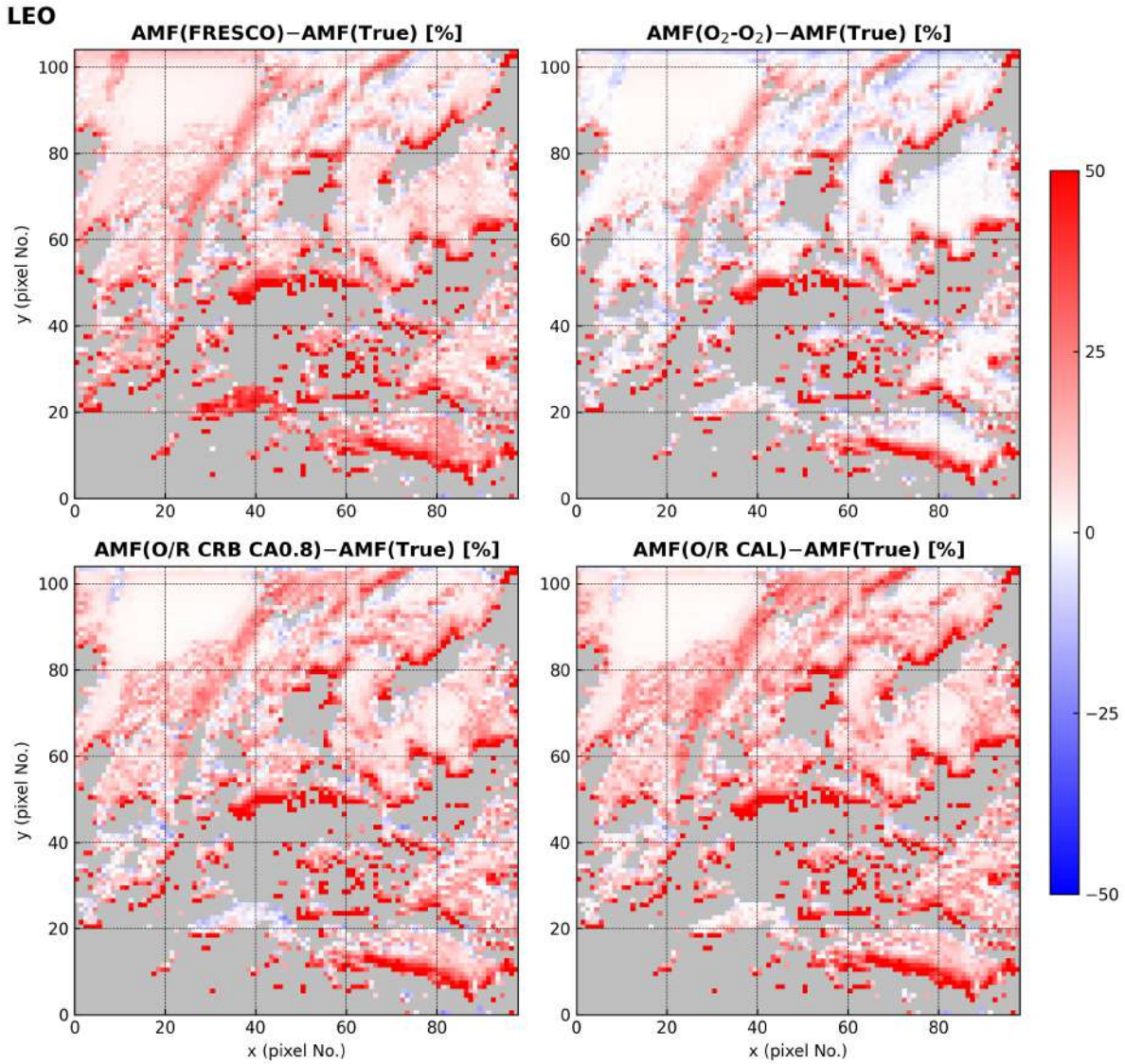

Figure 26: The mean bias of the NO_2 AMF based on various cloud corrections for all LEO cases.

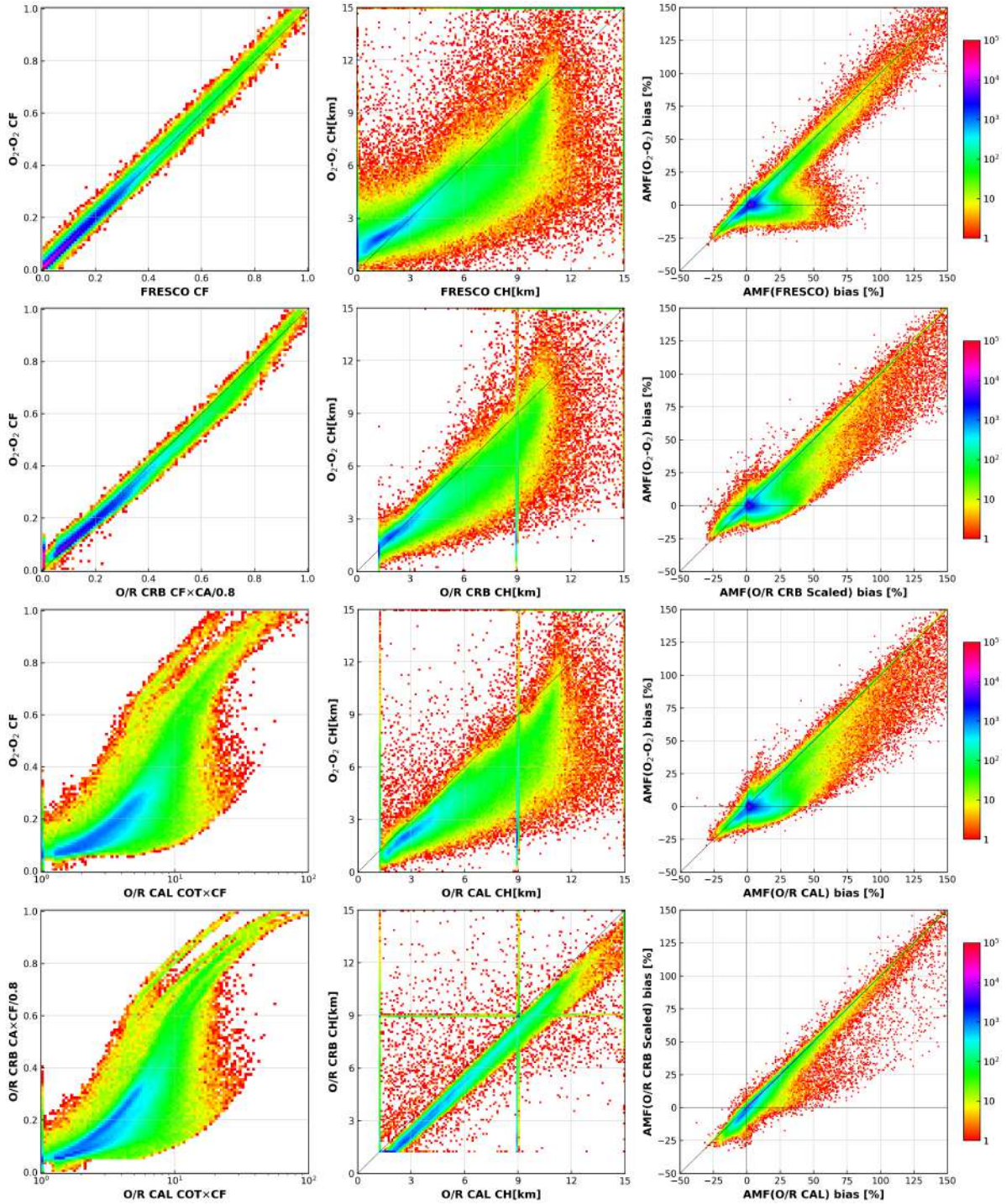

Figure 27: Comparison of cloud retrievals and bias of NO_2 AMF based on different cloud corrections for all GEO/LEO cases. 1st row: O_2-O_2 vs. FRESCO; 2nd row: O_2-O_2 vs. OCRA/ROCINN CRB; 3rd row: O_2-O_2 vs. OCRA/ROCINN CAL; 4th row: OCRA/ROCINN CRB vs. OCRA/ROCINN CAL. 1st column: effective cloud fraction or cloud optical thickness; 2nd column: cloud height; 3rd column: bias of NO_2 AMF.

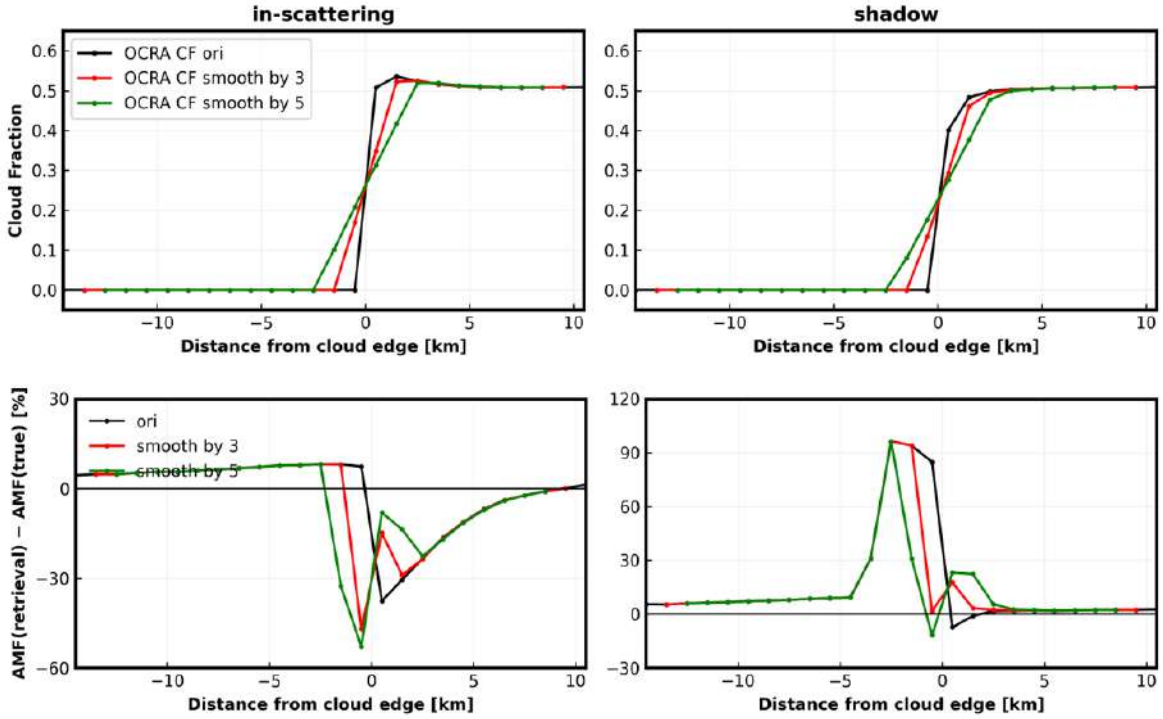

Figure 28: Treatment of 3D cloud effects by surrogate cloud method. The liquid cloud base case from the 2D-box cloud scenario is used, the NO_2 AMF calculation is performed based on the scaled OCRA/ROCINN CRB cloud correction. Top panel: Effective cloud fraction (black line) from OCRA/ROCINN and smoothed values, the width of the smoothed kernel is to 3km (red line) and 5km (green line); bottom panel: the bias of NO2 AMF based on various cloud fractions.

4.2 Validation based on the S5P/TROPOMI observations against MAX-DOAS collocations

4.2.1 Comparison methodology

For the comparison between the satellite and the ground-based MAX-DOAS instruments, TROPOMI data within a radius of 20 km around the selected European stations, listed in Table 1, were extracted, after filtering the data by NO2TropCorrection_Flag = 1, and discarding satellite pixels with a cloud fraction > 50%. While the MAX-DOAS instruments probe air masses along the line of sight and they are more sensitive to local emissions, the NO_2 columns that are reported by TROPOMI are essentially averaged over the sub-satellite pixel area, resulting, generally, in underestimation of the actual NO_2 levels [e.g. Griffin et al., 2019, Dimitropoulou et al., 2020, Zhao et al., 2020], which is more evident in highly polluted and in extremely highly polluted environments [Verhoelst et al., 2021]. In order to compensate for the larger satellite footprint, for each TROPOMI overpass, only the pixel with the minimum horizontal distance from the ground-based station is selected. Based on sensitivity tests for all sites, this approach was found to produce slightly better comparison results than using the mean NO_2 column of all pixels within 20 km. This choice was especially important for cities like Thessaloniki which has a coastal orientation (Figure 3), where the NO_2 load is higher in the urban area (where the MAX-DOAS is also located), compared to the sea region. This can also be seen in Figure 29 which shows the effect on the mean tropospheric NO_2 when increasing the distance between station location and central TROPOMI pixel.

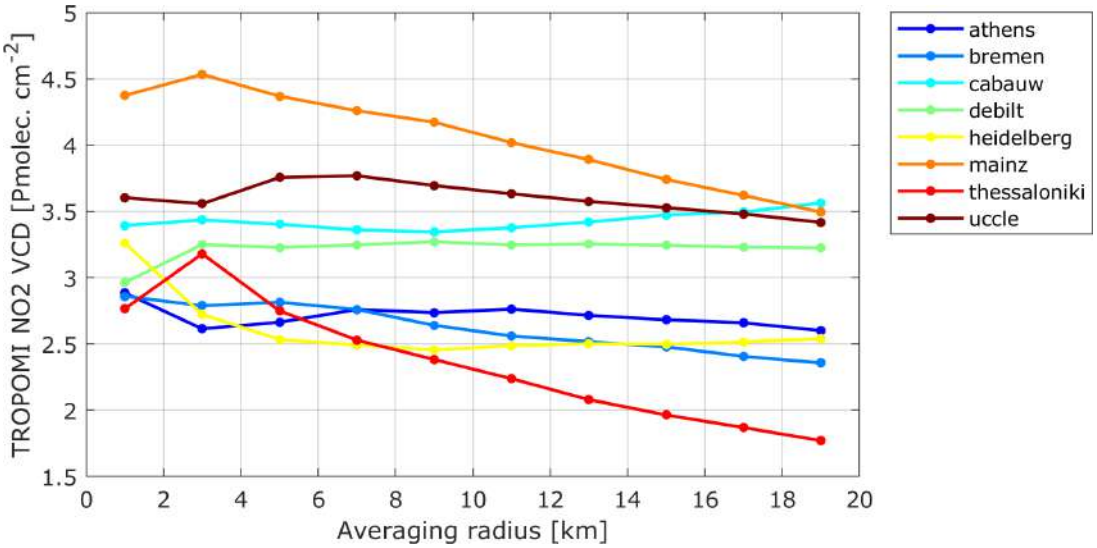

Figure 29: Mean TROPOMI tropospheric NO_2 column as a function of the averaging radius around the overpass location for all stations.

The temporal collocation criterion for the satellite and the ground-based instruments is adapted from Pinardi et al. [2020], i.e., the MAX-DOAS data are temporally interpolated to the TROPOMI overpass time (only if data within ± 1h exist). This criterion avoids large interpolation errors and ensures that no photochemical adjustments have to be applied. This approach was followed also by other NO_2 validation studies [e.g. Liu et al., 2021, Verhoelst et al., 2021]. Sensitivity tests using the temporally averaged MAX-DOAS NO_2 VCDs around ± 1h from the TROPOMI overpass time were performed, but no significant effect on the comparison results is found.

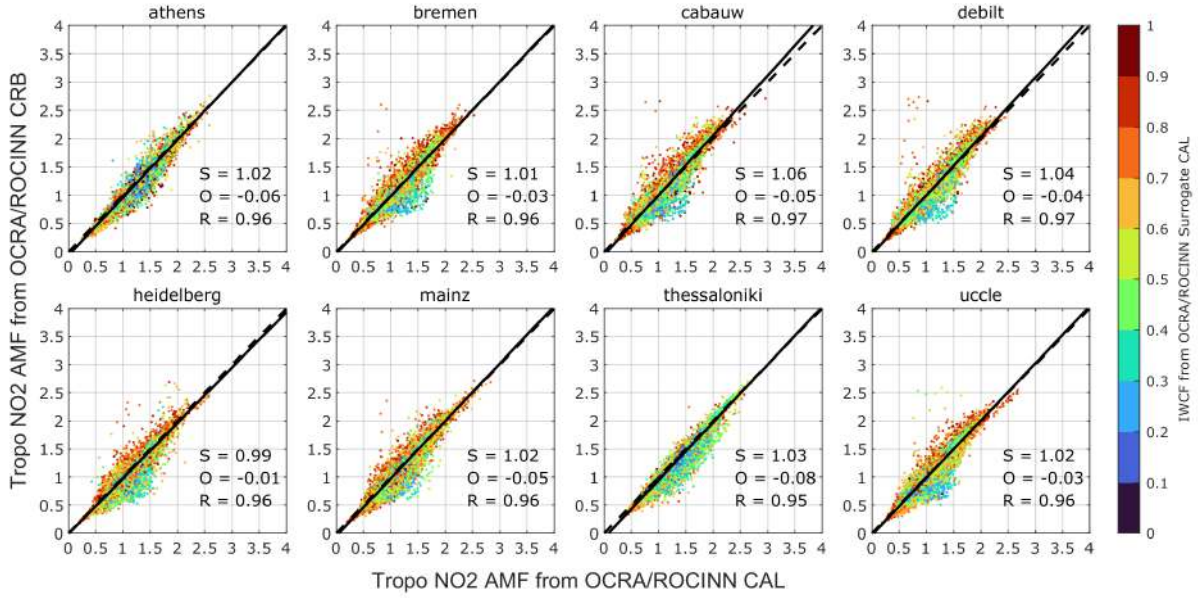

Figure 30: Scatter plots of the tropospheric AMF using CAL and CRB cloud treatments for all stations. The data are colored by the Intensity Weighted Cloud Fraction. The dashed black line represents the 1:1 line.

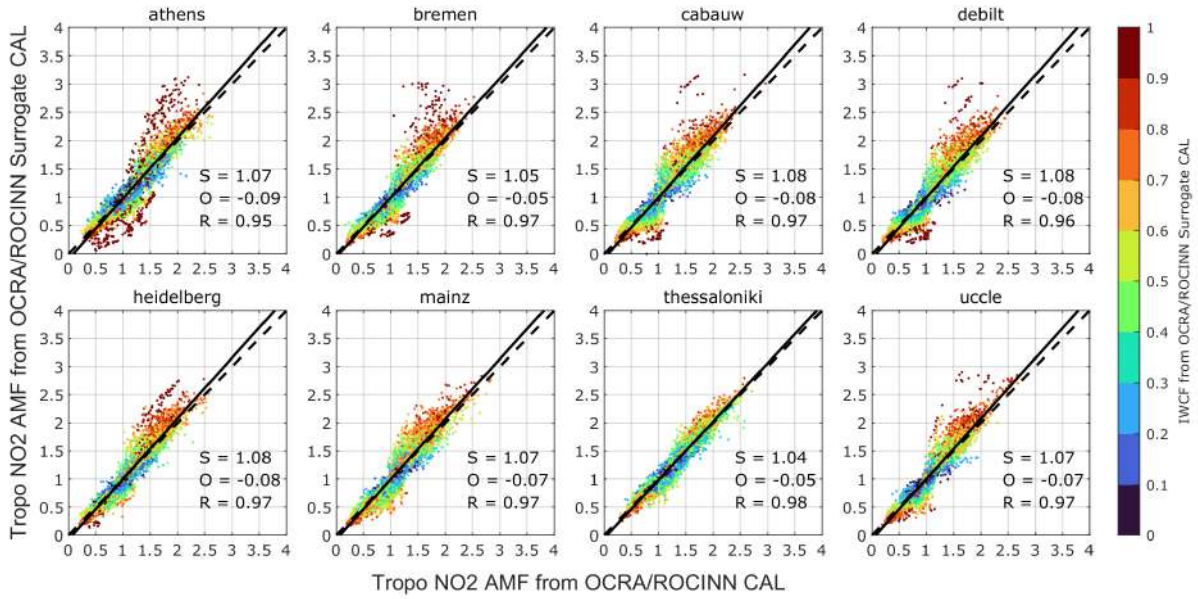

Figure 31: Scatter plots of the tropospheric AMF using CAL and CAL surrogate cloud treatments for all stations. The data are colored by the Intensity Weighted Cloud Fraction. The dashed black line represents the 1:1 line.

4.2.2 Assessment of the CRB, CAL and CAL surrogate model cloud treatments

The comparison of the tropospheric Air Mass Factor (AMF) using the CRB and CAL cloud treatments for all of the selected stations is given by Figure 30 and between CAL and CAL surrogate cloud treatment by Figure 31. The points are coloured by the Intensity Weighted Cloud Fraction (IWCF), calculated by the surrogate cloud algorithm. It should be noted that a TROPOMI pixel-by-pixel comparison is conducted, for all pixels within 20 km from the overpass location, not only for the pixel over the site. Data from the entire dataset provided by DLR are included and no seasonal separation is performed at this stage. While it is unavoidable that less collocations are found for the autumn and winter months, due to generally more frequent high cloud coverage conditions, the seasonal comparisons [not shown here] lead to similar conclusions.

Since the AMF products do not depend on each other, an orthogonal distance regression (ODR) has been used instead of an ordinary linear regression (OLR) for the comparison. The differences in the regression slopes and offsets arising in the OLR when comparing independent variables, as well as the appropriateness of ODR, are in detail discussed in Cantrell [2008]. The ODR results are also sensitive to the errors of the two variables. Hence, in this case, the uncertainties of all approaches are assumed to be the same and equal to the AMF error that is provided by DLR. The parameters of the regression, i.e., slope (S), offset (O), and Pearson's correlation coefficient (R), are presented in each subplot.

Overall, CAL-to-CRB (Figure 30) and CAL-to-CAL surrogate (Figure 31) AMFs agree to a great extent for all sites, with correlation coefficients ranging from 0.95 to 0.98 and slopes between 0.99 and 1.08. The agreement is better for the clear-sky satellite pixels (blue colors), where no significant scatter is found and the data are very close to the 1:1 line. As expected, larger discrepancies between the two AMF products are found for higher IWCF fraction values, when the differences of the three cloud model approaches start having an effect.

Similarly to the above discussion, Figures 32 and 33 show the comparison of the tropospheric NO_2 VCDs that are retrieved using all three cloud models. The three products are in excellent agreement with slopes and correlation coefficients close to unity for all of the selected sites, i.e., under low cloud presence conditions, CRB, CAL and CAL surrogate report very similar results. The differences that the CAL surrogate cloud treatment are introducing are most evident for the high IWCF values (red colours) to be examined further with the comparisons of TROPOMI CRB, CAL and CAL surrogate model NO_2 VCDs against the reference ground-based MAX-DOAS being presented in Sect. 4.2.3.

4.2.3 Validation against the MAX-DOAS observations

Following the criteria that are described in Sect. 4.2.1, in total 2619 satellite and ground-based collocated measurements are found for the period of study (1544 with cloud fractions <20% and 1075 with 20% $\leq$ cloud fractions < 50%). Figure 34 shows scatter plots of the TROPOMI and the MAX-DOAS tropospheric NO_2 VCDs for the selected sites, using ROCINN CAL, surrogate CAL and CRB cloud models, for cloud fraction values < 20%. Each sub-panel corresponds to a different site. For Mainz, the collocations for all four operating MAX-DOAS instruments are combined together. In Uccle, very few collocations were found due to missing MAX-DOAS data for the selected days since the instrument had been installed on a different location in this time period. The different colors (blue, red and green) represent the three cloud model approaches (CRB, CAL and CAL surrogate, respectively). In this section, even though the satellite and ground-based NO_2 VCDs are independently retrieved, an ordinary linear regression is applied for the comparison since the MAX-DOAS NO_2 column is considered to be more representative of the "true" state. The slopes and offsets of the linear regression for each station, as well as statistical information on the Pearson's correlation coefficient are displayed in each sub-panel.

Figure 35 shows the consolidated TROPOMI validation, i.e., by including the collocations of all stations. Here, the analysis is performed for both low (< 20%) and high (> 20%) cloud fraction values in order to assess the performance of CRB, CAL and CAL surrogate under different cloud coverage conditions.

Overall, in all cases, no significant differences are found among the NO_2 VCDs using ROCINN CAL, CAL surrogate and CRB cloud treatments. Especially for low cloud presence conditions, the three cloud

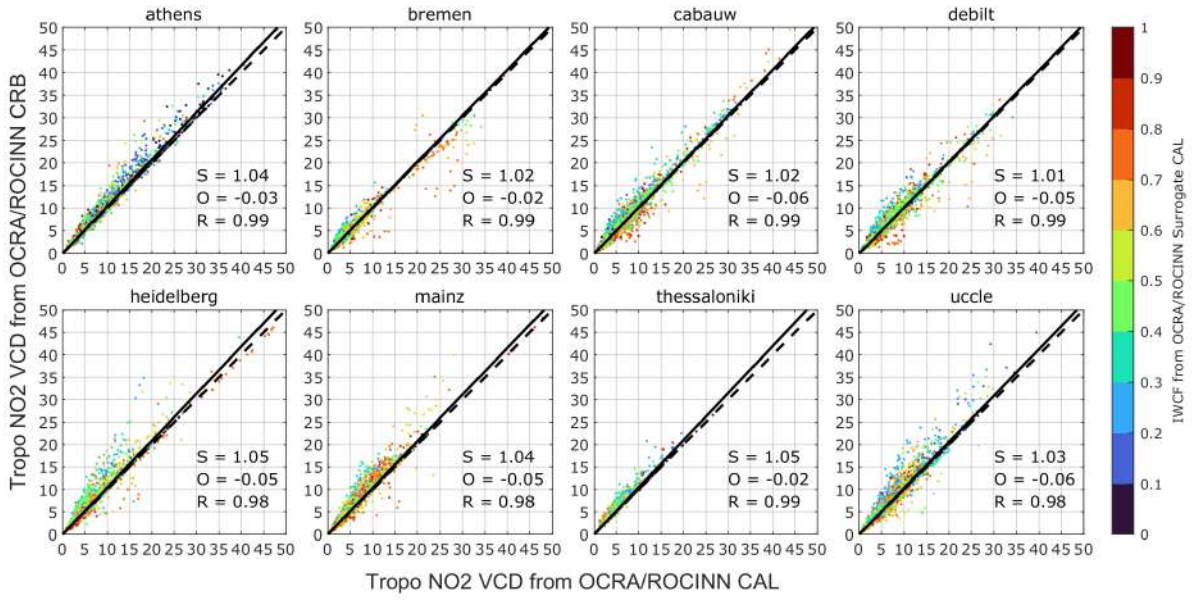

Figure 32: Scatter plots of the tropospheric NO_2 VCDs using CAL and CRB cloud treatments for all stations.

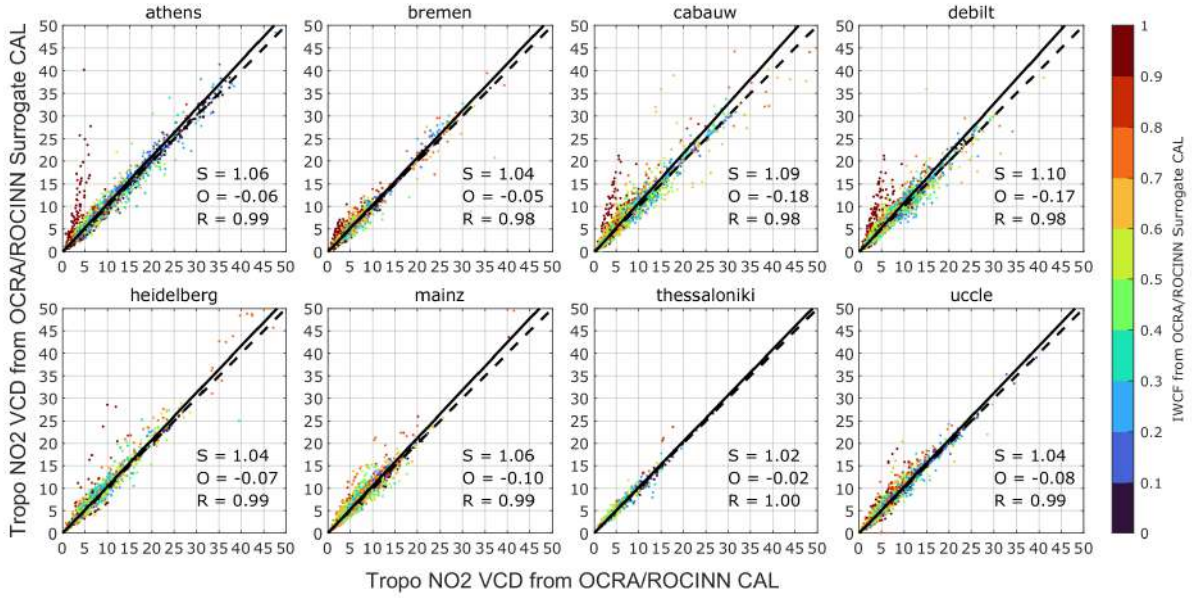

Figure 33: Scatter plots of the tropospheric NO_2 VCDs using CAL and CAL surrogate cloud treatments for all stations.

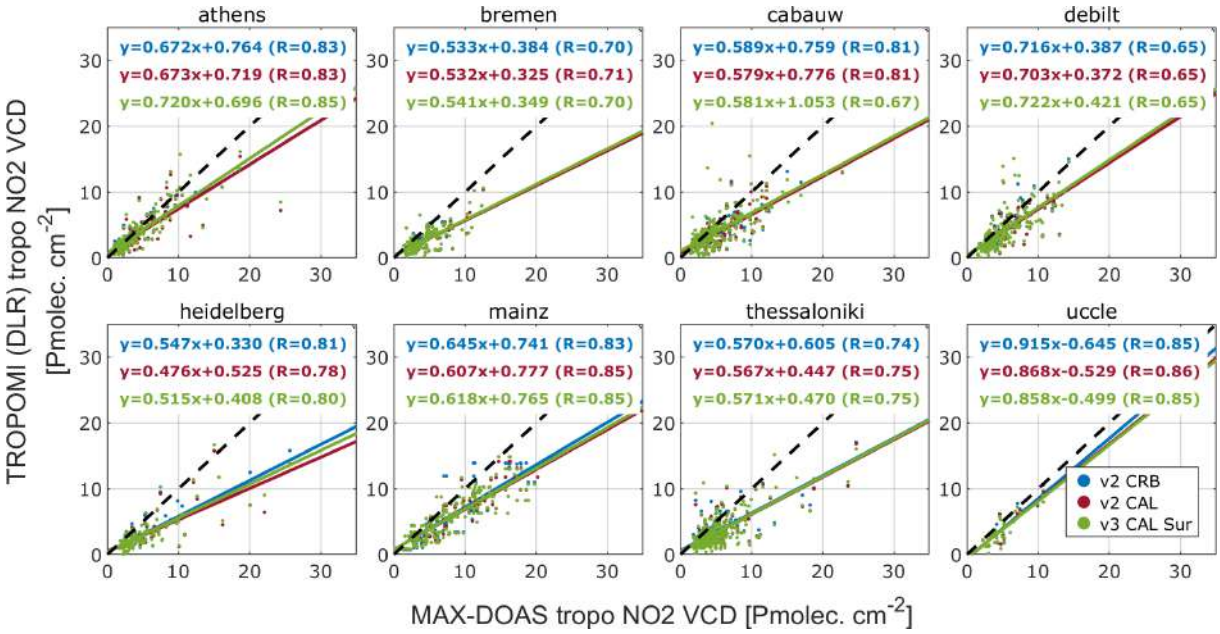

Figure 34: Comparison of the TROPOMI CRB (blue), CAL (red) and CAL surrogate model (green) tropospheric NO_2 VCDs and the ground-based MAX-DOAS for all stations. The data are filtered by cloud fraction $< 20\%$.

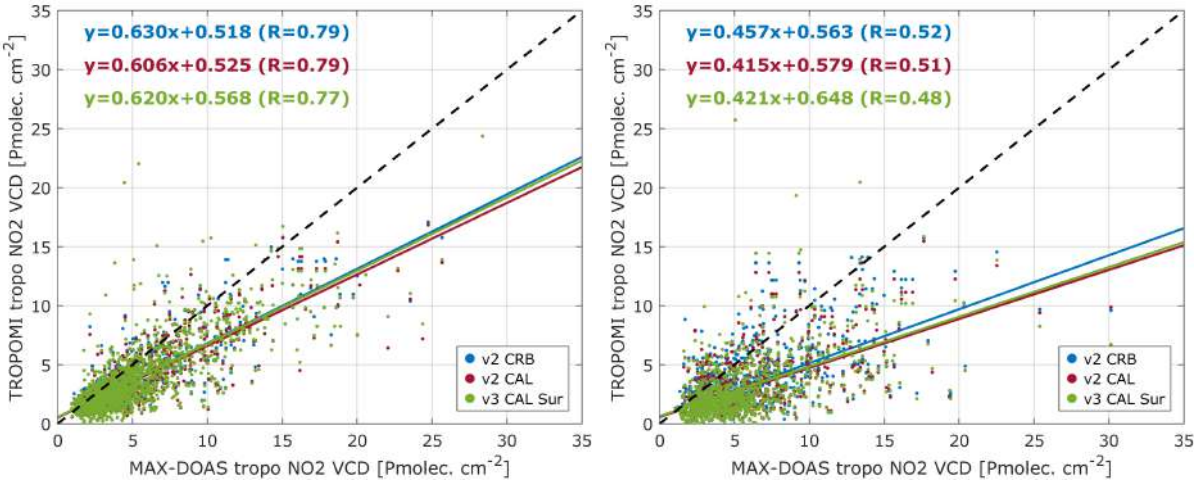

Figure 35: Consolidated comparison of TROPOMI and MAX-DOAS tropospheric NO_2 VCDs. The data are filtered by cloud fraction $< 20\%$ (left) and $> 20\%$ (right).

models show very similar comparison results with the MAX-DOAS with correlation coefficients $R = 0.77$-$R = 0.79$ and slopes ranging between 0.52 and 0.56.

For cloud fractions > 20% TROPOMI and the MAX-DOAS are expected to produce poorer comparison results than for the less cloudy conditions, yet the results are still in reasonable agreement. Even though the correlation coefficient for CAL retrievals is slightly higher than for CRB ($R = 0.70$ and $R = 0.66$, respectively), their performance is also very similar. This can also be seen in Tables 4 and 5, where the parameters of the linear regression between TROPOMI CRB, CAL and CAL surrogate and the MAX-DOAS, i.e., the slope and offset (in units of $\times 10^{15}$ molecules cm^{-2}, as well as the Pearson's correlation coefficient (R) are summarized for all stations, for both low and high cloud coverage conditions. However, in this case, it should be noted that the MAX-DOAS observations can also be affected by clouds and depending on the cloud conditions, the strength of the effect on the NO_2 VCDs may be different [e.g. Wang et al., 2017], which makes the comparison more challenging. Hence, test cases, where the cloud structure is well known, have been identified and have been further investigated for a more detailed assessment of the TROPOMI tropospheric NO_2 product, see section 4.3.

Table 4: Summary of the comparison between TROPOMI and the MAX-DOAS (cloud fraction < 20%).

Station	**Slope**			**Offset**			**R**		
	CRB	CAL	CAL_sur	CRB	CAL	CAL_sur	CRB	CAL	CAL_sur
Athens	0.672	0.673	0.720	0.764	0.719	0.696	0.83	0.83	0.85
Bremen	0.533	0.532	0.541	0.384	0.325	0.349	0.70	0.71	0.70
Cabauw	0.589	0.579	0.581	0.759	0.776	1.053	0.81	0.81	0.67
De Bilt	0.716	0.703	0.722	0.387	0.372	0.421	0.65	0.65	0.65
Heidelberg	0.547	0.476	0.515	0.330	0.525	0.408	0.81	0.78	0.80
Mainz	0.645	0.607	0.618	0.741	0.777	0.765	0.83	0.85	0.85
Thessaloniki	0.570	0.567	0.571	0.605	0.447	0.470	0.74	0.75	0.75
Uccle	0.915	0.868	0.858	-0.645	-0.529	-0.499	0.85	0.86	0.85

Table 5: Summary of the comparison between TROPOMI and the MAX-DOAS (cloud fraction > 20%).

Station	**Slope**			**Offset**			**R**		
	CRB	CAL	CAL_sur	CRB	CAL	CAL_sur	CRB	CAL	CAL_sur
Athens	0.496	0.481	0.489	1.182	0.956	1.253	0.67	0.71	0.51
Bremen	0.482	0.451	0.468	0.230	0.210	0.184	0.62	0.63	0.63
Cabauw	0.352	0.337	0.375	0.540	0.597	0.498	0.50	0.51	0.49
De Bilt	0.666	0.639	0.699	-0.043	-0.157	-0.378	0.44	0.43	0.44
Heidelberg	0.407	0.364	0.362	0.373	0.419	0.469	0.65	0.66	0.56
Mainz	0.454	0.379	0.366	0.822	1.074	1.242	0.57	0.54	0.51
Thessaloniki	0.326	0.284	0.267	1.088	0.941	1.013	0.38	0.38	0.38
Uccle	0.256	0.215	0.225	0.937	0.980	0.951	0.26	0.22	0.22

Figure 36 shows an overview of the daily differences between TROPOMI and the MAX-DOAS NO_2 columns for low cloud coverage conditions (cloud fraction < 20%) for each station. In all cases, a

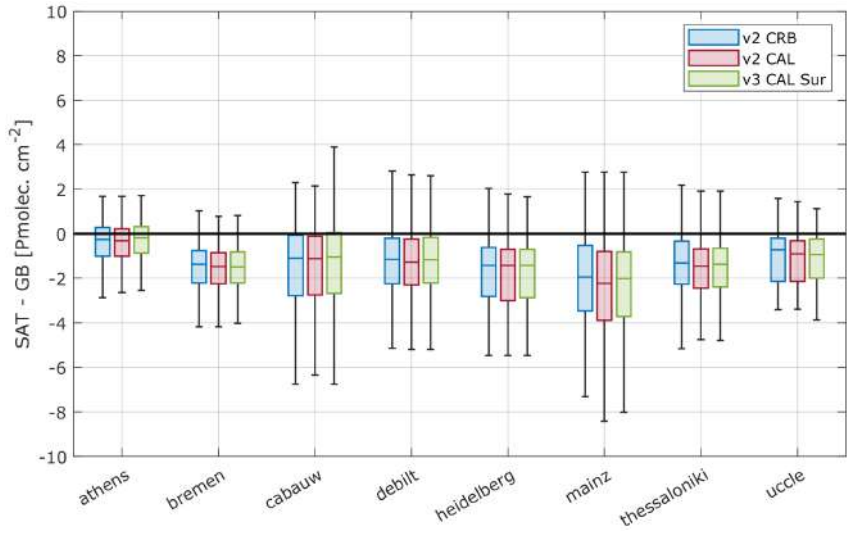

Figure 36: Box-and-whisker plots summarizing the bias and spread of the differences between TROPOMI (SAT) and MAX-DOAS (GB) tropospheric NO_2 VCDs (cloud fraction< 20%) for all sites.

clear negative bias is found with median differences ranging from approximately -0.5 to -2×10^{15} molecules/cm^2 for all cloud model retrievals. The observed negative bias could partly be attributed to the larger satellite footprint, resulting in a smoother perception of the NO_2 concentrations, while the MAX-DOAS measurements are affected more by local emissions. The consolidated median differences for cloud fractions < 20% are -1.14×10^{15} molecules/cm^2 (which corresponds to a mean fractional bias of -35.05%) for CRB, -1.24×10^{15} molecules/cm^2 (-37.18%) for CAL, and -1.18×10^{15} molecules/cm^2 (-35.03%) for CAL surrogate. The corresponding median differences for cloud fractions > 20% are -2.22×10^{15} molecules/cm^2 (-68.80%), -2.36×10^{15} molecules/cm^2 (-73.03%) and -2.34×10^{15} molecules/cm^2 (-72.24%) for CRB, CAL and CAL surrogate, respectively.

Even though TROPOMI has the highest spatial resolution among all space-borne instruments (3.5×5.5 km^2 since 6 August 2019), underestimation of the TROPOMI tropospheric NO_2 columns has also been found in multiple validation studies using data from MAX-DOAS instruments [e.g. Chan et al., 2020, Dimitropoulou et al., 2020, Verhoelst et al., 2021, Karagkiozidis et al., 2023]. According to the latest issue of the quarterly Routine Operations Consolidated Validation Report, [7] for the operational S5P/TROPOMI tropospheric NO_2 product, a median bias of -1.3×10^{15} molecules/cm^2 (about -27.8%) was found over the full satellite mission using MAX-DOAS data from 31 stations that belong to the Network for Detection of Atmospheric Composition Change, NDACC [8].

4.3 Validation based on the S5P/TROPOMI observations for specific cloud shadow scenes

Relatively large solar zenith angles and polluted type NO_2 profiles are conditions for which cloud shadow effects in the NO_2 TVDC are maximized [Yu et al., 2022]. Thus, for a region roughly covering central Europe, two months (March and April 2021) of VIIRS cloud shadow data was downloaded from CLASS. For these months the solar zenith angle is favorable for making cloud shadows visible from above. For this data set the number of VIIRS pixels with a cloud shadow within a circle of 15 km radius was calculated

[7] https://s5p-mpc-vdaf.aeronomie.be/ProjectDir/reports//pdf/S5P-MPC-IASB-ROCVR-22.01.00_20240503_signed.pdf

[8] https://ndacc.larc.nasa.gov

for the MAX-DOAS stations listed in Table 1. In Fig. 37 this number is shown for March (upper plot) and April (lower plot) 2021. Some dates stand out where one or more stations may be affected by cloud

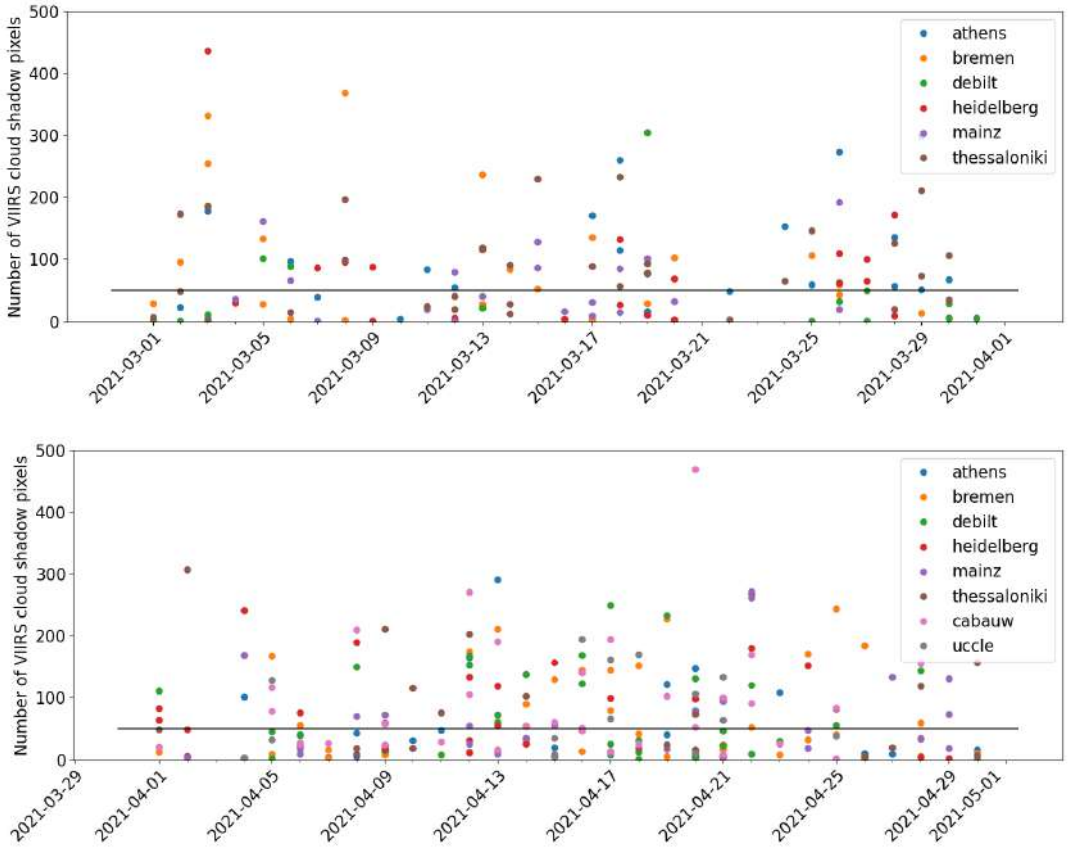

Figure 37: The number of VIIRS pixels with a cloud shadow within a circle of 15 km radius centered on the MAX-DOAS station. The black line is at 50 pixels. The upper plot is for March 2021 and the lower plot for April 2021.

shadows: 3 March (Bremen and Heidelberg stations) and 20 April (Cabauw station) 2021. For these two dates detailed cloud shadow effect analyis was done, as presented below. In addition a cloud free case on 24 February 2021 was used to visualize how non-cloud effects affect the NO_2 TVDC. We start by looking at the cloudless case.

Note that below all DLR data were required to have NO2TropCorrection Flag = 1 as above and all operational data a QA-value > 0.95.

4.3.1 Cloudless sky: 2021.02.24

For this date the sky was cloudless for all stations. However, coincident TROPOMI and MAX-DOAS measurements are not available for Cabauw and Uccle. RGB plots for the stations in Athens, Bremen, DeBilt, Heidelberg, Mainz, and Thessaloniki are shown in Fig. 38 and Figs.43-47. Differences between the standard DLR (CAL) and the DLR surrogate 3D cloud NO_2 TVCD are small. There are some pixels where the surrogate 3D cloud NO_2 TVCD is small by about 1 Pmol/cm^2 for DeBilt, Fig. 44. It is noted that two pixels for the DLR product have negative NO_2 TVCD (grey pixels in lower row centre plot in Fig. 38) although the quality flag NO2TropCorrection Flag = 1.

In Table 6 a comparison is presented between the MAX-DOAS NO_2 columns and NO_2 TVCDs derived

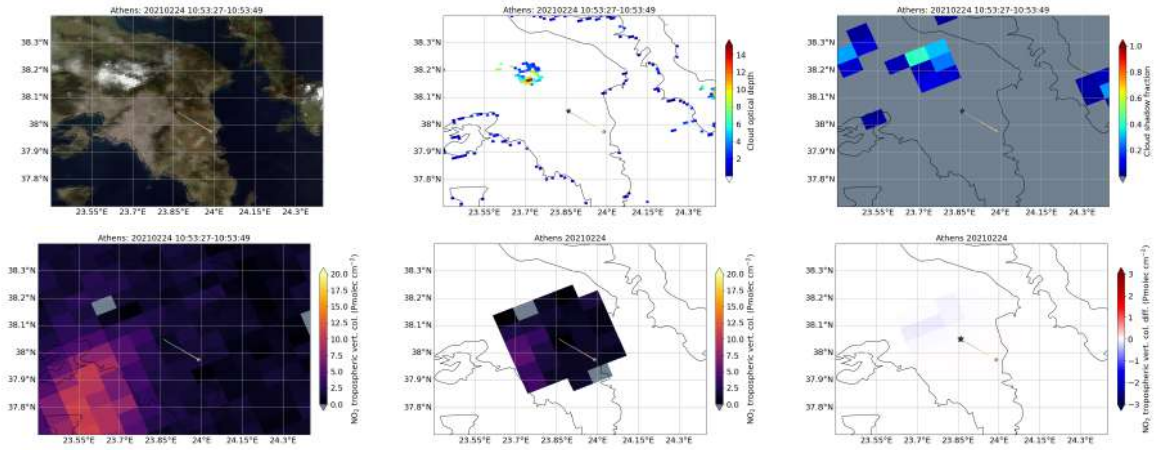

Figure 38: First row: (left) RGB from VIIRS channel M03, M04 and M05. (middle) VIIRS cloud optical depth. (right) Cloud shadow fraction calculated from VIIRS cloud shadow mask. Second row: (left) Operational NO_2 TVCD. (middle) DLR surrogate 3D cloud NO_2 TVCD (CRB). (right) Standard DLR (CAL) minus DLR surrogate 3D cloud NO_2 TVCD. The black star indicates the location of the MAX-DOAS site. The grey star suggests the MAX-DOAS sensing distance. The colored line connecting the two stars represents the MAX-DOAS sensing range and the different line colors is the line segment traversed for each S5P pixel. For 24 February 2021 and Athens.

from TROPOMI measurements by the operational and the DLR algorithms. The S5P NO_2 TVCD columns are calculated as the weighted average of the S5P NO_2 TVCD in the viewing direction of the MAX-DOAS. The weight is taken to be the length traversed for each S5P pixels relative to the total length traversed, see Fig. 38 and Figs.43-47 for examples of lines and line segments. For the Mainz site the MAX-DOAS varies between 10.80 to 14.85 Pmol cm^{-2} depending on viewing direction. This nearly 40% difference indicate large horizontal variability in the NO_2 column. The various S5P NO_2 TVCDs show horizontal variability of similar magnitudes, however their minimum value is in the direction where the MAX-DOAS has its maximum (Φ=231.0°). The S5P overpass time is within 2-13 minutes for all MAX-DOAS measurements.

For all sites the MAX-DOAS values are systematically larger than the TROPOMI derived values. The precision of the various S5P NO_2 products (typically between 30-50%) is larger than MAX-DOAS uncertainty (typically smaller than 7%). The differences between the various NO_2 TVCDs are well within the uncertainties for these quantities.

4.3.2 Cloud shadow case: 2021.03.03

For 3 March 2021 partly cloud cover was present for several of the MAX-DOAS stations in Table 1. Heidelberg is in a cloud shadow, Fig. 39. For Bremen cloud shadows are readily visible in the RGB plot, Fig. 48, while DeBilt lies on the edge of a larger cloud field, Fig. 49. Mainz is cloud free, Fig. 50, but is included in the analysis in order to investigate the azimuth variations in the NO_2 TVCD. For Athens and Thessaloniki the sky is cloudfree and no near concurrent MAX-DOAS measurements are available for Uccle and Caubauw. These four locations are thus not further discussed for 3 March 2021.

For Heidelberg the MAX-DOAS is under the cloud shadow and the MAX-DOAS views to the north under the cloud shadow, upper right plot Fig. 39. Note that the black areas to the east and west north of the cloud band in the RGB (upper left plot Fig. 39) are not cloud shadows, but forest areas. The cloud shadow is visible in the RGB as a slightly dimmer band north of the cloud. Interestingly, there is an east-west NO_2 TVCD gradient, with low values to the east and larger to the west of the MAX-DOAS location, bottom left plot Fig. 39.

Table 6: The S5P and MAX-DOAS NO_2 columns for MAX-DOAS stations from Table 1 for 24 February 2021. NO_2^{oper}, NO_2^{DLR}, and NO_2^{surr} are the NO_2 TVCD derived from TROPOMI measurements using the operational, standard DLR and surrogate 3D DLR retrievals, respectively. The S5P NO_2 TVCD columns are calculated as the weighted average of the S5P NO_2 TVCD in the viewing (azimuth=Φ) direction of the DOAS. The weight is the length traversed for each pixels relative to the total length traversed, see Fig. 38 and Figs.43-47 for examples of lines and line segments. NO_2^{DOAS} is the NO_2 column from from the MAX-DOAS measurements.

Instrument name	S5P time (hh:mm:ss)	DOAS time (hh:mm:ss)	DOAS ($\Phi°$)	NO_2^{oper} (Pmol/cm^2)	NO_2^{DLR} (Pmol/cm^2)	NO_2^{surr} (Pmol/cm^2)	NO_2^{DOAS} (Pmol/cm^2)
iup008	10:53:38	10:52:39	120.0	1.568	0.972	0.972	2.083
iup002	12:38:33	14:13:50	180.0	4.872	3.906	3.877	8.899
knmi004	12:38:23	12:41:55	80.0	5.369	4.018	4.149	10.396
uheidelberg001	12:37:34	12:34:22	324.0	4.025	2.892	2.867	8.091
mpic001	12:37:44	12:35:25	321.0	6.010	5.803	5.710	13.610
mpic002	12:37:44	12:35:25	51.0	7.866	9.119	8.937	12.487
mpic003	12:37:41	12:35:25	141.0	6.957	7.516	7.437	10.801
mpic004	12:37:42	12:24:30	231.0	5.441	4.963	5.010	14.850
lap007	10:54:22	10:51:57	255.0	4.676	4.378	4.378	7.166
lap008	10:54:22	10:57:45	142.0	3.768	3.292	3.292	5.446

Further details in the cloud shadow band is provided in Fig. 40. In the upper left plot of Fig. 40 is shown how the S5P operational NO_2 TVCD varies with latitude. Each line represents the NO_2 TVCD along S5P rows with the star marked line being closest to the MAX-DOAS viewing direction and the green (purple) triangle marked line is the first along track S5P row to the west (east). Furthermore, unmarked lines represents data to the west of the star marked line while circled marked lines are to the east. The cloud shadow fraction for the same data points are shown in the lower left plot of Fig. 40. In the upper right plot is shown the cloud shadow fraction versus the NO_2 TVCD. For the higher NO_2 TVCD values to the west of the MAX-DOAS location, the NO_2 TVCD decrease with increasing cloud shadow fraction, linear red line fit in the upper right plot of Fig. 40. This is in agreement with the behaviour of the underestimate predicted by theory [Yu et al., 2022]. For the lower NO_2 TVCD values to the east a smaller change with cloud shadow fraction is seen, purple line. MAX-DOAS NO_2 profiles are shown in the bottom right plot of Fig. 40. Most of the NO_2 is close to the surface with some enhancements seen around 1.5 km altitude for some profiles.

The bottom right plot in Fig. 39 shows the DLR surrogate 3D cloud NO_2 TVCD minus the standard DLR NO_2 TVCD. The DLR surrogate 3D cloud retrieval gives larger NO_2 TVCD in the cloud shadow and appears to correct for the cloud shadow impact. To see if this is so also for other locations, Fig. 41 shows the DLR surrogate 3D cloud NO_2 TVCD minus the standard DLR NO_2 TVCD plotted versus the cloud shadow fraction for the Heidelberg, Bremen, Cabauw, DeBilt and Mainz locations. Also shown are shown linear fits for the cloud shadow fractions present in the VIIRS data for this day and location. These fits are for data where the cloud shadow fraction is larger than zero. For the Bremen, DeBilt and Heidelberg locations the surrogate 3D cloud retrieval gives larger NO_2 TVCD than the standard retrieval. For Cabauw the behaviour is opposite. From the RGB plots in Fig. 39 and Figs. 48-49 it may be noted that the cloud situation for Cabauw differs from that over Bremen, DeBilt and Heidelberg and that may be the reason for the different behaviour.

Table 4.3.2 compares the MAX-DOAS NO_2 columns and NO_2 TVCDs derived from TROPOMI measurements by the operational and the DLR algorithms. For this day Mainz is cloud free. As opposed to the cloud free data for 24 February 2021, Table 6, for 3 March 2021 the S5P data shows a similar spatial distribution as the MAX-DOAS. The S5P overpass is within 4-28 min of the MAX-DOAS measurements.

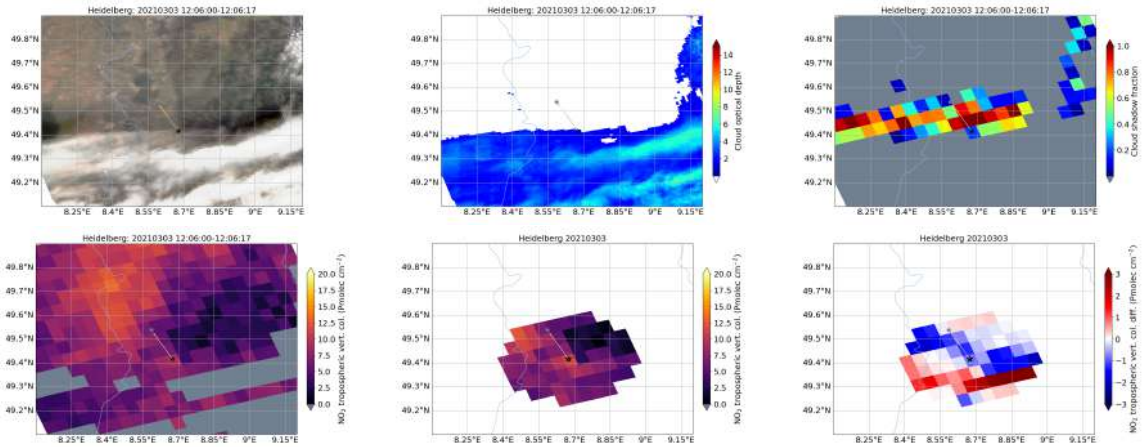

Figure 39: Similar to Fig 38 but for Heidelberg and 3 March 2021.

Table 7: Similar to Table 6 but for 3 March 2021.

Instrument name	S5P time (hh:mm:ss)	DOAS time (hh:mm:ss)	DOAS (Φ°)	NO_2^{oper} (Pmol/cm^2)	NO_2^{DLR} (Pmol/cm^2)	NO_2^{surr} (Pmol/cm^2)	NO_2^{DOAS} (Pmol/cm^2)
iup002	12:07:07	12:35:54	295.0	10.458	8.786	8.867	26.607
knmi004	12:07:03	12:47:32	80.0	10.827	11.857	10.584	11.575
uheidelberg001	12:06:09	12:04:19	324.0	6.740	6.568	7.505	13.009
mpic001	12:06:20	12:13:23	321.0	10.727	10.177	10.211	14.185
mpic002	12:06:19	12:02:43	51.0	12.472	13.430	13.090	19.045
mpic003	12:06:18	12:13:23	141.0	9.570	9.477	9.805	14.392
mpic004	12:06:18	12:34:41	231.0	7.777	7.320	7.436	14.851

4.3.3 Cloud shadow case: 2021.04.20

For 20 April 2021 scattered clouds were present around Cabauw (Fig. 42), DeBilt (Fig. 53), Heidelberg (Fig. 54) and Mainz (Fig. 55). Cloudfree conditions prevailed for Athens (Fig. 51), Bremen (Fig. 52) and Thessaloniki (Fig. 56). As for the other cases presented in sections 4.3.1 and 4.3.2, the MAX-DOAS NO_2 columns are for the most part larger than the S5P retrieved TVCDs, see Table 4.3.3. However, the MAX-DOAS NO_2 column is smaller for Bremen which is under a cloud free sky.

Cabauw has scattered clouds in the surroundings, Fig. 42. The S5P overpass is about 23 min before the MAX-DOAS measurements. Thus the cloud situation may have changed between the two measurements. Nevertheless, the DLR surrogate method (11.840 Pmol/cm^2) gives better agreement with MAX-DOAS measurement (10.484 Pmol/cm^2) then standard DLR method (7.432 Pmol/cm^2), see Table 4.3.3.

In the right plot of Fig. 41 is the DLR surrogate 3D cloud NO_2 TVCD minus the standard DLR NO_2 TVCD plotted versus the cloud shadow fraction for the Athens, Bremen, Cabauw, DeBilt, Heidelberg, and Mainz locations. For Cabauw the DLR surrogate retrieval increase the NO_2 TVCD compared with DLR standard method for cloud shadow fractions above 0.6. For DeBilt and Heidelberg the differences decrease with increasing cloud shadow fraction as opposed to findings for 3 March 2021, section 4.3.2. Note that linear fits are only shown if the data for a station include cloud shadow fractions above 0.5. Hence, no linear fit is shown for Mainz.

Due to S5P pixels not being analysed due to cloud there are no DLR S5P data for the north/northwest pointing MAX-DOAS for Mainz, Table 4.3.3. As for 24 February 2021, Table 6 the S5P and MAX-DOAS maxima are in different directions. The S5P overpass is within 1-30 min of the MAX-DOAS

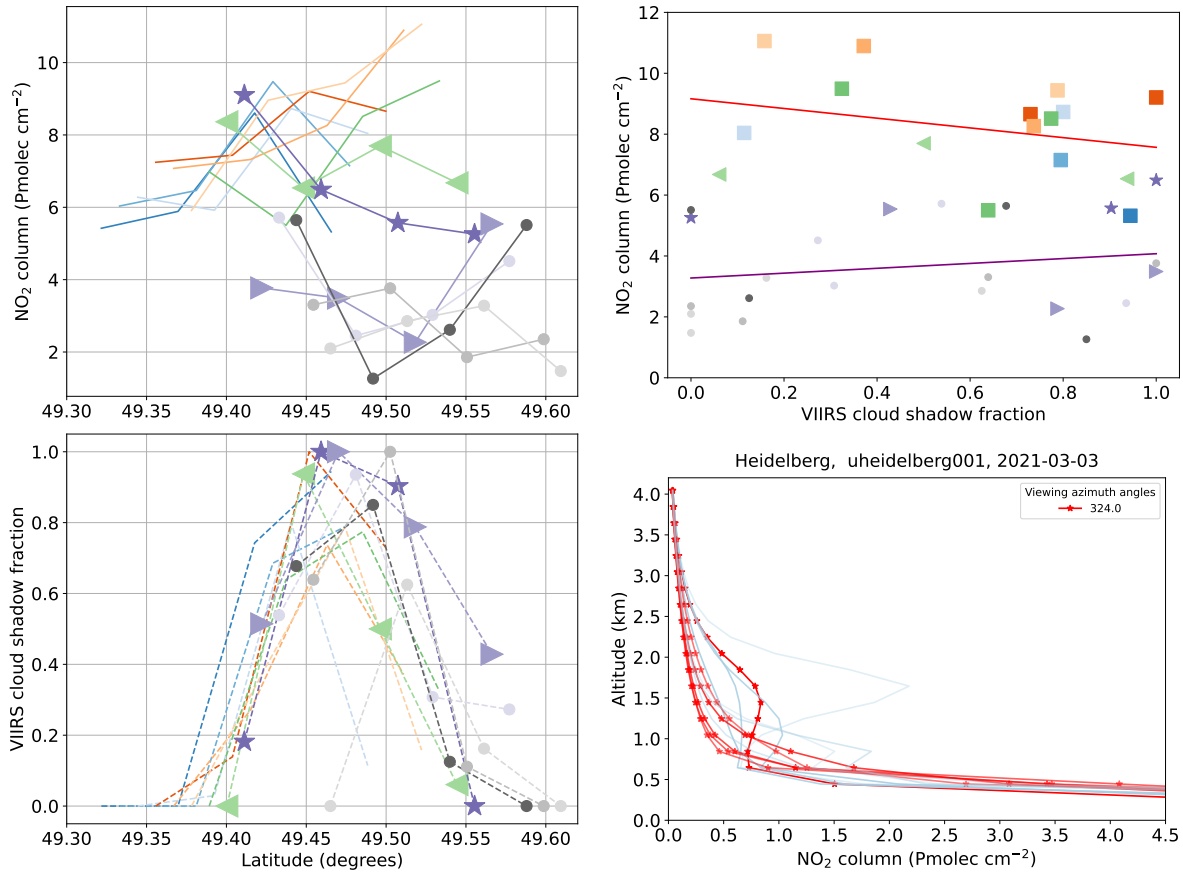

Figure 40: Along track S5P operational NO_2 TVCD (upper left) and cloud shadow fraction (lower left) as a function of latitude. The various lines are colored and marked with respect to their east-west position relative to the MAX-DOAS viewing direction. The star marked line is the S5P closest to the MAX-DOAS viewing direction. The green (purple) triangle marked line is the first along track S5P row to the west (east). Otherwise unmarked lines are to the west of the star marked line while circled marked lines are to the east. In the upper right plot is shown the cloud shadow fraction versus the NO_2 TVCD. The red (purple) line is a linear fit to the data to the west (east) of the MAX-DOAS viewing direction. In the bottom right plot is shown MAX-DOAS NO_2 profiles. Profiles measured within 30 minutes of the S5P overpass are colored red.

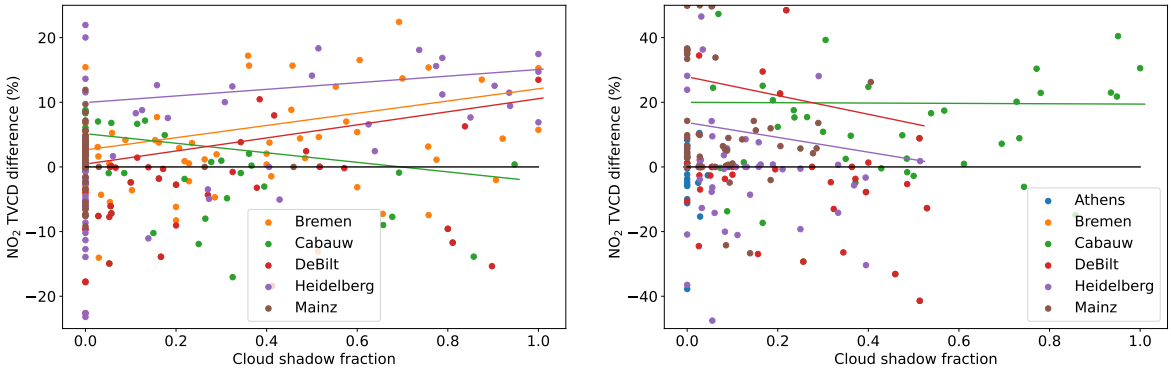

Figure 41: The cloud shadow fraction versus the percent difference of NO_2^{surr}-NO_2^{DLR} for various MAX-DOAS locations given in the legend. The solid lines are linear fits to the data for each location. The black line is the zero line. Left plot is for 3 March 2021 and right plot for 20 April 2021. Note different scales on the y-axes.

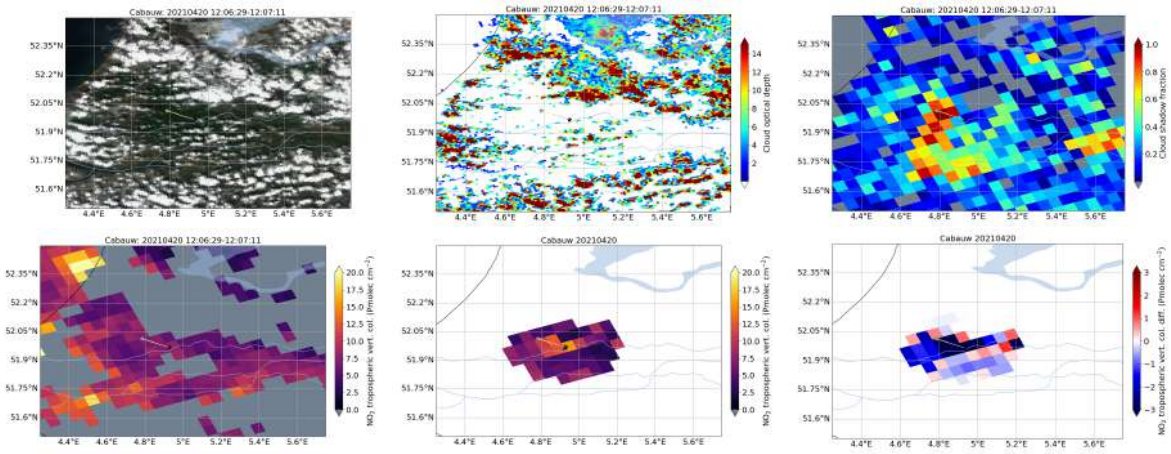

Figure 42: Similar to Fig 38 but for Cabauw. For 20 April 2021.

measurements.

4.3.4 Discussion of cloud shadow cases

The above cases were used to investigate 1): possible cloud shadow effects in S5P retrievals; and 2) how the DLR surrogate method behave in the presence of cloud shadows. When discussing the above cases the following should be kept in mind:

- The cloud shadow fraction calculations include 1) unknown uncertainties in the VIIRS cloud shadow product; and 2) differences in overpass times between S5P and VIIRS. This may cause differences on the order of the magnitude of a S5P pixel in co-locations when clouds move with the wind.
- When comparing MAX-DOAS and S5P retrievals there may be differences in NO_2 columns due to differences in overpass times of the S5P and the MAX-DOAS measurements.
- The cloud shadow effect is largest for polluted scenes. It has been difficult to identify cases with large S5P NO_2 TVCD and cloud shadows.

Table 8: Similar to Table 6 but for 20 April 2021. N/A indicates that no satellite data where available for one or more of the pixels in the MAX-DOAS viewing direction.

Instrument name	S5P time (hh:mm:ss)	DOAS time (hh:mm:ss)	DOAS (Φ°)	NO_2^{oper} (Pmol/cm^2)	NO_2^{DLR} (Pmol/cm^2)	NO_2^{surr} (Pmol/cm^2)	NO_2^{DOAS} (Pmol/cm^2)
iup008	12:02:18	12:00:14	275.0	3.536	3.690	3.435	5.935
iup002	12:06:55	11:34:15	270.0	5.410	5.714	5.714	4.703
knmi006	12:06:51	11:29:39	287.0	6.962	7.432	11.840	10.484
knmi004	12:06:51	10:12:02	80.0	5.439	N/A	N/A	4.946
uheidelberg001	12:05:57	10:14:19	324.0	11.002	N/A	N/A	15.509
mpic001	12:06:08	12:07:49	321.0	7.741	N/A	N/A	10.190
mpic002	12:06:08	12:07:49	51.0	6.720	7.670	11.088	8.605
mpic003	12:06:06	11:36:02	141.0	5.302	5.541	5.966	8.268
mpic004	12:06:07	11:36:02	231.0	5.324	5.561	5.940	10.801
lap007	12:03:01	12:46:08	220.0	2.180	3.035	3.028	5.412
lap008	12:03:02	11:56:43	142.0	2.363	3.136	3.182	5.859

For the 3 March 2021 case a cloud shadow effect is present for Heidelberg in the S5P NO_2 TVCD for pixels with increased NO_2 values. The DLR surrogate retrieval appears to correct for the cloud shadow effect for this case. For the other cloud shadow cases investigated the cloud shadow impact in S5P retrievals is less clear. The DLR surrogate retrieval is seen to change the S5P NO_2 TVCD in the vicinty of cloud shadows. However, the changes both increase and decrease the column compared to the standard DLR method. Finally note that the differences between surrogate and standard retrievals mostly are within the reported uncertainties.

5 Conclusions

Synthetic and observational data have been used to asses the effect on clouds TROPOMI NO_2 retrievals and how various cloud correction methods improve the retrievals. The synthetic data set includes 1D-layer clouds, box clouds and realistic 3D clouds. The observational data sets include TROPOMI, VIIRS and MAX-DOAS observations for the year 2021 and 2022 for selected MAX-DOAS stations in Europe. Both the synthetic and observational data are analysed by retrieval methods applying several different cloud correction methods. The findings are summarized below:

- **Synthetic data set conclusions.** The standard NO_2 retrieval with various cloud correction schemes was applied to a series of synthetic data. In a 1D layer cloud scene, the results exhibit generally good agreement, with the retrieval biases mostly staying within 20%. However, relatively large biases are observed in cases of high SZAs and when applying the OCRA/ROCINN CRB cloud correction in the NO_2 retrievals. For the latter cases, these biases can be significantly reduced by employing a fixed cloud albedo of 0.8 and a corresponding effective cloud fraction. In 2D box-cloud and 3D LES cloud scenes, the most significant 3D biases arise from cloud shadow effects. All cloud products used in the NO_2 retrieval typically underestimate cloud fraction retrieval for pixels affected by the cloud shadows, resulting in substantial positive biases in the calculation of NO_2 AMF.
- **S5P/TROPOMI Validation against MAX-DOAS observations.** Observations from 8 ground-based MAX-DOAS remote sensing instruments around Europe were used for validating the TROPOMI tropospheric NO_2 VCDs using OCRA/ROCINN CRB, CAL and CAL surrogate cloud models. The validation is performed for selected days in 2021 and 2022, under various pollution levels and cloud coverage conditions. While a clear underestimation by the TROPOMI tropospheric NO_2 columns is found for all stations, mainly due to the relatively larger satellite footprint, CRB, CAL and CAL surrogate cloud treatments lead to similar results by comparison with the MAX-DOAS, especially for less cloudy conditions. For cloud fractions $> 20\%$, even though slightly higher correlation coefficients are found for the CAL retrievals, the performance of CAL and CRB is overall very similar. However, in this case, the MAX-DOAS measurements can also be affected by clouds and thus, further analysis is required for a more detailed TROPOMI validation, by investigating cases where the cloud structure and the NO_2 field around the site are well known.
- **S5P/TROPOMI Validation over selected cloud shadow cases.** The effect of cloud shadows on the TROPOMI NO_2 retrievals have been made for selected cases where cloud shadows are present in the VIIRS data. There are very few cases with "ideal" cloud shadow bands. For one such case there is cloud shadow effect, i.e. that the NO_2 TVCD is smaller in the cloud shadow band, in agreement with theoretical predictions. For other cases including scattered clouds where cloud shadows are present, the NO_2 TVCDs are seen to both increase and decrease. It has mostly been shown that the cloud shadow effect is within the uncertainty of the satellite retrievals. The DLR surrogate cloud model retrieval changes NO_2 column in the presence of clouds compared to the standard CAL retrieval, however the reported changes is within the uncertainty of the two products.

6 Future suggestions

- The current cloud correction approach, using 1D radiative transfer modeling (RTM), is insufficient for adequately correcting 3D cloud effects in trace gas retrieval. A rapid and robust method to correct these effects in trace gas retrieval is needed. This could involve using 3D RTM, employing a machine learning approach, or adopting a more advanced cloud model in the cloud retrieval algorithm.
- There are consistent differences in TVCDs from MAX-DOAS and S5P. Fully 3D RTM simulations of MAX-DOAS and S5P measurements may be used together with standard retrievals to understand these differences. Such investigations should be done for both clear skies and cloudy skies.

- LES model results as used here are extremely useful, but also expensive in terms of computer resources required. EarthCARE will soon provide fully 3D input data for a number of real cloud conditions. These may be combined with future S4 measurements to further understand the impact of various cloud situations on NO_2 TVCD retrievals.

Acknowledgements

We warmly acknowledge the usage of EVDC ESA Validation Data Centre, http://evdc.esa.int/, ground-based MAX-DOAS tropospheric NO_2 data. We thank in particular the MAX-DOAS instruments PIs for allowing access to their data sets, namely Michel Van Roozendael (michel.vanroozendael@aeronomie.be), Andreas Richter (richter@iup.physik.uni-bremen.de), Thomas Wagner (thomas.wagner@mpic.de), Udo Frieß (udo.friess@iup.uni-heidelberg.de) and Ankie Piters (ankie.piters@knmi.nl). The MAX-DOAS NO_2 data used in this report have been processed by the FRM_4DOAS project (ESA contract no. 4000118181/16/I-EF), which is also gratefully acknowledged.

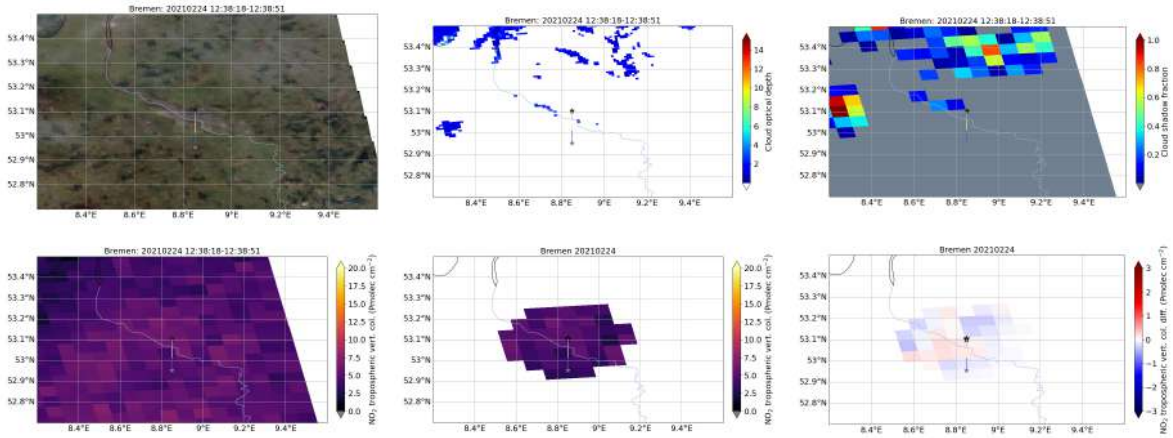

Figure 43: Similar to Fig 38 but for Bremen. For 24 February 2021.

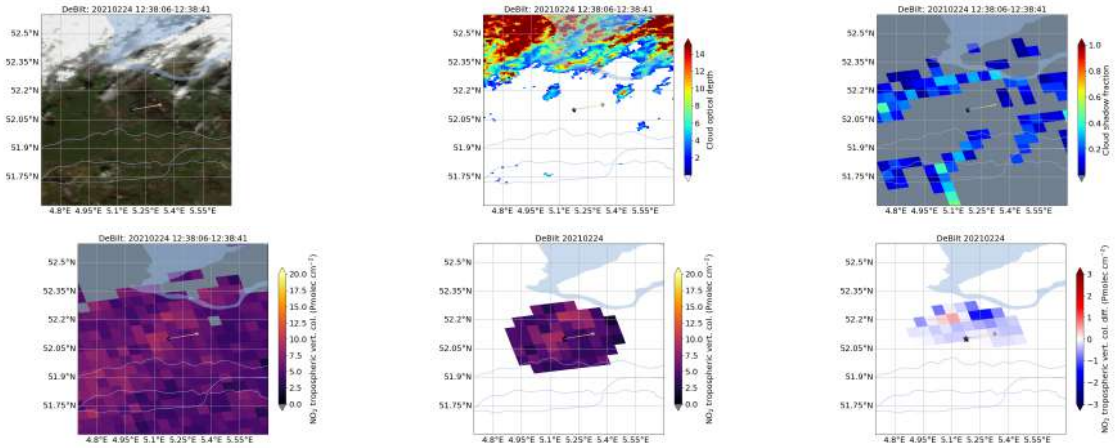

Figure 44: Similar to Fig 38 but for DeBilt. For 24 February 2021.

A Cloud shadow plots

A.1 Cloudless sky: 2021.02.24

Plots for Bremen are shown in Fig. 43.

Plots for DeBilt are shown in Fig. 44.

Plots for Heidelberg are shown in Fig. 45. Three pixels for the DLR product have negative NO_2 TVCD (grey pixels in Fig. 45) although the quality flag NO2TropCorrection Flag = 1.

Plots for Mainz are shown in Fig. 46. As for Athens and Heidelberg, also for Mainz there are (two) pixels for the DLR product that have negative NO_2 TVCD (grey pixels in Fig. 45) although the quality flag NO2TropCorrection Flag = 1.

Plots for Thessaloniki are shown in Fig. 47.

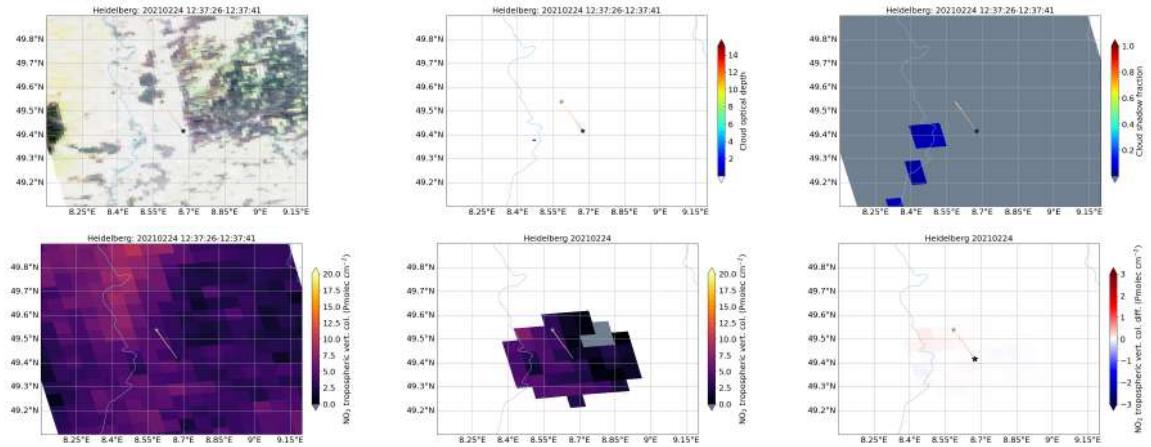

Figure 45: Similar to Fig 38 but for Heidelberg. For 24 February 2021.

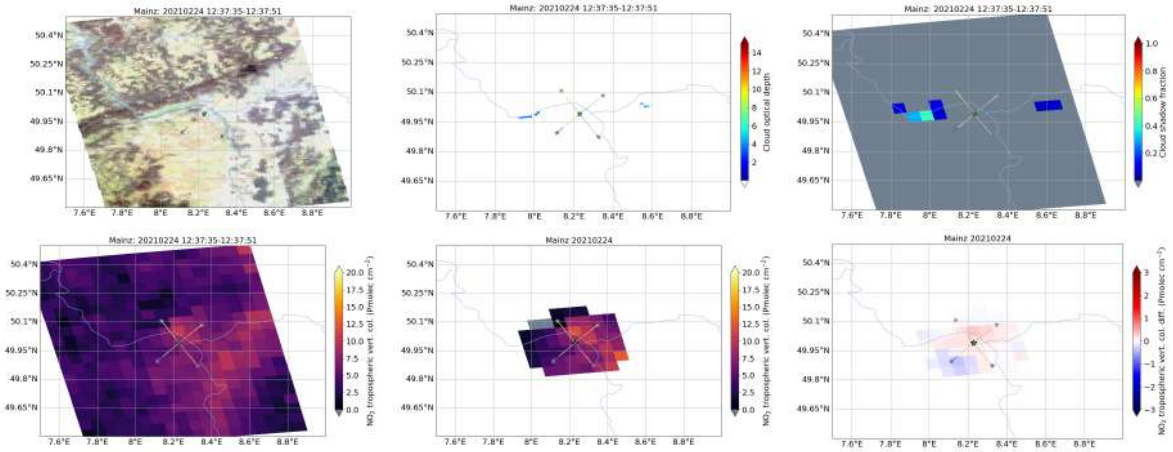

Figure 46: Similar to Fig 38 but for Mainz. For 24 February 2021.

A.2 Cloud shadow case: 2021.03.03

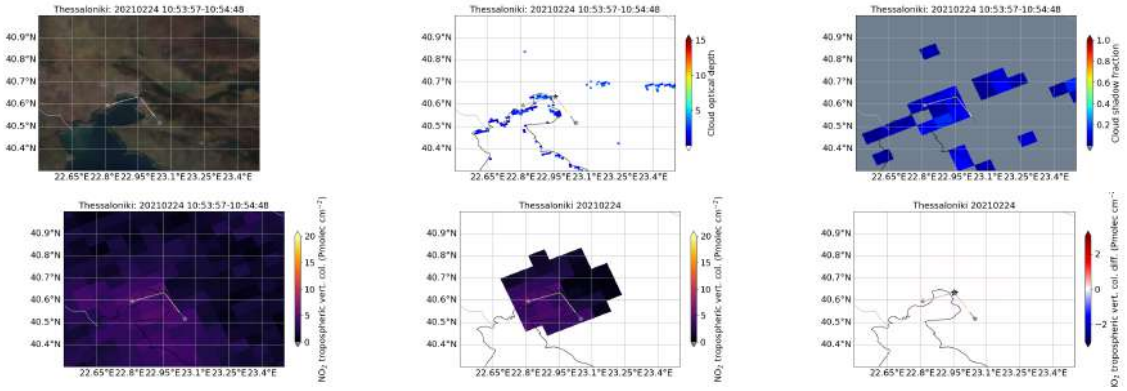

Figure 47: Similar to Fig 38 but for Thessaloniki. For 24 February 2021.

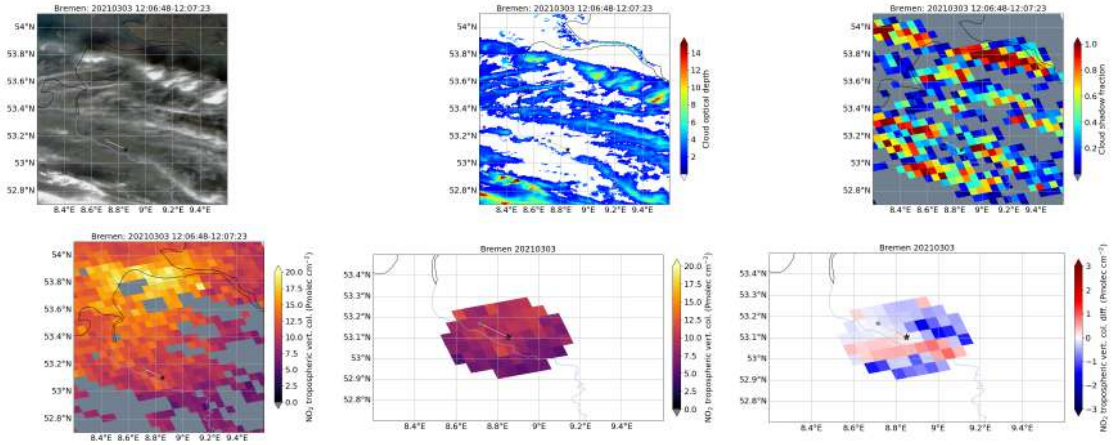

Figure 48: Similar to Fig 38 but for Bremen and 3 March 2021.

A.3 Cloud shadow case: 2021.04.20

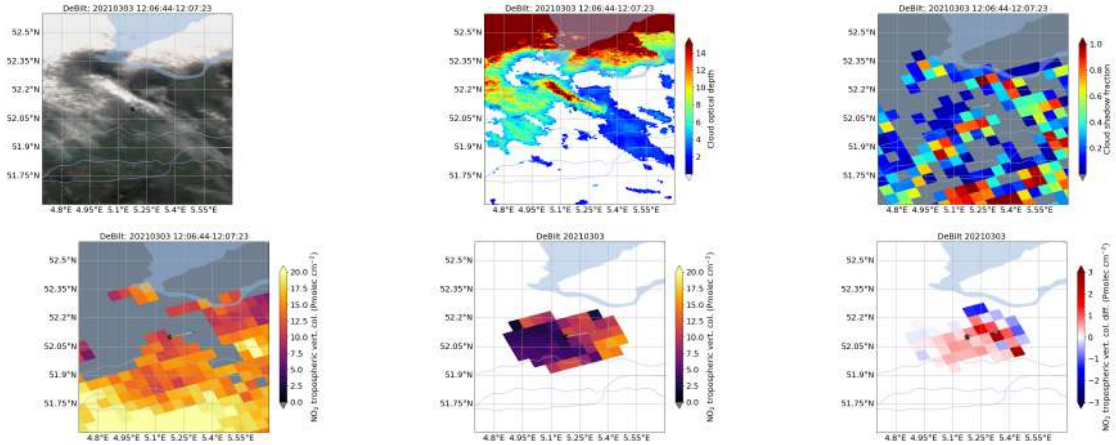

Figure 49: Similar to Fig 38 but for DeBilt and 3 March 2021.

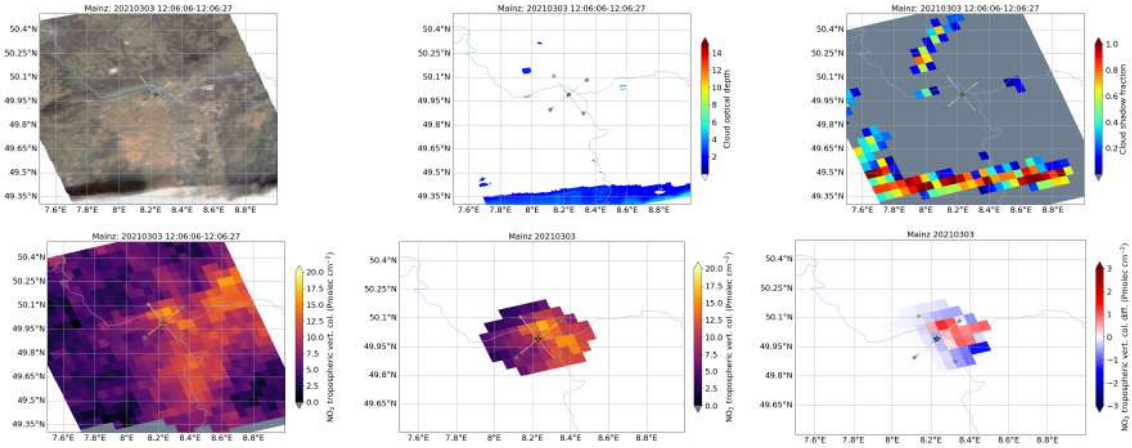

Figure 50: Similar to Fig 38 but for Mainz and 3 March 2021.

References

J. R. Acarreta, J. F. De Haan, and P. Stammes. Cloud pressure retrieval using the O2-O2 absorption band at 477 nm. *Journal of Geophysical Research: Atmospheres*, 109(5), 2004. ISSN 01480227. doi: 10.1029/2003jd003915.

K. F. Boersma, H. J. Eskes, and E. J. Brinksma. Error analysis for tropospheric NO2 retrieval from space. *Journal of Geophysical Research: Atmospheres*, 109(4), 2004. ISSN 01480227. doi: 10.1029/2003jd003962.

K. F. Boersma, H. J. Eskes, R. J. Dirksen, R. J. van der A, J. P. Veefkind, P. Stammes, V. Huijnen, Q. L. Kleipool, M. Sneep, J. Claas, J. Leitão, A. Richter, Y. Zhou, and D. Brunner. An improved tropospheric no_2 column retrieval algorithm for the ozone monitoring instrument. *Atmospheric Measurement Techniques*, 4(9):1905–1928, 2011. doi: 10.5194/amt-4-1905-2011. URL `https://amt.copernicus.org/articles/4/1905/2011/`.

T. Bösch, V. Rozanov, A. Richter, E. Peters, A. Rozanov, F. Wittrock, A. Merlaud, J. Lampel, S. Schmitt, M. de Haij, S. Berkhout, B. Henzing, A. Apituley, M. den Hoed, J. Vonk, M. Tiefengraber, M. Müller, and J. P. Burrows. Boreas – a new max-doas profile retrieval algorithm for aerosols and trace gases.

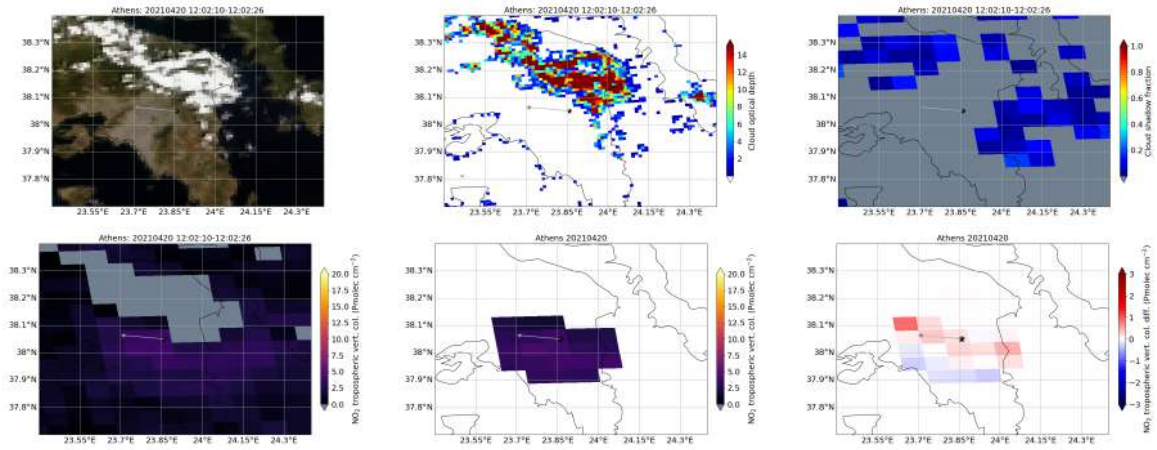

Figure 51: Similar to Fig 38 but for Athens. For 20 April 2021.

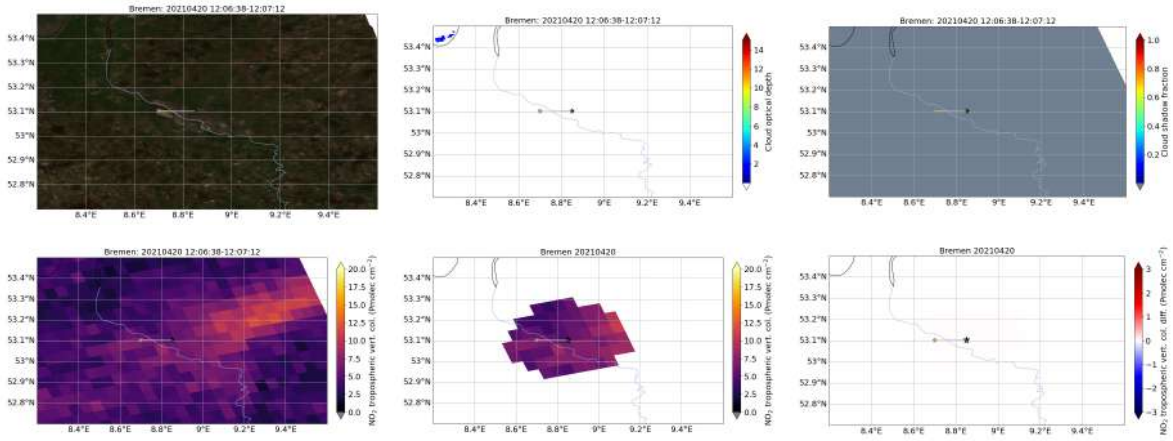

Figure 52: Similar to Fig 38 but for Bremen. For 20 April 2021.

Atmospheric Measurement Techniques, 11(12):6833–6859, 2018. doi: 10.5194/amt-11-6833-2018. URL `https://amt.copernicus.org/articles/11/6833/2018/`.

C. A. Cantrell. Technical note: Review of methods for linear least-squares fitting of data and application to atmospheric chemistry problems. *Atmospheric Chemistry and Physics*, 8(17):5477–5487, 2008. doi: 10.5194/acp-8-5477-2008. URL `https://acp.copernicus.org/articles/8/5477/2008/`.

K. L. Chan, M. Wiegner, J. van Geffen, I. De Smedt, C. Alberti, Z. Cheng, S. Ye, and M. Wenig. Max-doas measurements of tropospheric no_2 and hcho in munich and the comparison to omi and tropomi satellite observations. *Atmospheric Measurement Techniques*, 13(8):4499–4520, 2020. doi: 10.5194/amt-13-4499-2020. URL `https://amt.copernicus.org/articles/13/4499/2020/`.

J. Chimot, T. Vlemmix, J. P. Veefkind, J. F. de Haan, and P. F. Levelt. Impact of aerosols on the omi tropospheric no_2 retrievals over industrialized regions: how accurate is the aerosol correction of cloud-free scenes via a simple cloud model? *Atmospheric Measurement Techniques*, 9(2):359–382, 2016. doi: 10.5194/amt-9-359-2016. URL `https://amt.copernicus.org/articles/9/359/2016/`.

J. Chimot, J. P. Veefkind, J. F. de Haan, P. Stammes, and P. F. Levelt. Minimizing aerosol effects on the omi tropospheric no_2 retrieval – an improved use of the 477 nm o_2-o_2 band and an estimation of

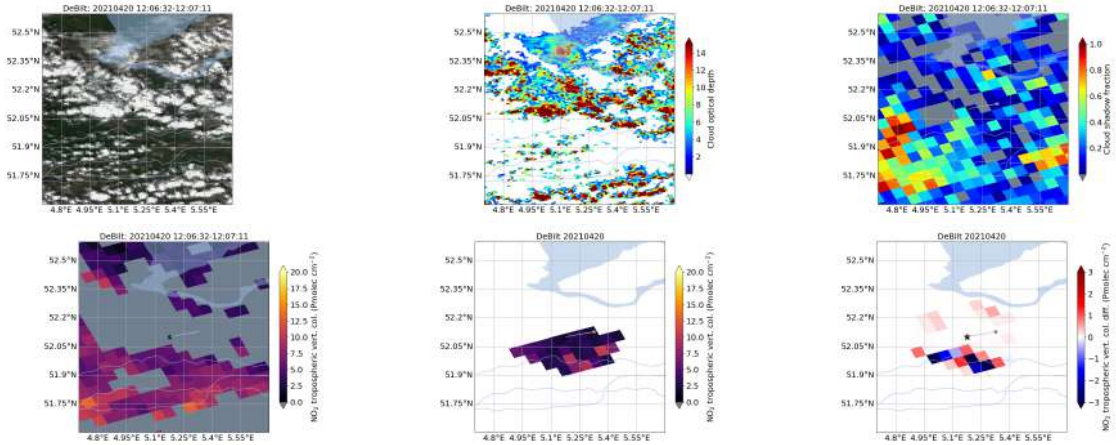

Figure 53: Similar to Fig 38 but for DeBilt. For 20 April 2021.

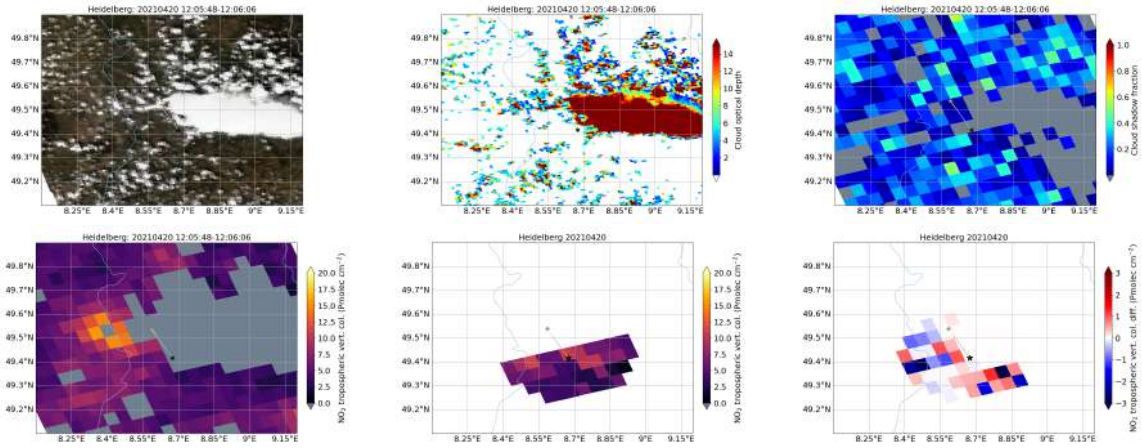

Figure 54: Similar to Fig 38 but for Heidelberg. For 20 April 2021.

the aerosol correction uncertainty. *Atmospheric Measurement Techniques*, 12(1):491–516, 2019. doi: 10.5194/amt-12-491-2019. URL `https://amt.copernicus.org/articles/12/491/2019/`.

K. Clémer, M. Van Roozendael, C. Fayt, F. Hendrick, C. Hermans, G. Pinardi, R. Spurr, P. Wang, and M. De Mazière. Multiple wavelength retrieval of tropospheric aerosol optical properties from maxdoas measurements in beijing. *Atmospheric Measurement Techniques*, 3(4):863–878, 2010. doi: 10.5194/amt-3-863-2010. URL `https://amt.copernicus.org/articles/3/863/2010/`.

E. Dimitropoulou, F. Hendrick, G. Pinardi, M. M. Friedrich, A. Merlaud, F. Tack, H. De Longueville, C. Fayt, C. Hermans, Q. Laffineur, F. Fierens, and M. Van Roozendael. Validation of tropomi tropospheric no_2 columns using dual-scan multi-axis differential optical absorption spectroscopy (max-doas) measurements in uccle, brussels. *Atmospheric Measurement Techniques*, 13(10):5165–5191, 2020. doi: 10.5194/amt-13-5165-2020. URL `https://amt.copernicus.org/articles/13/5165/2020/`.

C. Emde, H. Yu, A. Kylling, M. van Roozendael, K. Stebel, B. Veihelmann, and B. Mayer. Impact of 3d cloud structures on the atmospheric trace gas products from uv–vis sounders – part 1: Synthetic dataset for validation of trace gas retrieval algorithms. *Atmospheric Measurement Techniques*, 15(5): 1587–1608, 2022. doi: 10.5194/amt-15-1587-2022. URL `https://amt.copernicus.org/articles/15/1587/2022/`.

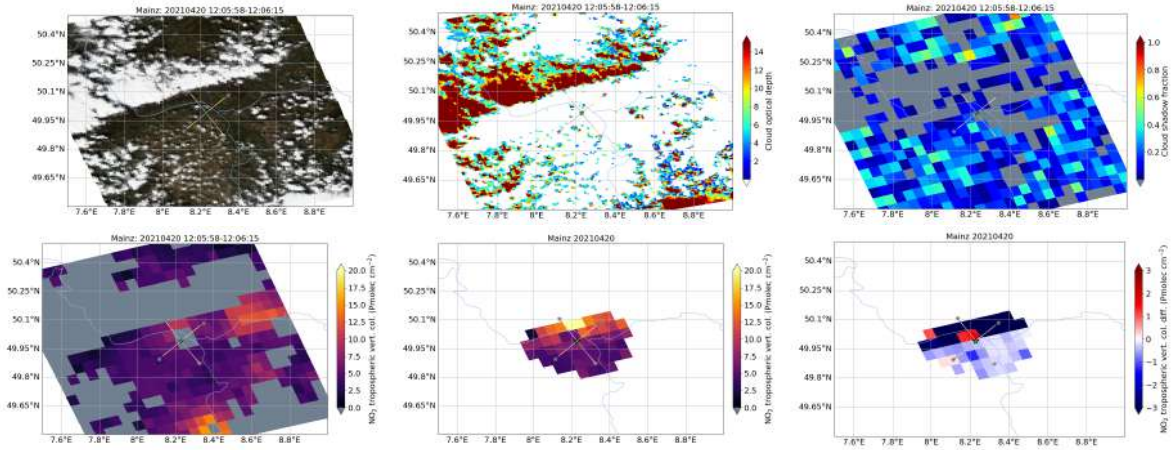

Figure 55: Similar to Fig 38 but for Mainz. For 20 April 2021.

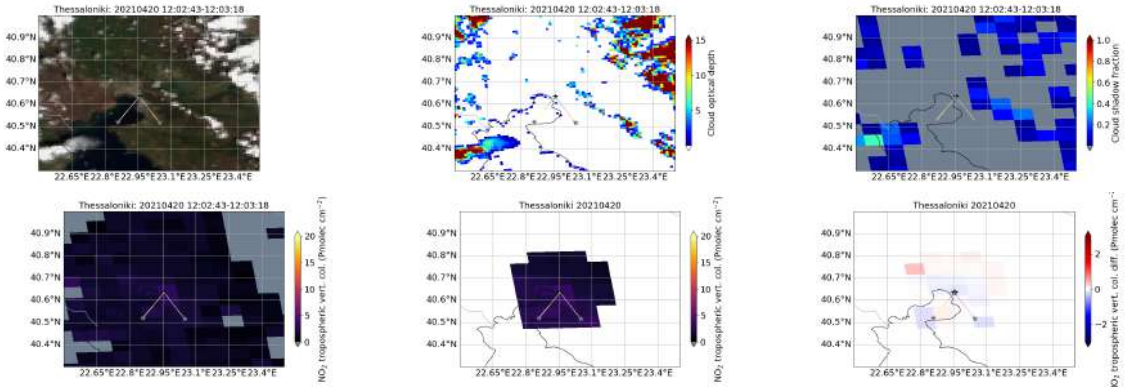

Figure 56: Similar to Fig 38 but for Thessaloniki. For 20 April 2021.

Claudia Emde, Robert Buras, and Bernhard Mayer. ALIS: An efficient method to compute high spectral resolution polarized solar radiances using the Monte Carlo approach. *Journal of Quantitative Spectroscopy and Radiative Transfer*, 112(10), 2011. ISSN 00224073. doi: 10.1016/j.jqsrt.2011.03.018.

Claudia Emde, Robert Buras-Schnell, Arve Kylling, Bernhard Mayer, Josef Gasteiger, Ulrich Hamann, Jonas Kylling, Bettina Richter, Christian Pause, Timothy Dowling, and Luca Bugliaro. The libRadtran software package for radiative transfer calculations (version 2.0.1). *Geoscientific Model Development*, 9(5), 2016. ISSN 19919603. doi: 10.5194/gmd-9-1647-2016.

M. M. Friedrich, C. Rivera, W. Stremme, Z. Ojeda, J. Arellano, A. Bezanilla, J. A. García-Reynoso, and M. Grutter. No_2 vertical profiles and column densities from max-doas measurements in mexico city. *Atmospheric Measurement Techniques*, 12(4):2545–2565, 2019. doi: 10.5194/amt-12-2545-2019. URL `https://amt.copernicus.org/articles/12/2545/2019/`.

Debora Griffin, Xiaoyi Zhao, Chris A. McLinden, Folkert Boersma, Adam Bourassa, Enrico Dammers, Doug Degenstein, Henk Eskes, Lukas Fehr, Vitali Fioletov, Katherine Hayden, Shailesh K. Kharol, Shao-Meng Li, Paul Makar, Randall V. Martin, Cristian Mihele, Richard L. Mittermeier, Nickolay Krotkov, Maarten Sneep, Lok N. Lamsal, Mark ter Linden, Jos van Geffen, Pepijn Veefkind, and Mengistu Wolde. High-resolution mapping of nitrogen dioxide with tropomi: First results and validation over the canadian oil sands. *Geophysical Research Letters*, 46(2):1049–1060, 2019. doi: https://doi.

org/10.1029/2018GL081095. URL https://agupubs.onlinelibrary.wiley.com/doi/abs/10.1029/2018GL081095.

M. Grzegorski, M. Wenig, U. Platt, P. Stammes, N. Fournier, and T. Wagner. The heidelberg iterative cloud retrieval utilities (hicru) and its application to gome data. *Atmospheric Chemistry and Physics*, 6(12):4461–4476, 2006. doi: 10.5194/acp-6-4461-2006. URL https://www.atmos-chem-phys.net/6/4461/2006/.

G. Hönninger, C. von Friedeburg, and U. Platt. Multi axis differential optical absorption spectroscopy (max-doas). *Atmospheric Chemistry and Physics*, 4(1):231–254, 2004. doi: 10.5194/acp-4-231-2004. URL https://acp.copernicus.org/articles/4/231/2004/.

Keith D. Hutchison, Robert L. Mahoney, Eric F. Vermote, Thomas J. Kopp, John M. Jackson, Alain Sei, and Barbara D. Iisager. A geometry-based approach to identifying cloud shadows in the viirs cloud mask algorithm for npoess. *Journal of Atmospheric and Oceanic Technology*, 26(7):1388–1397, 2009. doi: 10.1175/2009JTECHA1198.1. URL https://doi.org/10.1175/2009JTECHA1198.1.

H. Irie, H. Takashima, Y. Kanaya, K. F. Boersma, L. Gast, F. Wittrock, D. Brunner, Y. Zhou, and M. Van Roozendael. Eight-component retrievals from ground-based max-doas observations. *Atmospheric Measurement Techniques*, 4(6):1027–1044, 2011. doi: 10.5194/amt-4-1027-2011. URL https://amt.copernicus.org/articles/4/1027/2011/.

Dimitris Karagkiozidis, Maria-Elissavet Koukouli, Alkiviadis Bais, Dimitris Balis, and Paraskevi Tzoumaka. Assessment of the no_2 spatio-temporal variability over thessaloniki, greece, using max-doas measurements and comparison with s5p/tropomi observations. *Applied Sciences*, 13(4), 2023. ISSN 2076-3417. doi: 10.3390/app13042641. URL https://www.mdpi.com/2076-3417/13/4/2641.

R. B.A. Koelemeijer, P. Stammes, J. W. Hovenier, and J. F. De Haan. A fast method for retrieval of cloud parameters using oxygen a band measurements from the Global Ozone Monitoring Experiment. *Journal of Geophysical Research Atmospheres*, 106(D4), 2001. ISSN 01480227. doi: 10.1029/2000JD900657.

A. Kylling, C. Emde, H. Yu, M. van Roozendael, K. Stebel, B. Veihelmann, and B. Mayer. Impact of 3d cloud structures on the atmospheric trace gas products from uv–vis sounders – part 3: Bias estimate using synthetic and observational data. *Atmospheric Measurement Techniques*, 15(11):3481–3495, 2022. doi: 10.5194/amt-15-3481-2022. URL https://amt.copernicus.org/articles/15/3481/2022/.

S. Liu, P. Valks, G. Pinardi, J. Xu, K. L. Chan, A. Argyrouli, R. Lutz, S. Beirle, E. Khorsandi, F. Baier, V. Huijnen, A. Bais, S. Donner, S. Dörner, M. Gratsea, F. Hendrick, D. Karagkiozidis, K. Lange, A. J. M. Piters, J. Remmers, A. Richter, M. Van Roozendael, T. Wagner, M. Wenig, and D. G. Loyola. An improved tropomi tropospheric no_2 research product over europe. *Atmospheric Measurement Techniques*, 14(11):7297–7327, 2021. doi: 10.5194/amt-14-7297-2021. URL https://amt.copernicus.org/articles/14/7297/2021/.

D. G. Loyola, S. Gimeno García, R. Lutz, A. Argyrouli, F. Romahn, R. J. D. Spurr, M. Pedergnana, A. Doicu, V. Molina García, and O. Schüssler. The operational cloud retrieval algorithms from tropomi on board sentinel-5 precursor. *Atmospheric Measurement Techniques*, 11(1):409–427, 2018. doi: 10.5194/amt-11-409-2018. URL https://amt.copernicus.org/articles/11/409/2018/.

D. G. Loyola, Ronny Lutz, Athina Argyrouli, and Rob Spurr. S5p/tropomi atbd cloud products. *CI-400I-ATBD*, (2.3), 2021. URL https://sentinels.copernicus.eu/documents/247904/2476257/Sentinel-5P-TROPOMI-ATBD-Clouds.

R. Lutz, D. Loyola, S. Gimeno García, and F. Romahn. OCRA radiometric cloud fractions for GOME-2 on MetOp-A/B. *Atmospheric Measurement Techniques*, 9(5):2357–2379, 2016. doi: 10.5194/amt-9-2357-2016. URL https://amt.copernicus.org/articles/9/2357/2016/.

B. Mayer. Radiative transfer in the cloudy atmosphere. *European Physical Journal Conferences*, 1:75–99, 2009.

Bernhard Mayer and A. Kylling. Technical note: The libRadtran software package for radiative transfer calculations - Description and examples of use, 2005. ISSN 16807316.

Paul I. Palmer, Daniel J. Jacob, Kelly Chance, Randall V. Martin, Robert J.D. Spurr, Thomas P. Kurosu, Isabelle Bey, Robert Yantosca, Arlene Fiore, and Qinbin Li. Air mass factor formulation for spectroscopic measurements from satellites: Application to formaldehyde retrievals from the Global Ozone Monitoring Experiment. *Journal of Geophysical Research Atmospheres*, 106(D13), 2001. ISSN 01480227. doi: 10.1029/2000JD900772.

J. Pepijn Veefkind, Johan F. De Haan, Maarten Sneep, and Pieternel F. Levelt. Improvements to the OMI O2-O2 operational cloud algorithm and comparisons with ground-based radar-lidar observations. *Atmospheric Measurement Techniques*, 9(12), 2016. ISSN 18678548. doi: 10.5194/amt-9-6035-2016.

G. Pinardi, M. Van Roozendael, F. Hendrick, N. Theys, N. Abuhassan, A. Bais, F. Boersma, A. Cede, J. Chong, S. Donner, T. Drosoglou, A. Dzhola, H. Eskes, U. Frieß, J. Granville, J. R. Herman, R. Holla, J. Hovila, H. Irie, Y. Kanaya, D. Karagkiozidis, N. Kouremeti, J.-C. Lambert, J. Ma, E. Peters, A. Piters, O. Postylyakov, A. Richter, J. Remmers, H. Takashima, M. Tiefengraber, P. Valks, T. Vlemmix, T. Wagner, and F. Wittrock. Validation of tropospheric no_2 column measurements of gome-2a and omi using max-doas and direct sun network observations. *Atmospheric Measurement Techniques*, 13(11):6141–6174, 2020. doi: 10.5194/amt-13-6141-2020. URL `https://amt.copernicus.org/articles/13/6141/2020/`.

Ulrich Platt and J. Stutz. *Differential optical absorption spectroscopy: principles and applications*. Physics of Earth and space environments. Springer, Berlin, 2008. ISBN 9783540211938 9783540757764.

Stefan F. Schreier, Andreas Richter, Enno Peters, Mareike Ostendorf, Alois W. Schmalwieser, Philipp Weihs, and John P. Burrows. Dual ground-based max-doas observations in vienna, austria: Evaluation of horizontal and temporal no2, hcho, and chocho distributions and comparison with independent data sets. *Atmospheric Environment: X*, 5:100059, 2020. ISSN 2590-1621. doi: https://doi.org/10.1016/j.aeaoa.2019.100059. URL `https://www.sciencedirect.com/science/article/pii/S2590162119300620`.

M. Schwaerzel, C. Emde, D. Brunner, R. Morales, T. Wagner, A. Berne, B. Buchmann, and G. Kuhlmann. Three-dimensional radiative transfer effects on airborne and ground-based trace gas remote sensing. *Atmospheric Measurement Techniques*, 13(8):4277–4293, 2020. doi: 10.5194/amt-13-4277-2020. URL `https://amt.copernicus.org/articles/13/4277/2020/`.

V. J. H. Trees, P. Wang, P. Stammes, L. G. Tilstra, D. P. Donovan, and A. P. Siebesma. Darclos: a cloud shadow detection algorithm for tropomi. *Atmospheric Measurement Techniques*, 15(10): 3121–3140, 2022. doi: 10.5194/amt-15-3121-2022. URL `https://amt.copernicus.org/articles/15/3121/2022/`.

J.P. Veefkind, I. Aben, K. McMullan, H. Forster, J. de Vries, G. Otter, J. Claas, H.J. Eskes, J.F. de Haan, Q. Kleipool, M. van Weele, O. Hasekamp, R. Hoogeveen, J. Landgraf, R. Snel, P. Tol, P. Ingmann, R. Voors, B. Kruizinga, R. Vink, H. Visser, and P.F. Levelt. {TROPOMI} on the {ESA} sentinel-5 precursor: A {GMES} mission for global observations of the atmospheric composition for climate, air quality and ozone layer applications. *Remote Sensing of Environment*, 120(0):70 – 83, 2012. ISSN 0034-4257. doi: http://dx.doi.org/10.1016/j.rse.2011.09.027. URL `http://www.sciencedirect.com/science/article/pii/S0034425712000661`. The Sentinel Missions - New Opportunities for Science.

T. Verhoelst, S. Compernolle, G. Pinardi, J.-C. Lambert, H. J. Eskes, K.-U. Eichmann, A. M. Fjæraa, J. Granville, S. Niemeijer, A. Cede, M. Tiefengraber, F. Hendrick, A. Pazmiño, A. Bais, A. Bazureau, K. F. Boersma, K. Bognar, A. Dehn, S. Donner, A. Elokhov, M. Gebetsberger, F. Goutail, M. Grutter de la Mora, A. Gruzdev, M. Gratsea, G. H. Hansen, H. Irie, N. Jepsen, Y. Kanaya, D. Karagkiozidis, R. Kivi, K. Kreher, P. F. Levelt, C. Liu, M. Müller, M. Navarro Comas, A. J. M. Piters, J.-P. Pommereau, T. Portafaix, C. Prados-Roman, O. Puentedura, R. Querel, J. Remmers, A. Richter, J. Rimmer, C. Rivera Cárdenas, L. Saavedra de Miguel, V. P. Sinyakov, W. Stremme, K. Strong, M. Van Roozendael, J. P. Veefkind, T. Wagner, F. Wittrock, M. Yela González, and C. Zehner.

Ground-based validation of the copernicus sentinel-5p tropomi no_2 measurements with the ndacc zsl-doas, max-doas and pandonia global networks. *Atmospheric Measurement Techniques*, 14(1):481–510, 2021. doi: 10.5194/amt-14-481-2021. URL https://amt.copernicus.org/articles/14/481/2021/.

P. Wang, P. Stammes, R. Van Der A, G. Pinardi, and M. Van Roozendael. FRESCO+: An improved O2 A-band cloud retrieval algorithm for tropospheric trace gas retrievals. *Atmospheric Chemistry and Physics*, 8(21):6565–6576, nov 2008. ISSN 16807324. doi: 10.5194/acp-8-6565-2008.

Y. Wang, J. Lampel, P. Xie, S. Beirle, A. Li, D. Wu, and T. Wagner. Ground-based max-doas observations of tropospheric aerosols, no_2, so_2 and hcho in wuxi, china, from 2011 to 2014. *Atmospheric Chemistry and Physics*, 17(3):2189–2215, 2017. doi: 10.5194/acp-17-2189-2017. URL https://acp.copernicus.org/articles/17/2189/2017/.

H. Yu, C. Emde, A. Kylling, B. Veihelmann, B. Mayer, K. Stebel, and M. Van Roozendael. Impact of 3d cloud structures on the atmospheric trace gas products from uv–vis sounders – part 2: Impact on no_2 retrieval and mitigation strategies. *Atmospheric Measurement Techniques*, 15(19):5743–5768, 2022. doi: 10.5194/amt-15-5743-2022. URL https://amt.copernicus.org/articles/15/5743/2022/.

X. Zhao, D. Griffin, V. Fioletov, C. McLinden, A. Cede, M. Tiefengraber, M. Müller, K. Bognar, K. Strong, F. Boersma, H. Eskes, J. Davies, A. Ogyu, and S. C. Lee. Assessment of the quality of tropomi high-spatial-resolution no_2 data products in the greater toronto area. *Atmospheric Measurement Techniques*, 13(4):2131–2159, 2020. doi: 10.5194/amt-13-2131-2020. URL https://amt.copernicus.org/articles/13/2131/2020/.